Doctoral Dissertation
博士論文

Spectroscopic Study on Galactic Outflows over Cosmic History
(宇宙史における銀河アウトフローの分光学的研究)

令和元年 12 月博士 (理学) 申請
A Dissertation Submitted for the Degree of Doctor of Philosophy
December 2019

東京大学大学院理学系研究科
物理学専攻
Department of Physics, Graduate School of Science,
The University of Tokyo

菅原 悠馬
Yuma Sugahara

Ph.D. Thesis Committee:

Dr. Kazuhisa Mitsuda (Department of Space Astronomy and Astrophysics, Institute of Space and Astrocautical Science, Japan Aerospace eXploration Agency); Chair

Dr. Aya Bamba (Department of Physics, Graduate School of Science, The University of Tokyo)

Dr. Hideyuki Tagoshi (Institute for Cosmic Ray Research, University of Tokyo)

Dr. Toru Misawa (School of General Education, Shinshu University)

Dr. Masao Mori (Center for Computational Sciences, University of Tsukuba)

Thesis Advisor:

Dr. Masami Ouchi (Institute for Cosmic Ray Research, University of Tokyo; National Astronomical Observatory of Japan)

This thesis is based on the following papers:

PAPER-I: Yuma Sugahara, Masami Ouchi, Lihwai Lin, Cristal L. Martin, Yoshiaki Ono, Yuichi Harikane, Takatoshi Shibuya, & Renbin Yan
The Astrophysical Journal, 850, 51 (2017)
"Evolution of Galactic Outflows at z ∼0–2 Revealed with SDSS, DEEP2, and Keck Spectra"

PAPER-II: Yuma Sugahara, Masami Ouchi, Yuichi Harikane, Nicolas Bouché, Peter D. Mitchell, and Jérémy Blaizot
The Astrophysical Journal, 886, 29 (2019)
"Fast Outflows Identified in Early Star-Forming Galaxies at $z = 5$–6"

ACKNOWLEDGEMENTS

I would like to express my heartfelt appreciation to my supervisor, Masami Ouchi. When I joined the Ouchi group at Institute for Cosmic Ray Research, the University of Tokyo, I wanted to start researches on the galaxy formation and evolution. The theme he proposed me was the galactic outflow, which is the science topic I have been devoted to for the five years. The outflow studies are really tough, especially for the first three years, and sometimes my opinions were against Ouchi-san's advice, but Ouchi-san have been kept to give me comments on my studies so patiently and tell me what is important in Astronomy. Now I understand crucial roles of the galactic outflows in the galaxy formation and evolution to finish writing up my Ph.D. thesis. I greatly appreciate his continuous encouragement to me.

I am grateful to my collaborators. Yoshiaki Ono gave me helpful advice to start studies of the outflows. He also helped me progress studies, give presentations, and write applications. Yuichi Harikane is always interested in my outflow study, gives me comments, and help me for the DEIMOS data reductions. Takatoshi Shibuya taught me how to reduce the LRIS spectra. Lihwai Lin and Renbin Yan let me use the DEEP2 calibration pipeline and give me information of the DEEP2 galaxies. Crystal L. Martin gave me precious advice that promote my study. Nicolas Bouché hosted my stay at Lyon Observatory and gave me opportunities to discuss my results with many researchers. The discussion with him on the scaling relation between outflow velocities and galaxy properties was very suggestive for me to deeply think about the outflows. Peter D. Mitchell and Jérémy Blaizot gave me much theoretical advice to interpret the agreements between our results and numerical simulations. Specifically, Peter explained the outflows in the simulations many times, which is important for me to understand the outflow theory.

I thank Christopher N. A. Willmer for sharing the measurements of the DEEP2 rest-frame magnitudes with me. I am grateful to the Ph.D. thesis committee, including Kazuhisa Mitsuda, Aya Bamba, Hideyuki Tagoshi, Toru Misawa, and Masao Mori, for many constructive comments, especially about the noise analysis, that improve this thesis. I appriciate useful comments to my study from Xinnan Du, Kate Rubin,

John Chisholm, Léo Michel-Dansac, Timothy M. Heckman, Asuka Igarashi, Hidenobu Yajima, Tsutomu T. Takeuchi, Kentaro Nagamine, Akio K. Inoue, Kazuhiro Shimasaku, Takashi Horiuchi, Suzuka Koyamada, and Koki Terao. I acknowledge the PIs of the data in this work.

I am grateful to the members of our research group for supporting my study and making my Kashiwa life so exciting: Masami Ouchi, Yoshiaki Ono, Ken Mawatari, Jun Toshikawa, Takatoshi Shibuya, Yuma Suraphong, Florent Duval, Akira Konno, Masafumi Ishigaki, Yuko Tamazawa, Seiji Fujimoto, Yuichi Harikane, Haibin Zheng, Takashi Kojima, Shiro Mukae, Ryo Higuchi, Mitftal Hilmi, Shotaro Kikuchihara, Ryohei Itoh, Ryota Kakuma, Karin Shimodate, Yechi Zhang, Yuki Isobe, Nao Sakai, and Sun Dongsheng. At times we seriously discussed and criticized our own science topics; At times we enjoyed games, foods, and drinks with talking about random topics for a long time. I have experienced many things which make me happy, excited, sad, and tired for these five years. I am sure I am lucky to share my experiences with them and so happy to meet them all. Especially, I would like to express sincere gratitude to Takashi and Shiro. Without the two of them, I would not have spent my Ph.D. period such excited. From next year we will start walking very different paths. I hope their successes in their carriers. Let's gather and talk in the near future.

I am grateful to my friends in astronomy, especially to Tomohiro Inada, Yuki Iwamura, Wataru Ishizaki, Satoshi Kikuta, and Yasunori Terao. I could deepen my understanding to galaxies and high energy physics thanks to them. Moreover, the daily life in Kashiwa and travels in Japan with them were much fun to me. I thank my friends and colleagues in ICRR for wonderful days: Satoshi Fukami, Wakutaka Nakano, Keisuke Inomata, Kunihiko Hasegawa, Koshi Nagano, Yutaro Enomoto, Kouseki Miyo, Tomoya Kinugawa, and Shota Tanaka. Also I thank my friends and colleagues studying astronomy for inspiring me: Tadafumi Matsuno, Misaki Ando, Ryo Ando, Taku Okamura, Yuya Aono, Yuki Taniguchi, Eriko Kusunoki, Yuko Matsushita, Kouki Higuchi, Ippei Kurose, Haruka Kuakabe, Takuya Hashimoto, Takahiro Sudoh, Ryota Kawamata, Takahiro Morishita, Hiroyuki Ishikawa, and Hideaki Matsumura.

I would also like to show my appreciation to Kashiwanoha Science Education Lab

(KSEL), an outreach group in Kashiwa, especially to Taiga Hamura and Chihiro Miyamoto. I have been a member of KSEL since the first grade of a Ph.D. student. The many opportunities to give talks to people with various ages were good chances for me to look back and to understand my studies better.

There are still many people who helped me but I could not list up here. I would like to show thankfulness to all of the people who support me and cheer me up. The time that I spent with them is now my precious memory. I would like to express my special appreciation to Sumire Fujimoto, who colors my life. Finally, I would like to give my special thanks to my family for supporting and understanding me.

Funding for the SDSS and SDSS-II has been provided by the Alfred P. Sloan Foundation, the Participating Institutions, the National Science Foundation, the U.S. Department of Energy, the National Aeronautics and Space Administration, the Japanese Monbukagakusho, the Max Planck Society, and the Higher Education Funding Council for England. The SDSS Web Site is http://www.sdss.org/. The SDSS is managed by the Astrophysical Research Consortium for the Participating Institutions. The Participating Institutions are the American Museum of Natural History, Astrophysical Institute Potsdam, University of Basel, University of Cambridge, Case Western Reserve University, University of Chicago, Drexel University, Fermilab, the Institute for Advanced Study, the Japan Participation Group, Johns Hopkins University, the Joint Institute for Nuclear Astrophysics, the Kavli Institute for Particle Astrophysics and Cosmology, the Korean Scientist Group, the Chinese Academy of Sciences (LAMOST), Los Alamos National Laboratory, the Max-Planck-Institute for Astronomy (MPIA), the Max-Planck-Institute for Astrophysics (MPA), New Mexico State University, Ohio State University, University of Pittsburgh, University of Portsmouth, Princeton University, the United States Naval Observatory, and the University of Washington.

The data presented herein were obtained at the W. M. Keck Observatory, which is operated as a scientific partnership among the California Institute of Technology, the University of California and the National Aeronautics and Space Administration. The Observatory was made possible by the generous financial support of the W. M.

Keck Foundation. The DEEP2 team and Keck Observatory acknowledge the very significant cultural role and reverence that the summit of Mauna Kea has always had within the indigenous Hawaiian community and appreciate the opportunity to conduct observations from this mountain. The analysis pipeline used to reduce the DEIMOS data was developed at UC Berkeley with support from NSF grant AST-0071048. Funding for the DEEP2 Galaxy Redshift Survey has been provided by NSF grants AST-95-09298, AST-0071048, AST-0507428, and AST-0507483 as well as NASA LTSA grant NNG04GC89G.

This research has made use of the Keck Observatory Archive (KOA), which is operated by the W. M. Keck Observatory and the NASA Exoplanet Science Institute (NExScI), under contract with the National Aeronautics and Space Administration. I wish to recognize and acknowledge the very significant cultural role and reverence that the summit of Maunakea has always had within the indigenous Hawaiian community. We are most fortunate to have the opportunity to conduct observations from this mountain.

This work is supported by World Premier International Research Center Initiative (WPI Initiative), MEXT, Japan, and KAKENHI (15H02064, 17H01110, and 17H01114) Grant-in-Aid for Scientific Research (A) through Japan Society for the Promotion of Science (JSPS). I greatfully acknowledges support from the JSPS through the JSPS Research Fellowship for Young Scientists.

ABSTRACT

The galactic outflows in star-forming galaxies are thought to play a key role to regulate the galaxy evolution. Despite many observations in a wide redshift range, it is unclear how the outflows evolve throughout redshifts. We conduct a systematic study of the galactic-scale cool/warm outflows in star-forming galaxies at $z \sim 0$–6, by analyzing the metal absorption lines in the observed-frame optical spectra taken from the SDSS DR7 at $z \sim 0$, the DEEP2 DR4 at $z \sim 1$, Keck galaxies in Erb et al. at $z \sim 2$, and Lyman break galaxies in Capak et al. at $z = 5$–6. We carefully construct galaxy samples with similar stellar-mass distributions at $z \sim 0$, 1, 2, and 5–6 and produce composite spectra with high signal-to-noise ratio to perform the multi-component fitting of absorption-line profiles and stellar continua to the absorption lines. We finally obtain outflow properties from the blueshifted outflow components.

We measure the maximum ($v_{\rm max}$) and central ($v_{\rm out}$) outflow velocities from the outflow components. By making use of the ALMA [C II]158 μm emission lines for systemic velocities, we can present the first measurements of the outflow velocities at $z = 5$–6: $v_{\rm max} = 700^{+180}_{-110}$ km s^{-1} and $v_{\rm out} = 400^{+100}_{-150}$ km s^{-1}. Although the available absorption lines depend on the redshifts, we investigate the redshift evolution of the outflow velocities by comparing the absorption lines that have similar ionization energy and line depth at different redshifts (Na I D and Mg I at $z \sim 0$–1; Mg II and C II at $z \sim 1$–2). This comparison shows no significant differences between the outflow velocities derived from the low to high-ionization absorption lines. We identify, for the first time, the $v_{\rm max}$ value of our $z = 5$–6 galaxies is 3.5 times higher than those of $z \sim 0$ galaxies and comparable to $z \sim 2$ galaxies at a fixed stellar mass of $M_* \sim 10^{10.1}$ M$_\odot$. This implies that the outflow velocities strongly increase from $z \sim 0$ to 2 and weakly increase from $z \sim 2$ to 6 at the fixed stellar mass.

Estimating the halo circular velocity $v_{\rm cir}$ from the stellar masses and the abundance matching results, we investigate a $v_{\rm max}$–$v_{\rm cir}$ relation. The maximum outflow velocity $v_{\rm max}$ for galaxies with $M_* = 10^{10.0-10.8}$ M$_\odot$ shows a tight positive correlation with $v_{\rm cir}$ and the galaxy star formation rate (SFR) over $z = 0$–6 with a small scatter of $\simeq \pm 0.1$ dex. This positive correlation between $v_{\rm max}$ and $v_{\rm cir}$ is in good agreement

with theoretical predictions by numerical simulations. This suggests that the outflow velocity is physically related to the halo circular velocity. The redshift evolution of $v_{\rm max}$ at fixed M_* can be explained by the increase of $v_{\rm cir}$ toward high redshift.

To find the fundamental parameter to determine $v_{\rm max}$ with a single relation throughout all redshifts, we study relations between $v_{\rm max}$ and galaxy properties. The outflow maximum velocity $v_{\rm max}$ shows strong correlations with $v_{\rm cir}$, SFR, SFR/M_*, and the predicted SFR surface density $\Sigma_{\rm SFR}$. In addition to the tight correlations, only $v_{\rm cir}$ and SFR can explain $v_{\rm max}$ with single scaling relations throughout $z = 0$–6. Therefore, $v_{\rm cir}$ or SFR is likely to be the fundamental parameter.

We also estimate the mass loading factor (η), a ratio of the mass outflow rate to SFR, under the assumption of the fiducial parameters. We find that the η value increases from $z \sim 0$ to 2 by $\eta \propto (1+z)^{1.2\pm0.3}$ at a given $v_{\rm cir}$, albeit with a potential systematics caused by model parameter choices. The redshift evolution of $v_{\rm max}$ ($v_{\rm out}$) and η is consistent with the galaxy-size evolution and explained by high-gas fractions in high-redshift massive galaxies, which is supported by radio observations. We obtain a scaling relation of $\eta \propto v_{\rm cir}^a$ for $a = -0.2 \pm 1.1$ in our $z \sim 0$ galaxies that agrees with the momentum-driven outflow model ($a = -1$) within the uncertainty.

We indirectly estimate the escape fraction of the Lyman-continuum photons using absorption-line profiles. Our measurement at $z = 5$–6 is located on the relation found at $z \sim 2$–4 between the maximum covering fraction of the Si II line and the Lyα equivalent width. The intrinsic Lyman-continuum escape fraction would be much lower than 20%, while the ratio absorption-line profile exhibits a signature comparable to the local Lyman-continuum leaking galaxies.

TABLE OF CONTENTS

CHAPTER 1
INTRODUCTION

1.1 Galaxy and IGM Evolution in Baryon Cycle

Large spectroscopic observations investigated the galaxy distribution in the universe. The observations have revealed the large cosmic structure where galaxies are placed in dense and sparse regions, referred as to galaxy clusters and voids, respectively. In present, this large-scale structure of the universe is well explained by the gravitational interactions based on the Lambda cold dark matter (ΛCDM) model (e.g., Springel et al. 2005).

To explain small scale structures like galaxies, we need additional models because these small scales are governed by the baryon physics. Gas in the dark matter halos loses its energy by radiative cooling and gradually accretes onto galaxies. The dense and cold intergalactic medium (IGM) can penetrate the dark matter halos and directly accrete from the IGM to galaxies (cold accretion; e.g., Dekel & Birnboim 2006). In the core of the cold dense gas in the galaxies, the nuclear fusion is ignited and stars form. The stars produce elements heavier than helium (metal) in themselves, drive stellar winds, and blow away metal and dusts into the interstellar medium (ISM). The massive stars with the stellar mass of $M_* \gtrsim 9$ $M_\odot$ (Heger et al. 2003) end their lives with the supernova (SN) explosion, providing energy, metals, and dusts to the ISM. The supermassive black holes (SMBHs), which exist basically in the centers of the galaxies, can also release huge energy, corresponding to galaxy luminosity, from their accretion disks. Such active SMBHs are called as active galactic nuclei (AGNs), exhibiting signatures like jets, outflows, X-ray radiation, highly ionized emission lines, broad components of emission lines, and significant radio emission. These energetic activities of SNe and AGNs accelerate the ISM and launch galactic-scale outflows. The galactic outflows transfer the products of stars from galaxies into the circumgalactic medium (CGM) and the IGM. A part of the outflows cannot escape the galaxy halos and come back to galactic disks to contribute the star-forming activity again (Figure 1.1).

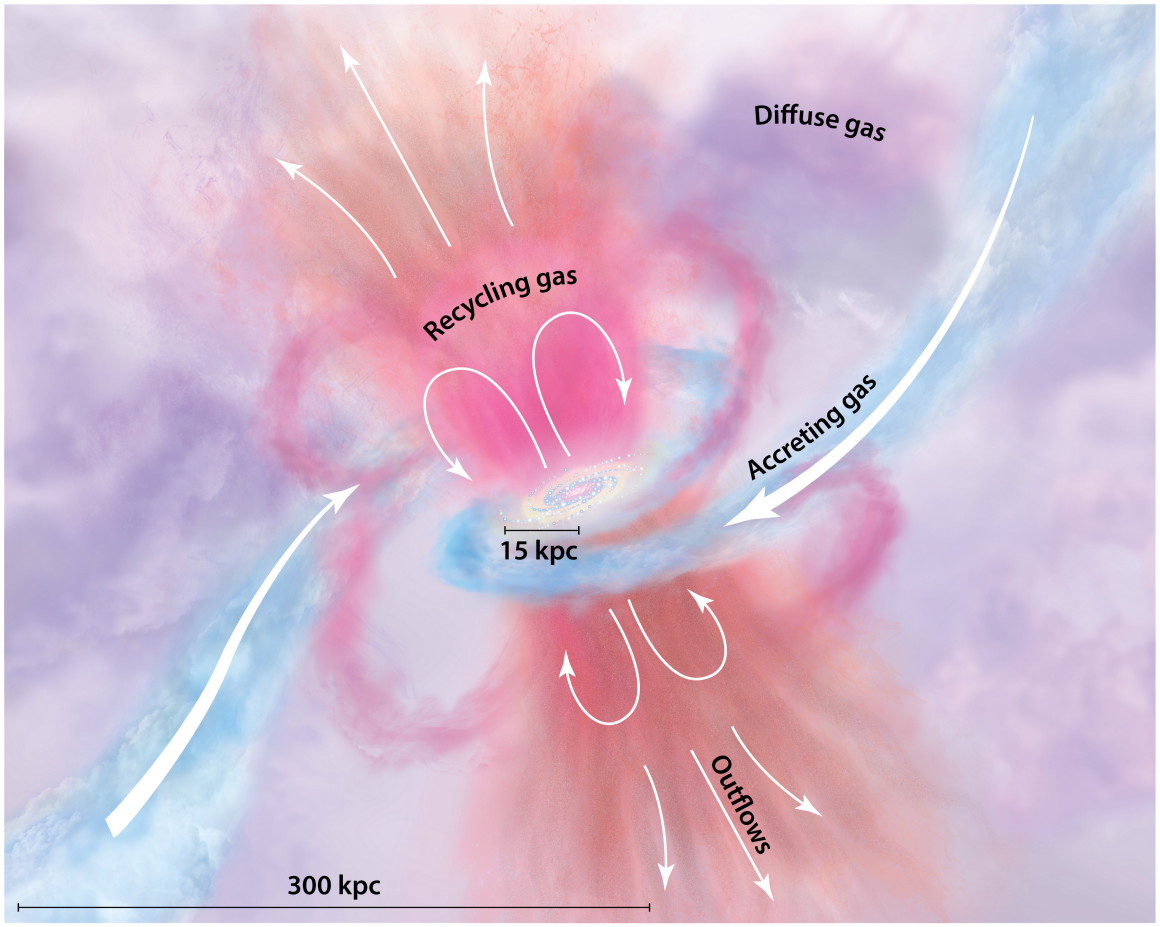

Tumlinson J, et al. 2017.
Annu. Rev. Astron. Astrophys. 55:389–432

Figure 1.1 Schematic picture of the baryon cycle. The starformation in the central galaxy is invoked by inflowing gas (blue), and drives the outflowing gas (pink and orange). The figure is taken from Figure 1 of Tumlinson et al. (2017).

As shown above, galaxies evolve through the baryon cycle, i.e., inflowing gas from the IGM to galaxies, starformation in galaxies and accretion onto SMBHs, and outflowing gas from galaxies to the IGM. Along with galaxies, the CGM and IGM keep changing their composition of elements and ionization states. Therefore, the baryon cycle is a key process for us to understand the galaxy, CGM, and IGM evolution,

1.2 Feedback Processes to Regulate Galaxy Evolution

1.2.1 feedback processes to starformation

One of the biggest problems in extragalactic astronomy is a notable discrepancy between the shapes of the halo mass function predicted by numerical simulations of ΛCDM model and the galaxy stellar mass function confirmed by observations (e.g., Somerville & Davé 2015). This is clearly represented in the drops of the stellar-to-halo mass ratio (SHMR) at the massive and less massive end (Behroozi et al. 2013; Harikane et al. 2016; Ishikawa et al. 2017; Harikane et al. 2018), as shown in Figure 1.2. This discrepancy suggests the existence of the mechanisms that reduce the efficiency of the starformation at the high and low mass regime. Thus, the galaxy formation and evolution are regulated by negative feedback processes where star-forming activity suppresses the starformation in the next generation.

Many physical mechanisms of the feedback processes are proposed, such as thermal energy inputs from SNe, photoionization of molecular clouds, and photo-heating and radiation pressure creating holey giant molecular clouds. The plausible main drivers of the feedback are AGNs for massive galaxies and the SN-driven outflows for less massive galaxies.

The AGN signatures are detected mostly in the massive galaxies (e.g., Förster Schreiber et al. 2019). The AGN in the massive galaxies can suppress star-formation with inputs of thermal energy, kinetic energy, and photo ionization. AGN-driven outflows are predicted to play an important role to quench the star-forming activity in massive galaxies.

1.2.2 Galactic Outflows Driven by SNe

In contrast to the AGN-driven outflows, SN-driven outflows are thought to affect galaxies primarily in low-mass regime, because outflows can relatively easily escape the gravitational potential of low-mass galaxies. The mass, momentum, energy, and metal budgets of the outflows leaked from the star-forming galaxies are theoretically important for regulating the star-forming activity in low-mass galaxies.

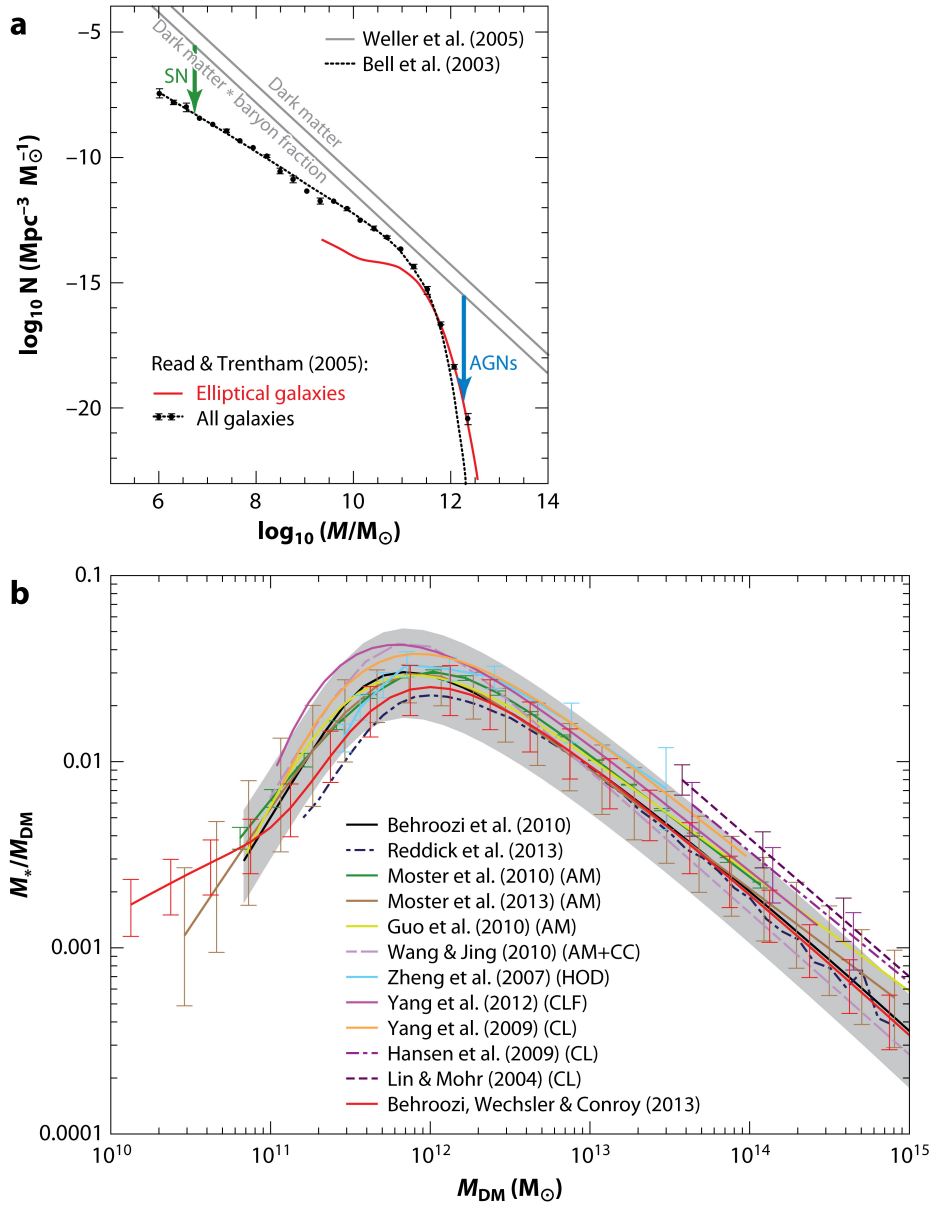

Kormendy J, Ho LC. 2013.
Annu. Rev. Astron. Astrophys. 51:511–653

Figure 1.2 (a) Observed baryonic mass function with the black points (Read & Trentham 2005) and the dotted lines (Bell et al. 2003), in comparison with theoretical prediction by numerical simulations (Weller et al. 2005, solid lines). There are discrepancies at the low and high mass ends of the functions. (b) Stellar-to-halo mass ratio of galaxies estimated from abundance matching (AM), clustering constraints (CC), modeling of halo occupation distributions (HOD), conditional luminosity function (CLF), and various results on galaxy clusters (CL). There is the peak at $M_{\rm DM} \sim 10^{12}$ $M_\odot$ and steep drop at the low and high mass ends. The figure is taken from Figure 25 of Kormendy & Ho (2013).

The metal budgets of the outflows are also important for the chemical evolution of the galaxies and the IGM. While the stellar mass of galaxies are regulated by the outflows, the metallicity that stars produce are released into the CGM and IGM by the outflows. Therefore, the outflows have a large impact on the mass-metalicity relation of galaxies (Tremonti et al. 2004). In contrast, the CGM and IGM are polluted by the metals transferred from galaxies (Somerville & Davé 2015; Dayal & Ferrara 2018). The metal enrichment of the IGM is observed with the quasar (QSO) absorption lines (Madau & Dickinson 2014).

Outflows may help ionizing photons escape from galaxies by creating holes in the ISM. The ionizing photons are rarely observed in local Universe because they are almost absorbed by neutron Hydrogen in galaxies. However, if strong outflows at high redshift help the ionizing photons leak, the outflows may be important phenomena for the reionization of the universe.

1.3 Galactic Outflows in Star-forming Galaxies

1.3.1 Theoretical Aspects

The details of the outflows driven by star-forming activities have been theoretically investigated with analytical models and simulations (Zhang 2018). The cold gas is launched by the starburst or the SNe and the lack of the cold gas quenches the starformation in the galaxies. Despite predicted impacts of the outflows on the star formation activity, physical mechanisms of the outflows are still poorly known.

The most classical scenario is the hot fluid outflows driven by the core-collapse SNe (e.g., Larson 1974; Chevalier & Clegg 1985; Springel & Hernquist 2003). This hot outflows are in good agreement with the X-ray observations and have been studied with this models (e.g., Strickland & Heckman 2009). However, the launch of the multi-phase outflows in observations (Veilleux et al. 2005) is still unclear, especially for low temperature gas, which is possible to be dominant in mass transfer. Theoretical work has been proposed many candidate hypotheses: thermal pressure of the core-collapse SNe, the ultra-violet (UV) radiation pressure of the starburst acting on dusts

(e.g., Leitherer et al. 1999), the infrared (IR) radiation pressure acting on dust in the optically thick case (e.g., Murray et al. 2005; Oppenheimer & Davé 2006), the radiation pressure based on the resonance-scattering lines (e.g., Castor et al. 1975; Kimm et al. 2018), and the cosmic ray pressure (e.g., Ipavich 1975; Breitschwerdt et al. 1991; Wadepuhl & Springel 2011).

In numerical simulations, many theoretical studies contribute to revealing the outflow properties (Oppenheimer et al. 2010; Muratov et al. 2015; Christensen et al. 2016; Ceverino et al. 2016; Mitchell et al. 2018; Nelson et al. 2019). In most numerical simulations, the outflows and SN feedback are implemented with the "sub-grid" physics (Somerville & Davé 2015), to reproduce the statistical galaxy relations such as the stellar-mass functions and the mass-metallicity relations. Some recent simulations employ the explicit thermal feedback generated by SNe with no outflows in subgrid physics, and describe the relation between the outflow and galaxy properties (Schaye et al. 2015; Muratov et al. 2015; Barai et al. 2015). Although the analysis of the outflow properties are different from the estimation with observations, the observed measurements are reproduced in simulations (e.g., Nelson et al. 2019). Theories in the outflows are definitely progressing, but there remains many complicated physics, such as energy and momentum inputs to the ISM, multi-phase gas structures, thermal and hydrodynamic instabilities, and interactions with magnetic fields.

1.3.2 Observational Aspects

To understand the pictures of the outflows, observational constraints are important. The outflows are composed of the various ISM phases, cold molecular, cool atomic, ionized warm, and hot plasma gas (Veilleux et al. 2005; Rupke 2018). The hot plasma gas of nearby galaxies are explored by X-ray observations for the temperature, energy, pressure, mass, and velocities of the outflows (e.g., Griffiths et al. 2000; Strickland & Heckman 2009)

By using far-UV (FUV; 1000–2000Å) to optical observation, we can extend our study to the outflows in high-redshift galaxies (Figure 1.3). The emission lines like Hα and [O III] in the rest-frame optical wavelengths represent the warm ionized out-

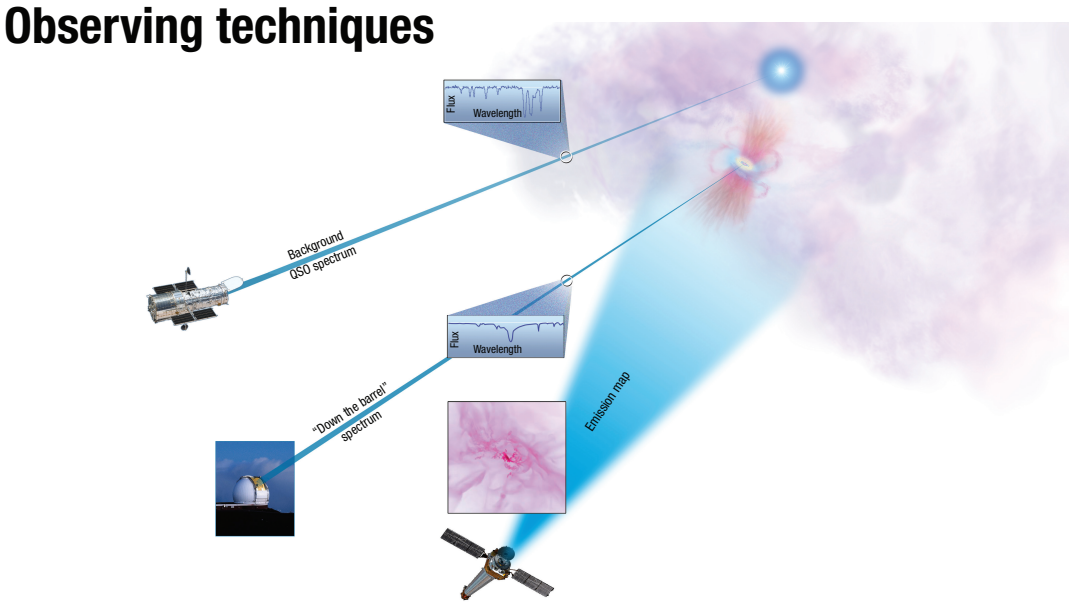

Figure 1.3 Observational techniques to probe the outflowing gas and the CGM, including emission line study, "down-the-barrel" methods with absorption lines, and absorption lines in spectra of background QSOs. The figure is taken from Supplemental Figure 1 of Tumlinson et al. (2017).

flowing gas (Lehnert & Heckman 1996a,b; Heckman et al. 1990; Martin 1998). Broad components in the emission lines provide the kinematics of ionized outflows (Cicone et al. 2016; Finley et al. 2017; Concas et al. 2017; Freeman 2017), which have also recently been observed with integral-field-units spectroscopy (Davies et al. 2019; Förster Schreiber et al. 2019; Swinbank et al. 2019). The velocity of the relatively cool and warm outflows along the line of sight is estimated with the "down-the-barrel" technique, which measures blueshifts of the absorption lines in the galaxy spectra (Heckman et al. 2000; Schwartz & Martin 2004; Martin 2005; Rupke et al. 2005a,b; Tremonti et al. 2007; Martin & Bouché 2009; Grimes et al. 2009; Alexandroff et al. 2015) Particularly, the absorption lines are used at various redshift: $z \sim 0$ (Chen et al. 2010; Chisholm et al. 2015, 2016b, 2017b; Roberts-Borsani & Saintonge 2019; Concas et al. 2019), $z \sim 1$ (Sato et al. 2009; Weiner et al. 2009; Martin et al. 2012; Kornei et al. 2012; Rubin et al. 2014; Zhu et al. 2015; Du et al. 2016), and $z > 2$ (Shapley et al. 2003; Steidel et al. 2010; Erb et al. 2012; Law et al. 2012; Jones et al. 2013; Shibuya et al. 2014). The outflowing gas far from the galaxy is detected with the absorption lines in the apparently-nearby background-QSO spectra (Bouché et al. 2012; Kacprzak et al. 2014; Muzahid et al. 2015; Schroetter et al. 2015, 2016, 2019).

The outflows are ubiquitously observed in the star-forming galaxies at $z < 2$ (Weiner et al. 2009; Chen et al. 2010; Steidel et al. 2010; Rubin et al. 2014). From their detection rate and inclination study at $z \sim 0$, the opening angle of the outflows are constrained to be $\simeq 60°$ (Figure 1.4 Left, Chen et al. 2010; Martin et al. 2012). Their outflow velocities have a positive correlation with the star formation rate (SFR, Figure 1.4 Right), the stellar mass (M_*), and the SFR surface density ($\Sigma_{\rm SFR}$) (e.g., Rubin et al. 2014; Heckman & Borthakur 2016; Chisholm et al. 2016b), and roughly the correlation is $\propto {\rm SFR}^{0.2-0.3}$ (Rupke 2018).

The "down-the-barrel" technique is also appropriate for outflow studies at $z > 2$. Unlike the emission from the outflows whose detection becomes difficult toward high redshift, the absorption can be detected with a bright background continuum source. Shapley et al. (2003) construct composites of almost 1000 Lyman-break galaxy (LBG) spectra at $z \sim 3$ to discuss the relation between the FUV spectral features and the outflow properties. Recently, Du et al. (2018) report no evolution of central outflow

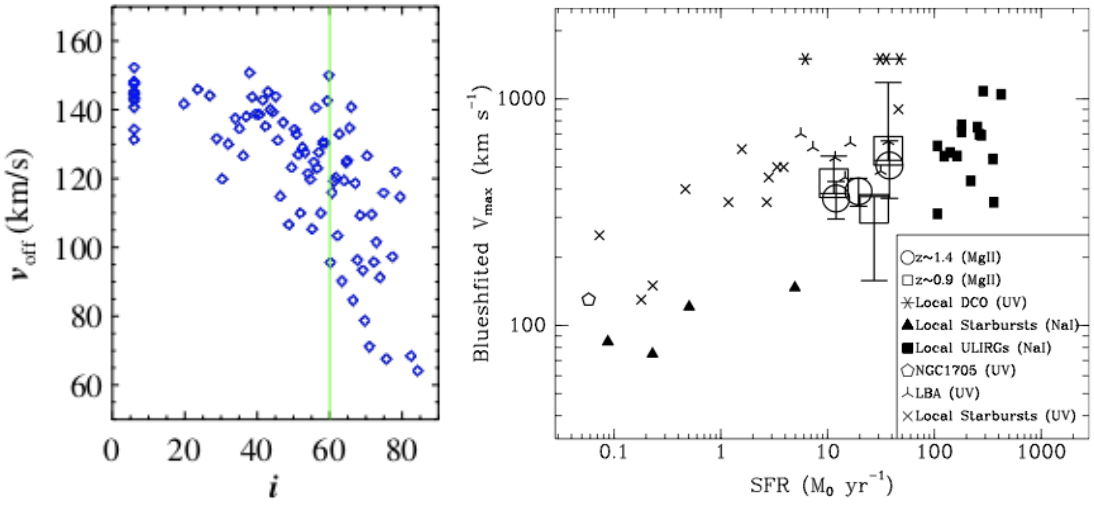

Figure 1.4 **Left**: Outflow Velocity as a function of the galaxy inclination i. The velocity drops at $i = 60°$, which is corresponds to the typical opening angle of the outflows. The figure is taken from Figure 9 of Chen et al. (2010). **Right**: Outflow velocity as a function of SFR, showing a positive correlation between them. The data points are taken from the literature: Martin et al. (2012, square), Weiner et al. (2009, circle), Heckman et al. (2011, asterisk), Schwartz & Martin (2004, triangle), Martin (2005, filled square), Grimes et al. (2009, cross), Heckman et al. (2011, trefoil), and Vázquez et al. (2004, pentagon). The figure is taken from Figure 14 of Martin et al. (2012). These velocities are measured with the "down-the-barrel" methods using the low-ionization absorption lines.

velocities at $z \sim 2$–4 using composites of the rest-frame FUV spectra presented in Steidel et al. (2003, 2004), Reddy et al. (2008), and Jones et al. (2012). Although the Lyα profile provides us the information on the neutral-gas kinematics around Lyman alpha emitters at high redshift (e.g., Erb et al. 2014; Shibuya et al. 2014; Hashimoto et al. 2015; Trainor et al. 2015; Karman et al. 2017), even at $z \sim 6$ (Ajiki et al. 2002), it is difficult to directly estimate the outflow properties only from the Lyα profile due to its strong resonance scattering.

1.4 Scope of This Thesis

1.4.1 Redshift Evolution of Outflow Properties

Despite many observations in a wide redshift range, these results cannot be directly compared because of possible systematic errors in different redshift samples. The literature uses various procedures to measure outflow velocities, including non-parametric (Weiner et al. 2009; Heckman et al. 2015), one-component (Steidel et al. 2010; Kornei et al. 2012; Shibuya et al. 2014; Du et al. 2016), and two-component methods (Martin 2005; Chen et al. 2010; Martin et al. 2012; Rubin et al. 2014). Moreover, we should compare the samples of galaxies in the similar stellar mass range for the apple-to-apple comparison. Although Du et al. (2016) compare outflow velocities of star-forming galaxies at $z \sim 1$ with those at $z \sim 3$ that are derived with the same procedure, Du et al. (2016) cannot make similar galaxy samples at $z \sim 1$ and $z \sim 3$ due to the lack of stellar mass measurements.

The outflow observations at high redshift are challenging. One of the keys to estimate outflow properties is to determine the systemic redshifts of the galaxies. At the low redshift, the systemic redshifts are measured by nebular emission lines (e.g., Hα, [O III], and [O II]), but observations of the emission lines become expensive at high redshift. Some outflow studies at $z > 1.5$ conduct additional near-IR (NIR) observations (Steidel et al. 2010; Shibuya et al. 2014), while others determine the redshifts from Lyα emission or interstellar absorption, which includes the uncertainties based on the outflows (Shapley et al. 2003; Du et al. 2018). Precise measurements of the

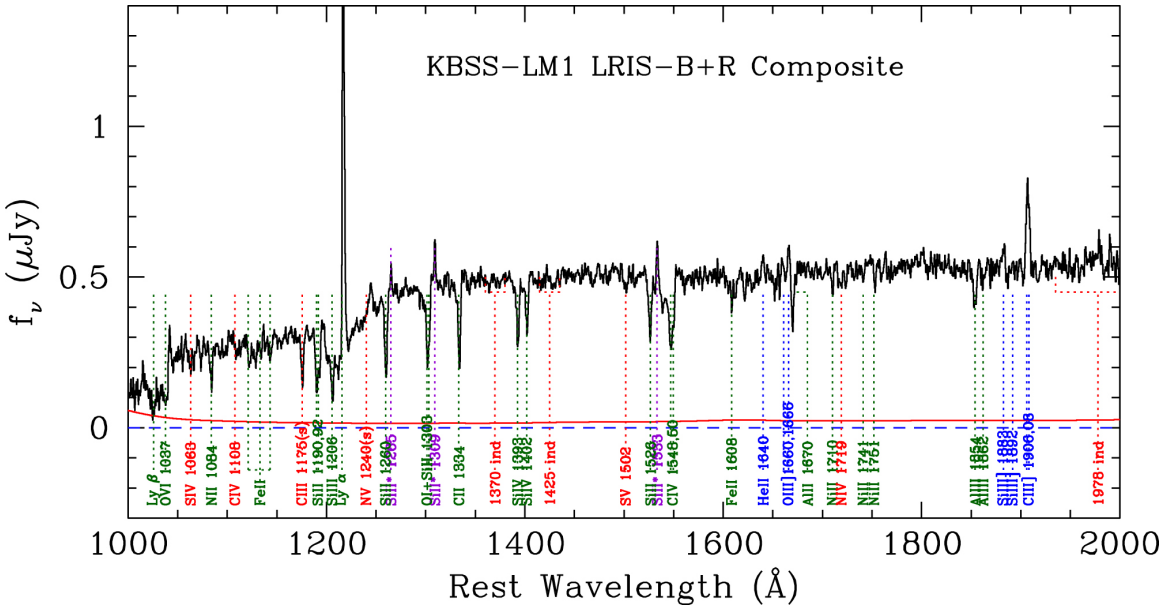

Figure 1.5 Composite spectrum in rest-frame FUV wavelengths in the Keck Baryonic Structure Survey along with MOSFIRE (KBSS-MOSFIRE Steidel et al. 2014). It shows strong emission lines of Lyα and C III], but Lyα is a resonance-scattering line, whose line profile is sensitive to the environment, and C III] is weak to be detected in typical star-forming galaxies. There are no emission lines useful for the determination of the systemic redshift. The figure is taken from Figure 2 of Steidel et al. (2016).

systemic redshifts are more challenging at $z > 5$, where the strong optical emission lines fall into the mid-IR bands. Although there are several nebular emission lines in the rest-frame FUV band such as O III]$\lambda\lambda$1660, 1666 and C III]$\lambda\lambda$1906, 1908, these lines are weak to be detected in typical star-forming galaxies at high redshift (Figure 1.5). This problem makes it difficult to extend the outflow studies to $z > 5$.

1.4.2 Plan of This Thesis

In this thesis, we investigate the redshift evolution of the cool and warm galactic outflows in the star-forming galaxies with large spectroscopic samples and the "down-the-barrel" method. We use spectra of galaxies at $z \sim 0$, 1, and 2 drawn from the Sloan Digital Sky Survey (SDSS; York et al. 2000), the Deep Evolutionary Exploratory Probe 2 (DEEP2) Galaxy Redshift Survey (Davis et al. 2003, 2007; Newman et al. 2013), and Low Resolution Imaging Spectrometer (LRIS) sample (Erb et al. 2006a,b), respectively. For galaxies at $z > 5$, we overcome the technical challenge about the systemic redshifts, by making use of the redshifts determined from observations with the Atacama Large Millimeter/submillimeter Array (ALMA). Recent ALMA observations detect [C II] 158 μm and [O III] 88 μm emission lines in high-z galaxies (e.g., Capak et al. 2015; Inoue et al. 2016; Hashimoto et al. 2019), which enables us to measure the systemic redshifts of the galaxies. Combining the redshift determined from the ALMA observations with deep observed-frame optical spectra, we can address the outflow properties at $z > 5$. As a case study, Pavesi et al. (2016) discuss the rest-frame FUV absorption lines in HZ10, a IR-luminous LBG at $z \simeq 5.6$, and find the blueshifts with respect to the [C II] emission line. The combination of these data sets enables us to study the redshift evolution of outflow velocities in star-forming galaxies with a similar stellar masses.

Chapter 2 explains the theoretical backgrounds of the galactic outflows and relations with observations. Chapter 3 introduces the observational instruments and the spectroscopic catalogs we use in this thesis. Chapter 4 describes the sample selections in this thesis used for galaxies at $z \sim 0$, 1, 2, and 5–6. Chapter 5 explains the analysis of the absorption lines in the observed-frame optical spectra. We obtain composite

spectra of the galaxies to measure outflow velocities by fitting profiles to absorption lines. Chapter 6 shows the results on the measurements of the outflow velocities and their redshift evolution. Chapter 7 discusses relations between the outflow and galaxy properties, the mass of the outflows, and the escape fraction of the ionizing photons. Chapter 8 summarizes our conclusions.

We calculate stellar masses and SFRs by assuming a Chabrier (2003) initial mass function (IMF). The ΛCDM cosmology is used throughout this thesis: $\Omega_{\rm M} = 0.27$, $\Omega_\Lambda = 0.73$, $h = H_0/(100\ {\rm km\ s^{-1}\ Mpc^{-1}}) = 0.70$, $n_s = 0.95$, and $\sigma_8 = 0.82$. All transitions are referred to by their wavelengths in vacuum. Magnitudes are in the AB system.

CHAPTER 2
THEORETICAL BACKGROUNDS

2.1 Driving Mechanisms of Outflows

There are two well-known driving mechanisms of outflowing gas: the momentum-driven (Murray et al. 2005) and energy-driven (Chevalier & Clegg 1985) models. These models provide simple analytic relations between the halo circular velocity $v_{\rm cir}$ and the mass loading factor η, which is the ratio of the mass outflow rate $\dot{M}_{\rm out}$ to SFR:

$$\eta = \frac{\dot{M}_{\rm out}}{\rm SFR}, \tag{2.1}$$

where $\dot{M}$ is the mass rate of the outflowing gas per year. Since SFR is an indicator of the energy and momentum rate produced by SNe, η represents how effectively the outflows carry the mass out. In this section, we briefly describe the derivation of η in both models, on the basis of the discussion shown by Murray et al. (2005).

2.1.1 Momentum-Driven Model

The ISM in a galaxy is accelerated by the radiation pressure from starburst or the ram pressure of the hot fluid produced from SNe in the central region of the galaxy. This process is referred as the momentum-driven model. In the momentum-driven model, because the momentum of the outflowing gas is input from the galaxy, $\dot{M}_{\rm out}$ is given by

$$\dot{M}_{\rm out} V_\infty \simeq \dot{p}, \tag{2.2}$$

where $\dot{p}$ is the total momentum deposition rate from the star-forming activity, and V_∞ the terminal outflow velocity. We assume that the terminal outflow velocity is comparable to the halo circular velocity: $V_\infty \sim v_{\rm cir}$.

The momentum deposition from the hot fluid by SNe can be order-estimated. Under the assumptions of $m_{\rm SN} \simeq 10$ M$_\odot$ materials produced by a individual SN at the velocity of $v_{\rm SN} \simeq 3000$ km s^{-1}, and the frequency of SNe per unit mass of star

formation is $\nu \sim \mathrm{SFR}/(100\ M_\odot)$, the typical momentum deposition rate by SNe is

$$\dot{p}_{\mathrm{SN}} = m_{\mathrm{SN}} v_{\mathrm{SN}} \nu \sim 300\ \mathrm{SFR}\ [\mathrm{M_\odot\ yr^{-1}\ km\ s^{-1}}] \tag{2.3}$$

$$= 2 \times 10^{33} \left(\frac{\mathrm{SFR}}{1\ \mathrm{M_\odot\ yr^{-1}}} \right) [\mathrm{dyn}]. \tag{2.4}$$

The total luminosity of the central starburst L_{SB} is expressed as

$$L_{\mathrm{SB}} = \epsilon c^2 \mathrm{SFR}, \tag{2.5}$$

where c is the speed of light, and ϵ is the conversion efficiency. In the starburst models of Leitherer et al. (1999) and Bruzual & Charlot (2003), the value of ϵ is calculated to be $\epsilon \sim 10^{-3}$ for a Salpeter (1955) IMF. The radiation pressure by the starbursts $\dot{p}_{\mathrm{SB}}$ is connected with the luminosity L_{SB}/c in the point-source, single-scattering limit case, and thus

$$\dot{p}_{\mathrm{SB}} \simeq L_{\mathrm{SB}}/c = \epsilon c \sim 300\ \mathrm{SFR}\ [\mathrm{M_\odot\ yr^{-1}\ km\ s^{-1}}]. \tag{2.6}$$

Equations (2.3) and (2.6) show that the momentum input from SNe and starbursts are comparable.

Comparing Equations (2.2)–(2.6), we obtain the mass loading factor η with the dependency on v_{cir}:

$$\eta \equiv \frac{\dot{M}_{\mathrm{out}}}{\mathrm{SFR}} \sim \frac{\epsilon c}{V_\infty} \propto v_{\mathrm{cir}}^{-1}. \tag{2.7}$$

This scaling relation is shown in Figure 2.1 with the blue line.

2.1.2 Energy-Driven Model

The ISM can be heated and accelerated by thermal pressure made by the core-collapse SNe. This process is described with the energy-driven model. In the energy-driven model, $\dot{M}_{\mathrm{out}}$ is estimated by

$$\frac{1}{2} \dot{M}_{\mathrm{out}} V_\infty^2 \simeq \dot{E}, \tag{2.8}$$

where $\dot{E}$ is the total energy deposition rate by SNe. Because the energy released from an individual SN is $E_{\rm SN} \sim 10^{51}$ erg, the energy rate produced by starbursts is

$$\dot{E}_{\rm int} \sim \nu E_{\rm SN} = 3 \times 10^{41} \left(\frac{\rm SFR}{1\ {\rm M}_\odot\ {\rm yr}^{-1}} \right) {\rm erg\ s}^{-1}. \tag{2.9}$$

This energy released from an SN is two magnitude lower than the luminosity of the starbursts (Equation 2.4 and 2.6), indicating that an SN releases 1% of the energy which a massive star emits throughout its lifetime. Hence, with the efficiency of energy transfer to the ISM ξ, the energy deposition rate from SNe is written as

$$\dot{E} = \xi \dot{E}_{\rm int} \simeq 10^{-2} \xi L_{\rm SB}. \tag{2.10}$$

Comparing Equations (2.7), (2.8), and (2.10), η is described as

$$\eta \sim \frac{\xi \epsilon 10^{-2} c^2}{V_\infty^2} \propto {v_{\rm cir}}^{-2}. \tag{2.11}$$

This scaling relation is shown in Figure 2.1 with the red line.

2.2 Analytical Models of the Outflow Velocity

Heckman et al. (2015) describe a simple analytical model of acceleration of a gas cloud whose cross section and mass is $A_{\rm c}$ and $M_{\rm c}$, respectively. Driving force of radiation pressure and hot fluid acts on the cloud by

$$F_{\rm out} = \dot{p_*} \frac{A_{\rm C}}{4\pi r^2}, \tag{2.12}$$

where p_* is the momentum flux given by the radiation pressure and the ram pressure of the hot fluid. The p_* value is $\sim 10^{33} ({\rm SFR/M}_\odot\ {\rm yr}^{-1})$ dyn (Equation 2.4). Heckman et al. (2015) calculate the momentum flux given by the starburst and SNe based on a stellar synthesis model, Starburst 99 (Leitherer et al. 1999). The calculated momentum flux is $\dot{p}_* = 4.8 \times 10^{33} ({\rm SFR/M}_\odot\ {\rm yr}^{-1})$ dyn, and the ratio of the momentum flux contributed by the hot fluid and radiation pressure is about 2.5.

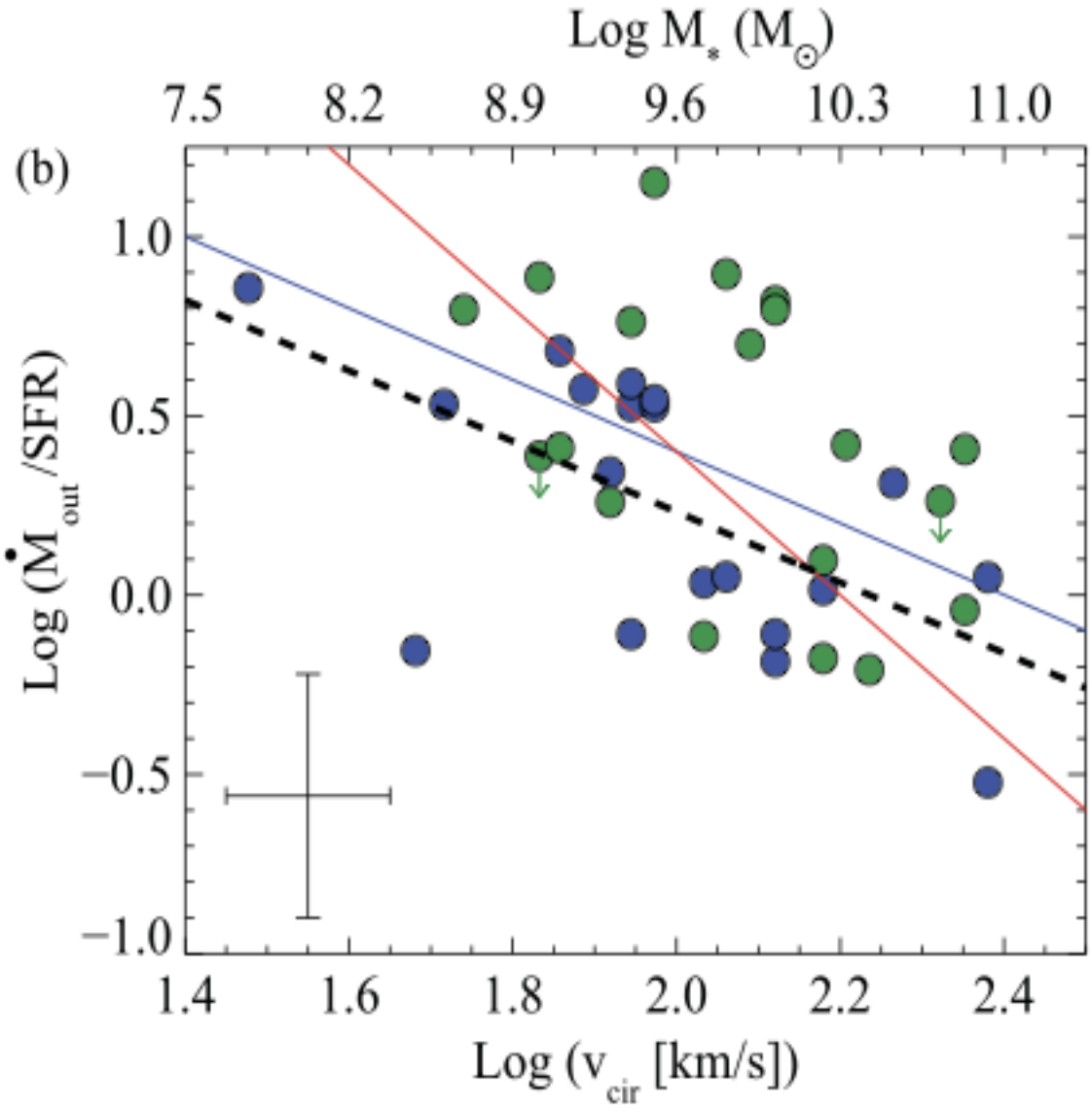

Figure 2.1 Mass loading factor as a function of the halo velocity. The blue and red lines represents the scaling of the momentum-driven (Equation 2.7) and energy-driven (Equation 2.11) models, respectively. The data points denotes measurements of local starbursts given by Heckman et al. (2015) and the dashed line is the least-square best-fit relation to the strong outflows (blue circle). The typical error bars are shown in the cross at the left bottom. The figure is taken from Figure 11 of Heckman et al. (2015).

The gravitational force is

$$F_{\rm in} = G\frac{M(<r)M_{\rm c}}{r^2} = \frac{M_{\rm c}v_{\rm cir}^2}{r}, \tag{2.13}$$

where G is gravitational constant, $M(<r)$ the mass within the galactocentric radius r, and $v_{\rm cir}(r) = \sqrt{GM_*/r}$ the circular velocity at the distance r.

When the cloud is located at the galaxy effective radius r_* along the minor axis of the galaxy with zero velocity, a condition of the acceleration of the cloud outward is $F_{\rm out} > F_{\rm in}$. The critical value of $\dot{p}_*$ is derived as

$$\dot{p}_{\rm crit} = \frac{4\pi r_* M_{\rm c} v_{\rm cir}^2}{A_{\rm c} r_*} = 4\pi r_* N \langle m \rangle v_{\rm cir}^2. \tag{2.14}$$

Here we assume $M_{\rm c} = A_{\rm c} N \langle m \rangle$, where N is the cloud column density, $\langle m \rangle$ the averaged particle mass. When N is constant, $\dot{p}_{\rm crit} \propto r_* v_{\rm cir}^2$.

Solving the equation of motion of the cloud, we obtain the cloud velocity $v_{\rm c}$ at the galactocentric radius r as

$$\frac{v_{\rm c}(r)}{v_{\rm cir}} = \sqrt{2}\left[\left(1-\frac{r_*}{r}\right)\left(\frac{\dot{p}_*}{\dot{p}_{\rm crit}}\right) - \ln\left(\frac{r}{r_*}\right)\right]^{1/2}. \tag{2.15}$$

Figure 2.2 shows the solutions of Equation (2.15) in the case of $\dot{p}_*/\dot{p}_{\rm crit} = 2.5$, 5, 10, 20, and 40. When $\dot{p}_*/\dot{p}_{\rm crit}$ is larger than 10, the outflows can reach a distance of $\log(r/r_*) > 3.0$. Because the momentum flux $\dot{p}_* \propto$ SFR, $\dot{p}_*/\dot{p}_{\rm crit}$ is proportional to SFR$/r_* v_{\rm cir}^2$. Equation (2.15) has the velocity peak at $r/r_* = \dot{p}_*/\dot{p}_{\rm crit}$, where the maximum velocity $v_{\rm max}$ is

$$\frac{v_{\rm max}}{v_{\rm cir}} = \sqrt{2}\left[\left(\frac{\dot{p}_*}{\dot{p}_{\rm crit}}-1\right) - \ln\left(\frac{\dot{p}_*}{\dot{p}_{\rm crit}}\right)\right]^{1/2}. \tag{2.16}$$

In convenient units, $v_{\rm max}$ is $\simeq 330$ km s^{-1} for $\dot{p}_*/\dot{p}_{\rm crit} = 5$ and $v_{\rm cir} = 150$ km s^{-1}. In the case of $\dot{p}_*/\dot{p}_{\rm crit} \gg 1$, the second term in Equation (2.16) become $\ll 1$ and

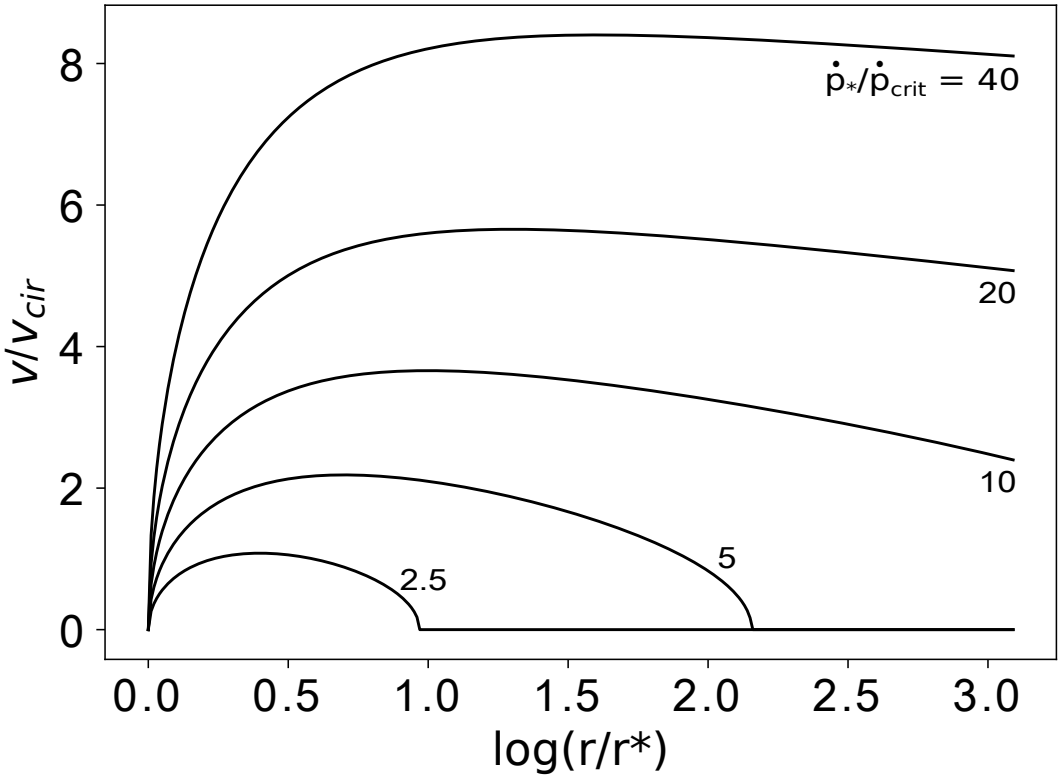

Figure 2.2 Outflow velocity as a function of galactocentric radius represented in Equation (2.15), for each $\dot{p}_*/\dot{p}_{\rm crit}$. If $\dot{p}_*/\dot{p}_{\rm crit} \ll 10$, the outflows cannot escape the gravity of the galaxy farther than $r/r_* > 10^2$.

Equation (2.16) can be rewritten as

$$\frac{v_{\rm max}}{v_{\rm cir}} \sim \sqrt{2}\left(\frac{\dot{p}_*}{\dot{p}_{\rm crit}}\right)^{1/2}. \tag{2.17}$$

Because $\dot{p}_*/\dot{p}_{\rm crit}$ is proportional to ${\rm SFR}/r_* v_{\rm cir}^2$, we obtain

$$v_{\rm max} \propto \left(\frac{\rm SFR}{r_*}\right)^{1/2}. \tag{2.18}$$

2.3 Characterizing Outflows by Observations

2.3.1 Optical Depth and Covering Factor

To estimate the physical parameters of the outflows from observations, we need to specify the energy that is carried by photons from the galaxies. We define the specific intensity $I(\lambda)$, the energy density of photons in unit wavelength range around wavelength λ that pass through unit area within unit solid angle during unit time. When photons are absorbed by matter, the loss of $I(\lambda)$ along a distance $\mathrm{d}s$ is expressed with the absorption coefficient κ_λ:

$$\frac{\mathrm{d}I(\lambda)}{\mathrm{d}s} = -\kappa_\lambda I(\lambda). \tag{2.19}$$

When we use the optical depth τ_λ that is defined by

$$\mathrm{d}\tau(\lambda) = -\kappa_\lambda \mathrm{d}s, \tag{2.20}$$

Equation (2.19) is integrated along the pass of the photons and become

$$I(\lambda) = I_0(\lambda) e^{-\tau(\lambda)}, \tag{2.21}$$

where $I_0(\lambda)$ is the specific intensity of the source before the absorption of the matter. If there are sight lines with no absorption, we can rewrite Equation (2.21) as

$$I(\lambda) = I_0(\lambda)(1 - C_f(\lambda) + C_f(\lambda) e^{-\tau(\lambda)}), \tag{2.22}$$

where $C_f(\lambda)$ is the covering factor, the fraction in which the matter covers the sight line.

If the photons pass through some layers of matter, $I(\lambda)$ is given by

$$I(\lambda) = I_0(\lambda) \prod_k i_k(\lambda), \tag{2.23}$$

$$i_k(\lambda) = 1 - C_{i,f}(\lambda) + C_{i,f}(\lambda) e^{-\tau_i(\lambda)}, \tag{2.24}$$

where $i_k(\lambda)$ is the intensity after unit intensity pass through each layer, and $C_{k,f}$ and $\tau_k(\lambda)$ are the covering factor and the optical depth of $i_k(\lambda)$, respectively.

2.3.2 Column Density

If the dynamics in the matter is the thermal motions, we can obtain the column density of the matter from the absorption line profile. In this subsection, we follow the description in Spitzer (1978).

The absorption efficient is related to the particle number density n by

$$\kappa_\lambda = n\sigma_\lambda = n\sigma\phi(\lambda), \tag{2.25}$$

where σ_λ is the absorption cross section per particle per wavelength. If we use the profile $\phi(\lambda)$ whose integral over the wavelength is unity, we obtain the right-hand side of Equation (2.25), where σ is the integral absorption cross section over the wavelength. The column density N is defined by

$$N = \int n \mathrm{d}s, \tag{2.26}$$

whose the range of integration is over the distance along the sight line. If we integrate Equation (2.25) along the sight line, we have the following expression based on Equations (2.20) and (2.26):

$$\tau(\lambda) = N\sigma\phi_a(\lambda), \tag{2.27}$$

where $\phi_a(\lambda)$ is the line profile function that is the average of $\phi(\lambda)$ along the sight line.

If stimulated emission is ignored, the integral absorption cross section is given by

$$\sigma = \frac{\pi e^2 \lambda_0^2}{m_e c^2} f, \tag{2.28}$$

where c is the speed of light, e is the elementary charge, m_e is the mass of an electron, f is the oscillator strength of the absorption line, and λ_0 is the central wavelength of

the line profile. If the line profile function is a Gaussian function, $\phi_a(\lambda)$ becomes

$$\phi_a(\lambda) = \frac{c}{\sqrt{\pi} b_D \lambda_0} e^{-(v/b_D)^2}, \tag{2.29}$$

$$v = \frac{\lambda - \lambda_0}{\lambda_0} c, \tag{2.30}$$

where b_D is the Doppler parameter. Now we define the optical depth by the simple equation

$$\tau(\lambda) \equiv \tau_0 e^{-(v/b_D)^2}, \tag{2.31}$$

where τ_0 is the optical depth at the line center. Comparing Equations (2.27) and (2.31), we obtain the expression of τ_0 with Equations (2.28) and (2.29) by

$$\tau_0 = \frac{\sqrt{\pi} e^2 N f \lambda_0}{m_e c}. \tag{2.32}$$

If we substitute the values of the physical constants in Equation (2.32), the column density is given by

$$N = \frac{\tau_0 b}{1.497 \times 10^{-15} \lambda_0 f}. \tag{2.33}$$

2.3.3 Outflow Velocity

In Sections 2.3.3 and 2.3.4, we describe the properties of outflowing gas from galaxies. When the ISM clouds are going out of a galaxy, these ISM clouds give rise to blue-shifted absorption lines in the galaxy spectrum. Given the central wavelength of a blue-shifted absorption line $\lambda_{\rm out}$, the velocity of the outflowing cloud is given by

$$v_{\rm out} = \frac{c(\lambda_{\rm out} - \lambda_{\rm rest})}{\lambda_{\rm rest}}, \tag{2.34}$$

where $\lambda_{\rm rest}$ is the rest-frame wavelength of the absorption line.

2.3.4 Mass Loading Factor

We write this subsection, referring Rupke et al. (2002, 2005b). To estimate the mass outflow rate $\dot{M}_{\rm out}$, we assume the spherical continuous outflow model, which assumes

the bi-conical outflow whose solid angle subtended by the outflowing gas is given by Ω. The mass of the outflowing gas $M_{\rm out}$ at radius r is

$$\frac{{\rm d}M_{\rm out}}{{\rm d}r} = \bar{m}_p \Omega C_f r^2 n({\rm H}), \tag{2.35}$$

where $\bar{m}_p$ is the mean atomic weight and n(H) is the number density of hydrogen. If the outflow mass is constant at any radius, the left-hand term of Equation (2.35) is simplified by

$$\frac{{\rm d}M_{\rm out}}{{\rm d}r} = \frac{M_{\rm out}}{r_2 - r_1}, \tag{2.36}$$

where r_1 and r_2 are the inner and outer radii of the outflow, respectively. We divide Equation (2.35) by r^2 and integrate it from r_1 to r_2, with Equations (2.26) and (2.36). We thus obtain

$$M_{\rm out} = \bar{m}_p \Omega C_f r_1 r_2 N({\rm H}), \tag{2.37}$$

where N(H) is the column density of hydrogen, and Ω and C_f are assumed to be independent of the radius. Given the typical outflow velocity $v_{\rm out}$, the outflow lifetime $t_{\rm out}$ is defined by

$$t_{\rm out} \equiv \frac{r_2}{v_{\rm out}}. \tag{2.38}$$

If we divide $M_{\rm out}$ by $t_{\rm out}$, we have

$$\dot{M}_{\rm out} = \bar{m}_p \Omega C_f r_1 N({\rm H}) v_{\rm out}. \tag{2.39}$$

In this way, we obtain $\dot{M}_{\rm out}$ to derive η with Equation (2.1).

CHAPTER 3
OBSERVATIONAL INSTRUMENTS AND DATA

To study galactic outflows, we construct four samples at $z \sim 0$–6. A $z \sim 0$ sample is drawn from the SDSS Data Release 7 (DR7; Abazajian et al. 2009), a $z \sim 1$ sample is drawn from the DEEP2 DR 4 (Newman et al. 2013), a $z \sim 2$ sample is drawn from Erb et al. (2006a), and a $z = 5$–6 sample is drawn from Capak et al. (2015). In this chapter, we describe the telescope, instruments, and spectroscopic catalogs used in this thesis.

3.1 SDSS Telescope

The SDSS telescope is a modified two-corrector Ritchey-Chrétien telescope located at Apache Point Observatory in New Mexico (Figure 3.1). With a 2.5 m and f/2.25 primary mirror, a 1.08 m secondary mirror, and two corrector lenses, the telescope accomplishes 3° diameter (0.65 m) focal plane that covers a wide range of wavelengths from 3,000 to 10,600 Å (Gunn et al. 2006). The SDSS consists of wide-field survey programs that study stars, galaxies, and cosmology (York et al. 2000). There are ten survey programs that have been conducted in four phases since 2000. Prior surveys are the SDSS Legacy Survey, the SDSS Supernova Survey, the Sloan Extension for Galactic Understanding and Exploration (SEGUE), SEGUE-2, the Multi-Object APO Radial Velocity Exoplanet Large-area Survey (MARVELS), the Baryon Oscillation Spectroscopic Survey (BOSS), and APO Galaxy Evolution Experiment (APOGEE). The fourth phase of the SDSS (SDSS-IV) are comprised of the three surveys: The Extended BOSS (eBOSS), APOGEE-2, and Mapping Nearby Galaxies at APO (MaNGA).

3.1.1 SDSS-I/-II Spectrograph

The SDSS-I/-II spectrographs are installed at the Cassegrain focus of the SDSS telescope and used in the SDSS Legacy Survey (Figure 3.1). The spectrographs take 640 spectra at a time, with the corresponding fibers of 3″ diameter, which are plugged into

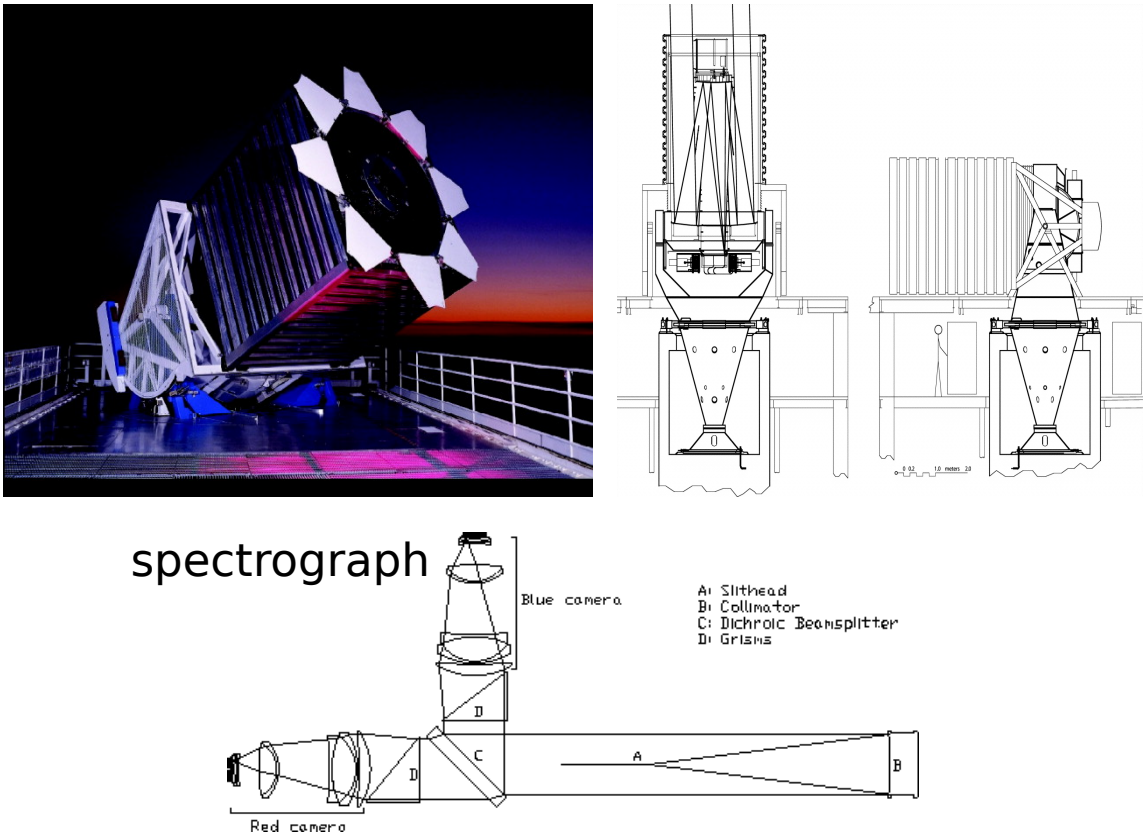

Figure 3.1 Top left: Picture of the SDSS telescope. This figure is taken from Figure 2 of Gunn et al. (2006). Top right: Structure of the SDSS telescope. This figure is also taken from Figure 12 of Gunn et al. (2006). Bottom: Optical design of the SDSS-I/-II spectrographs. This figure is taken from the Project Book.

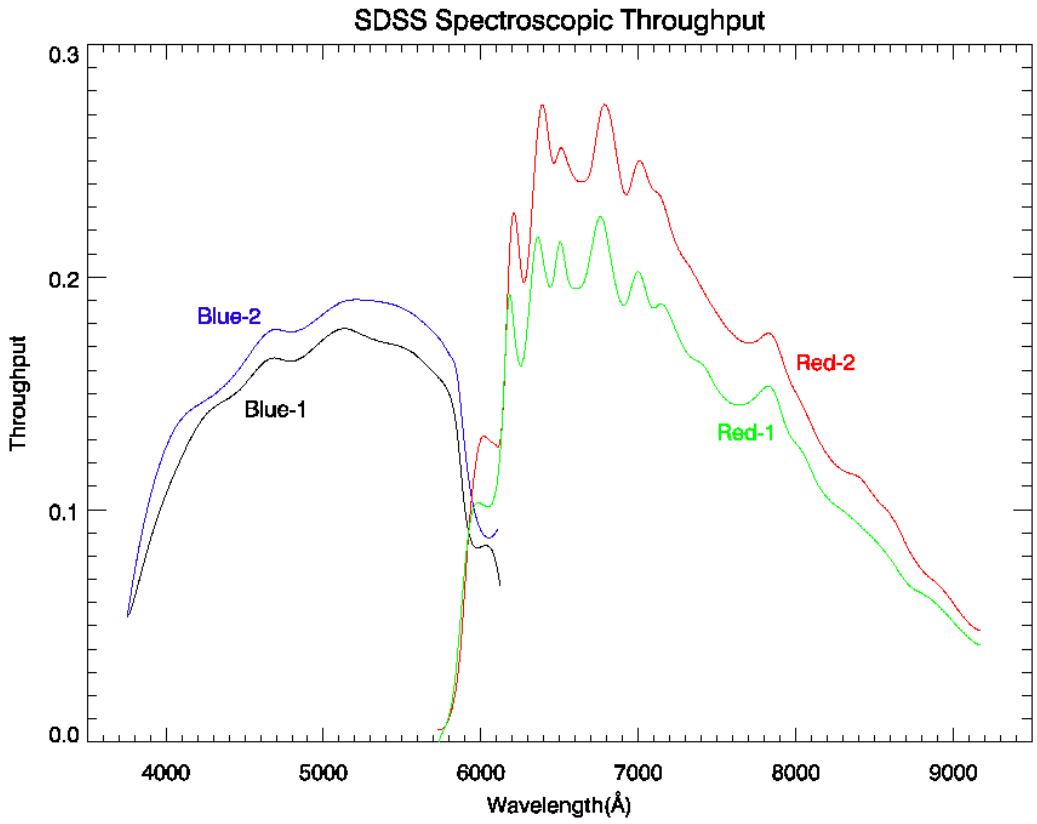

Figure 3.2 Throughput curves of the SDSS-I/-II spectrographs. The blue and red curves show the throughputs of the blue and red spectrographs, respectively. This figure is taken from http://classic.sdss.org/dr7/instruments/spectrographs/index.html .

holes in an aluminum plate. The collected light is transmitted to two spectrographs that cover 3800-6150Å (blue) and 5800-9200Å (red). The throughput curves of the two spectrographs are shown in Figure 3.2. The spectral resolution ranges from 1850 to 2200. (See Section 7 of the Project Book[1] for more details.)

3.1.2 SDSS Legacy Survey

We use spectra taken by the SDSS Legacy Survey, which takes >10,000 deg^2 images and 1.6 million spectra. We select star-forming galaxies at $z \sim 0$ from the SDSS DR7 (Abazajian et al. 2009) main galaxy sample (Strauss et al. 2002), which contains

[1]http://www.astro.princeton.edu/PBOOK/welcome.htm

galaxies with extinction-corrected Petrosian r magnitude in a range of $14.5 < r < 17.5$. The spectra of these galaxies have a mean spectral resolution of $R \sim 2000$, a dispersion of 69 km s^{-1} pixel^{-1}, and a wavelength coverage spanning between 3800 and 9200 Å. These spectra are taken with 3″-diameter fibers placed at the centers of galaxies. The SDSS imaging data are taken through a set of u, g, r, i, and z filters (Fukugita et al. 1996) using a drift-scanning mosaic CCD camera (Gunn et al. 1998).

3.2 Keck Telescopes

The twin Keck Telescopes are two of the largest optical telescopes, which are placed on the summit of Maunakea in Hawai'i. The two telescopes are referred to as Keck I and II. The each primary mirror is composed of 36 hexagonal mirrors, which accomplish the effective diameter of 10 meters. Figure 3.3 illustrates the structure of the Keck telescopes.

Each telescope equips four main instruments for observations: the High Resolution Echelle Spectrometer (HIRES), the Low Resolution Imaging Spectrometer (LRIS), the Multi-Object Spectrometer For Infra-Red Exploration (MOSFIRE), and the OH-Suppressing Infra-Red Imaging Spectrograph (OSIRIS) on Keck I; the DEep Imaging Multi-Object Spectrograph (DEIMOS), the Echellette Spectrograph and Imager (ESI), the Near-Infrared Camera 2 (NIRC2), and the Near-Infrared Spectrometer (NIRSPEC) on Keck II. We use spectra taken by the LRIS on Keck I and the DEIMOS on Keck II.

3.2.1 LRIS

The LRIS is installed at the Cassegrain focus of the Keck-I telescope (Oke et al. 1995). The left bottom panel of Figure 3.3 illustrates the structure of the LRIS. The LRIS is composed of the red and blue channels that take spectra (or images) simultaneously in a wavelength range of 3200–10,000 Å (Steidel et al. 2004; Rockosi et al. 2010). The field of view is $6' \times 7.8'$. The available imaging filters are U, B, V, G, R, and I bands plus a small number of narrow bands.

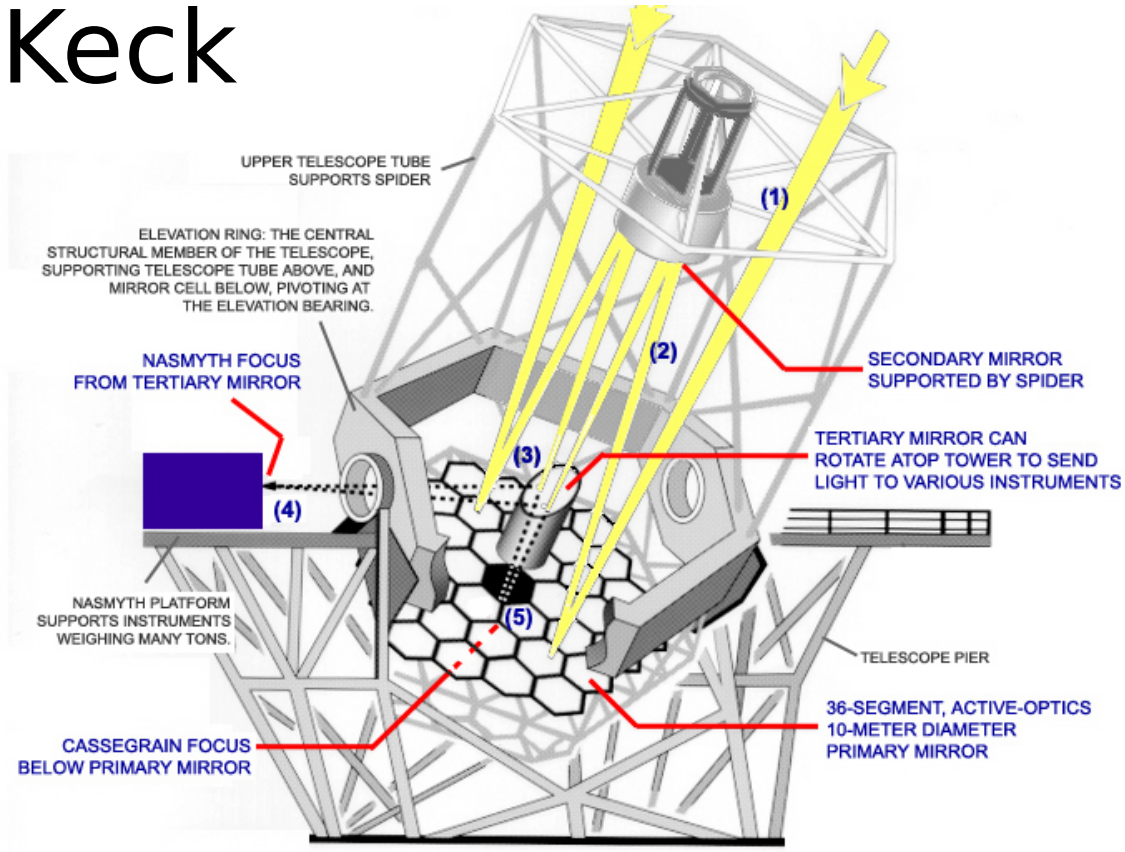

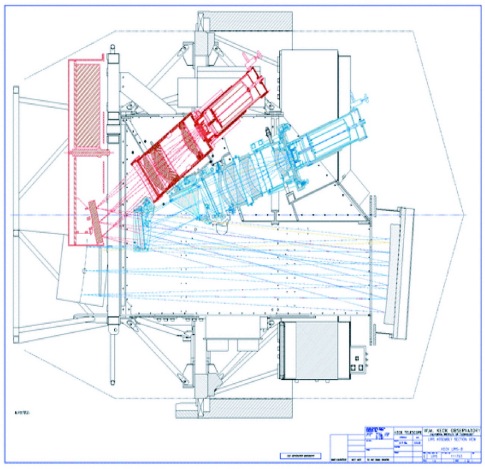

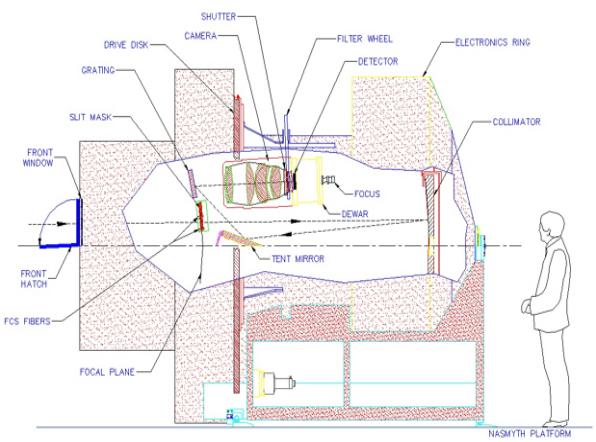

Figure 3.3 Top: Structure of the Keck telescope. Bottom left: Optical configurations of the LRIS. The LRIS is installed at the Cassegrain focus, the position (5) of the top figure. Bottom right: The internal structure of the DEIMOS. The DEIMOS is installed at the Nasmyth focus, the position (4) of the top figure. These figures are taken from http://spacecraftkits.com/KFacts2.html (Top), Figure 10 of Steidel et al. (2004) (Bottom left), and http://www2.keck.hawaii.edu/inst/deimos/ (Bottom right).

The spectra we use in this thesis are taken with the spectrograph of the blue channel of the LRIS (LRIS-B). The LRIS-B takes spectra in the longslit or multi-object spectroscopy (MOS) modes, and employs the four grisms, 300/5000, 400/3400, 600/4000, and 1200/3400. The throughput curves of the grism are shown in Figure 3.4. We use the spectra taken with the 400/3400 grism, which provides dispersion of 1.09 Å/pixel in 3000–4300 Å and FWHM resolution of 6.5–7.1 Å.

3.2.2 LRIS galaxies at $z \sim 2$

We use spectra in the Erb et al. (2006a) catalog for our sample at $z \sim 2$. The catalog consists of BX/BM (Adelberger et al. 2004; Steidel et al. 2004) and MD (Steidel et al. 2003) galaxies, which are originally in the rest-frame UV-selected sample described by Steidel et al. (2004). The rest-frame UV spectra of galaxies are taken with the LRIS. The galaxies are also taken with the NIR spectra, mainly with NIRSPEC (McLean et al. 1998) at Keck II telescope, for Hα emission lines of them at $z \sim 2$.

We download raw LRIS data of the galaxies from the Keck Observatory Archive[2] (KOA). We reduce the data with the `XIDL LowRedux`[3] pipeline. The Right ascension (R.A.) and declination (Decl.) of each galaxy are computed from the pixel positions and the fits header of the data with the program `COORDINATES`[4]. We find systematics of about 20″ between the real coordinates and outputs by `COORDINATES`. In the images where several galaxies are observed at a time, we correct R.A. and Decl. of objects to be consistent with coordinates listed in the Erb et al. (2006a) catalog.

3.2.3 DEIMOS

The DEIMOS is installed at the Nasmyth focus of the Keck-II telescope (Faber et al. 2003). The right bottom panel of Figure 3.3 illustrates the structure of the DEIMOS. The field of view is 3.6′×3.6′. The available filters are, at present, B, R, I, and Z for imaging and GG400, GG455, GG495, and OG550 for spectroscopy. The DEIMOS

[2]KOA website: http://www2.keck.hawaii.edu/koa/public/koa.php.
[3]The XIDL LowRedux is available at http://www.ucolick.org/~xavier/LowRedux/
[4]`COORDINATES` is available at http://www2.keck.hawaii.edu/inst/lris/coordinates.html

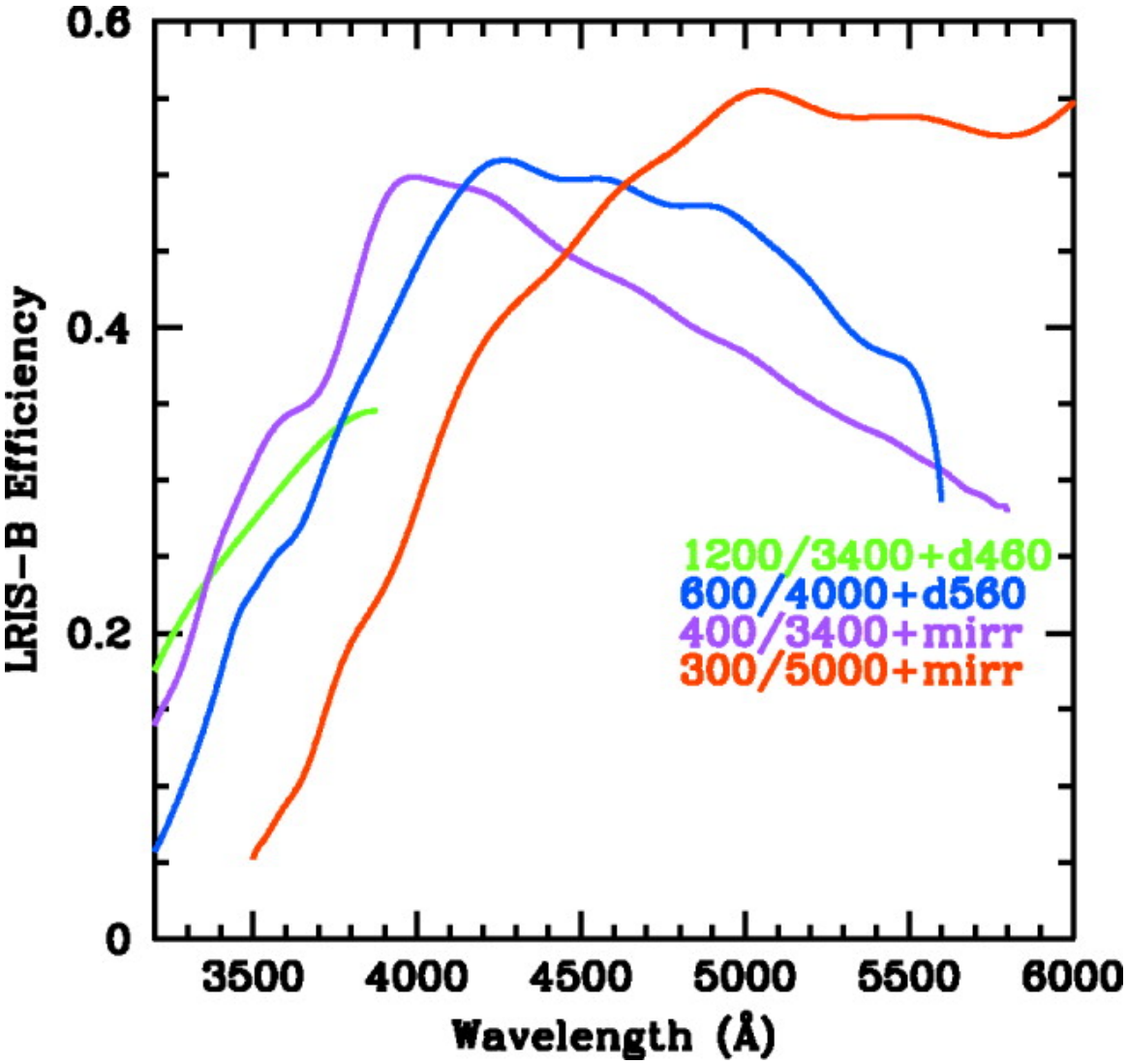

Figure 3.4 Throughput curves of the LRIS-B. The colors depends on grisms as shown in the legend. This figure is taken from Figure 11 of Steidel et al. (2004).

employs the four gratings, 600, 830, 900, and 1200 lines mm^{-1}, and covers the spectral wavelength range of 4100–11000 Å. The throughput curves of 1200 lines mm^{-1} grating with various fileters are shown in Figure 3.5.

3.2.4 DEEP2 Galaxy Redshift Survey

Our galaxy sample at $z \sim 1$ is taken from a large spectorosocpic catalog of the DEEP2 DR4 (Newman et al. 2013) [5]. The survey is conducted with the DEIMOS (Faber et al. 2003). The DEEP2 survey targets galaxies with a magnitude limit of $18.5 < R_{\mathrm{AB}} < 24.1$ in four fields of the Northern Sky. In three of the four fields, the DEEP2 survey preselects these galaxies with B, R, and I band photometry taken with 12K camera at the Canada-France-Hawaii Telescope to remove galaxies at $z < 0.7$ (Coil et al. 2004). We use the spectra taken with the 1200 lines mm^{-1} grating, the OG550 filter blazed at 7500 Å and 1.″0 slits. This setting gives the spectral resolution of $R \sim 5000$, corresponding to a dispersion of 0.33 Å/pixel. The wavelength ranges from 6500 to 9100 Å. The public data are reduced with the DEEP2 DEIMOS Data pipeline (the `spec2d` pipeline), developed by the DEEP2 Redshift Survey team (Newman et al. 2013; Cooper et al. 2012).

We execute the pipeline written in `IDL` for the flux calibration of the DEEP2 spectra (Newman et al. 2013). The pipeline corrects spectral fluxes for the overall throughput, chip-to-chip variations, and telluric contamination. After these corrections, the pipeline calibrate fluxes with the R- and I-band photometry. The flux calibration is accurate to 10% or better. Since the routines can not calibrate some spectra correctly, we exclude the spectra from our sample.

3.2.5 Lyman Break Galaxies at $z = 5$–6

Our sample at $z = 5$–6 consists of seven galaxies whose spectra are taken in the optical and millimeter wavelengths. We use the galaxies presented in Capak et al. (2015), who observe nine LBGs and one low-luminosity QSOs at $z \sim 5$–6 in the Cosmic Evolution Survey (COSMOS; Scoville et al. 2007) field. Capak et al. (2015)

[5] The DEEP2 DR4 is available at http://deep.ps.uci.edu/DR4/home.html

obtain the rest-frame FUV spectra of the galaxies with the DEIMOS (Faber et al. 2003). The spectroscopic configuration is the 830 lines mm^{-1} grating with the OG550 filter, which gives the wavelength coverage of 6000–9500 Å and the spectral resolution of $R \sim 2500$–3500. The total integration time is ∼3.5 hr for each object.

We download raw DEIMOS data of the galaxies from the KOA and reduce the raw data the DEIMOS `spec2d` pipeline. From the reduced two-dimensional multi-object-slit data, the pipeline extracts the one-dimensional spectra of the science targets. Finally, we obtain the rest-frame FUV spectra of seven out of the nine LBGs in Capak et al. (2015), other than two objects (HZ3 and HZ9) whose spectra we could not identify from the archive.

3.3 Data Reduction

We reduce the LRIS and DEIMOS spectra with the `IDL` pipelines developed for the two instruments, respectively. Although the details are different, a large part of the reduction flow is identical for LRIS and DEIMOS spectra and the reduction process for SDSS spectra is based on the same idea. Here we describe the LRIS reduction process. The first step is to prepare information required for corrections of spectra. This step uses the multiple flat frames and the arc frames. The flat frames are used for a correction of pixel-to-pixel variations and for the detection of edges of multiple 2D spectra along slitlets. The arc frames provide 2D wavelength solutions by the cross-correlation with the arc intensity templates whose wavelengths are already known.

Figure 3.6 shows a row science image of the multiple object spectroscopy taken by the LRIS. The pixel values in the 2D spectra along the slitlets show signals detected in the CCDs including target-object fluxes, sky fluxes, thermoelectric current, cosmic rays, and biases. The thermoelectric current can be ignored because the LRIS and DEIMOS keep their temperatures of $-120°C$ and $-115°C$, respectively. The pixels which include the cosmic-ray signals are masked. When the biases are subtracted, the pixel values N, corresponding to the electron counts, will be expressed with the

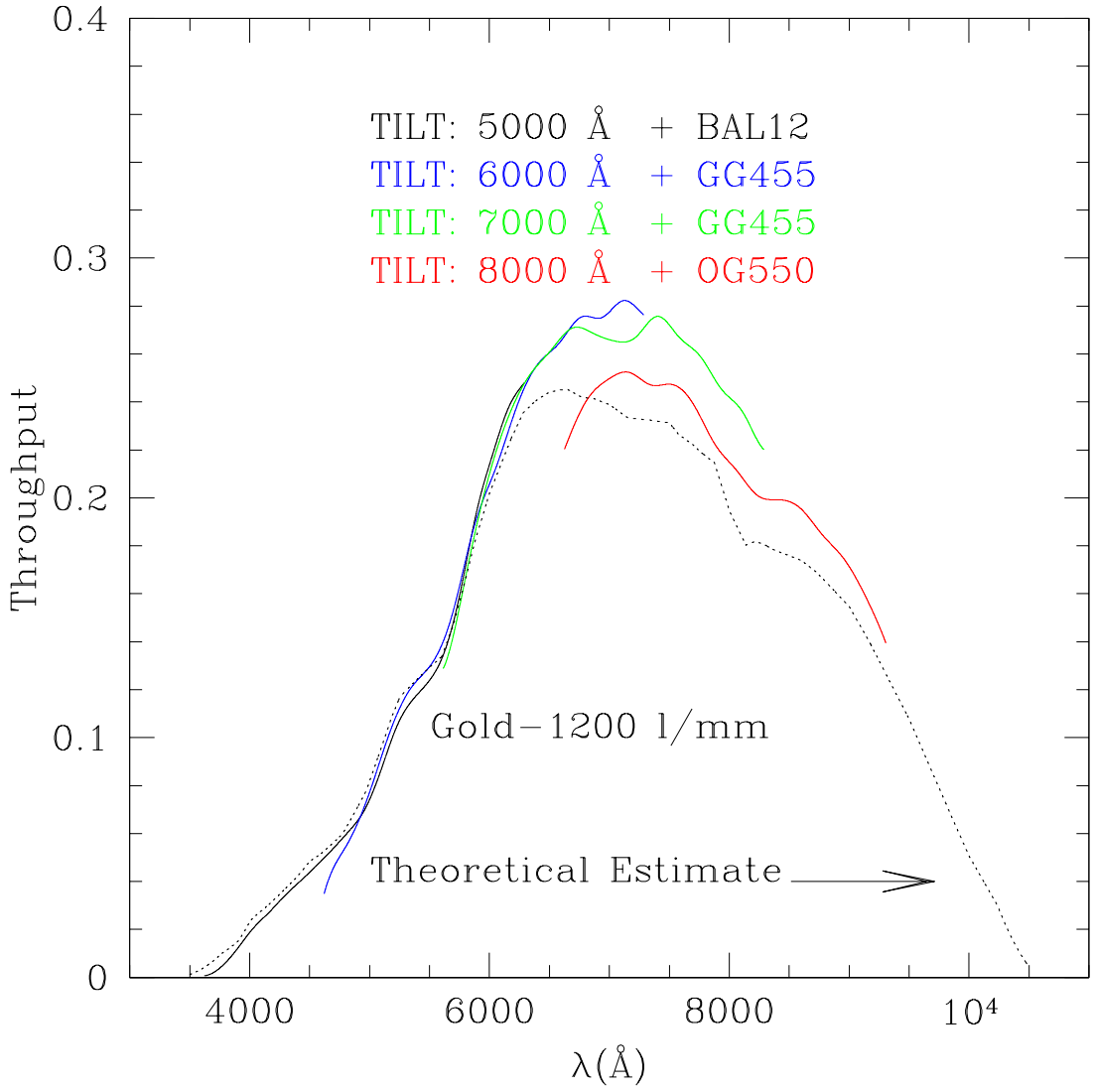

Figure 3.5 Throughput curves of 1200 lines mm^{-1} grating attached to the DEIMOS. The colors indicate filters and blaze wavelengths. This figure is taken from http://www2.keck.hawaii.edu/inst/deimos/ .

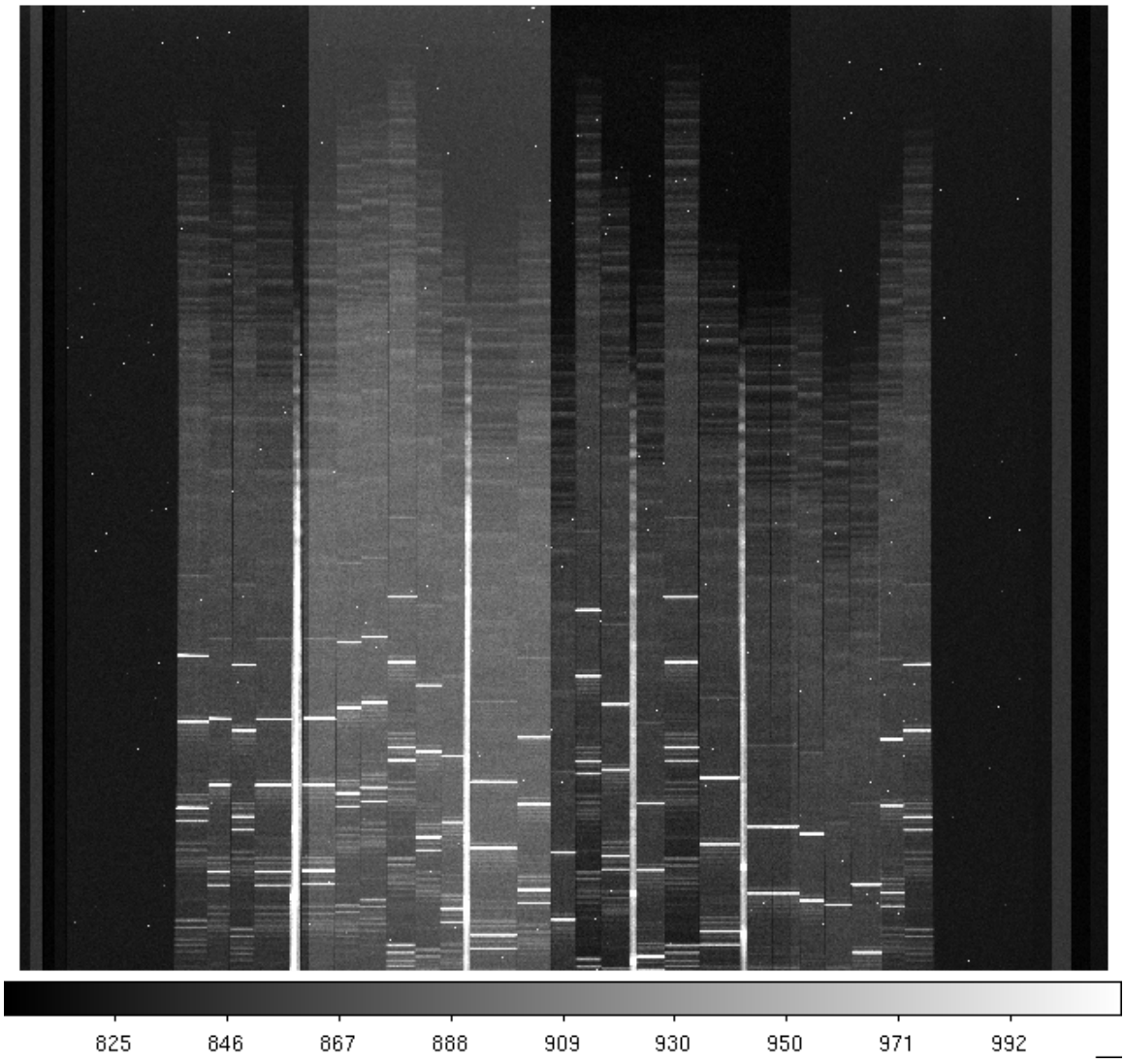

Figure 3.6 Raw LRIS data of a multi-object spectroscopy. The vertical columns along slitlets correspond to the wavelength directions. The white horizontal lines in each spectra shows the sky emission lines.

target-object photo-electron counts $N_{\rm obs}$ and the sky photo-electron counts $N_{\rm sky}$ as

$$N = N_{\rm obs} + N_{\rm sky}. \tag{3.1}$$

On the other hand, the noises of the pixel values σ are described with the readout noises $\sigma_{\rm read}$ and the shot noises of the photo-electrons that come from both objects and the sky. The readout noises follow the Gaussian distribution the width of which are already measured for the instruments ($\sigma_{\rm read} \simeq 4.0$ in the LRIS and $\sigma_{\rm read} \simeq 2.5$ in the DEIMOS detectors), and the shot noises follow the Poisson distribution the average of which is the number of the electrons. Hence, the noises of the pixel values are given by

$$\sigma = \sqrt{N_{\rm obs} + N_{\rm sky} + \sigma^2_{\rm read}}. \tag{3.2}$$

We check that the pixel values counted in the LRIS data follow the equation. The panels (a) and (b) in Figure 3.7 show that the pixel-value distributions of the sky image shown in the left panel of the figure. Because the pixel values are much larger than 1, the Poisson distribution can be approximated with the Gaussian distribution. In Figure 3.7 the pixel-value distributions are well explained by the Gaussian distribution with the width given by Equation (3.2), indicating that the readout noise cannot be ignored in the regions where the sky fluxes are weak. Newman et al. (2013) confirms that the noises in the DEIMOS data can be computed with Equation (3.2).

The raw science data is calibrated for the pixel-to-pixel variations and the wavelength solutions. In the cutout 2D spectra along the slitlets, the sky fluxes are estimated from the area aside objects and extracted from the object spectra. Then, the spectra of the same objects taken in different periods are combined into one composite spectrum with the inverse-variance-weighted mean. The fluxes of the spectra are calibrated with methods based on standard stars and photometry.

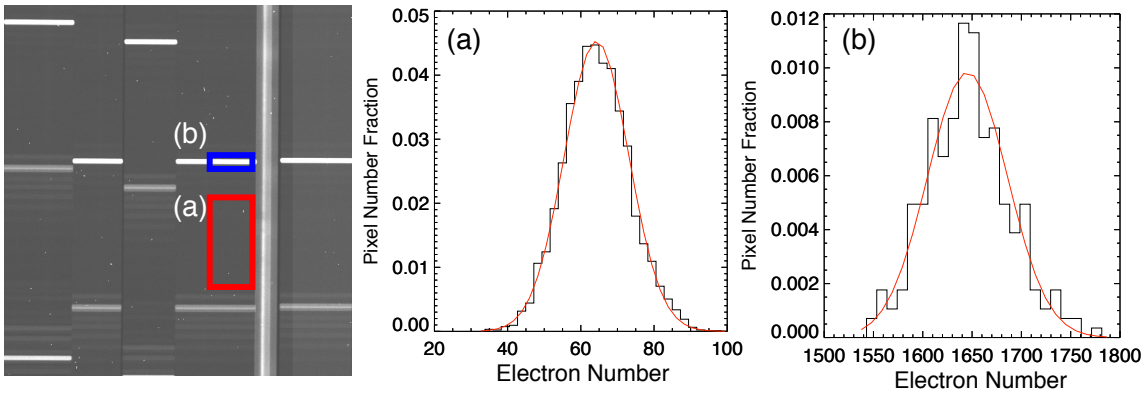

Figure 3.7 Electron counts distributions of region (a) and (b) shown in the left image. The left panel shows the cutout image of Figure 3.6. The area (a) is not significantly affected by the sky emission while the area (b) is. The red lines in the panel (a) and (b) is the best-fit Gaussian curves with the width following Equation (3.2).

CHAPTER 4
SAMPLE SELECTION

This section describes the spectroscopic samples of star-forming galaxies at $z \sim 0$, 1, 2, and 5–6. The spectra are taken with the observed-frame optical instruments (Section 3). We discuss the selection biases among the samples in Section 6.2.3.

4.1 Galaxies at $z \sim 0$

The sample at $z \sim 0$ is drawn from the SDSS Legacy Survey (Section 3.1.2). We select actively star-forming, disk galaxies using their properties. The galaxy properties are mainly taken from the MPA/JHU galaxy catalog[1]. The systemic redshift $z_{\rm sys}$ is derived with a fitting of a linear combination of the galaxy spectral templates to the observed spectra. The spectral templates are constructed from the principal-component analysis. Because these measurements may be affected by blueshifted absorption lines that outflowing gas produces, we compare $z_{\rm sys}$ in the MPA/JHU catalog with redshifts measured by fitting a Gaussian function to Hα emission lines alone. We find that the differences of the two types of redshifts are typically $<$ 5 km s^{-1}, which is negligible. The stellar mass M_* is obtained by fits to the broad-band u, g, r, i, and z photometry with the Bruzual & Charlot (2003) simple stellar population (SSP) models (Kauffmann et al. 2003a; Salim et al. 2007). The SFR within the fiber (SFR$_{\rm fiber}$) is measured from the extinction-corrected Hα emission-line flux, and the total SFR is estimated by applying aperture correction with the photometry inside and outside the fiber (Brinchmann et al. 2004). For our study, the stellar masses and the SFRs are converted from a Kroupa (2001) IMF to a Chabrier (2003) IMF with a correction factor of 0.93. The SFR surface density $\Sigma_{\rm SFR}$ is defined as SFR$_{\rm fiber}/\pi R^2$, where R is the physical distance corresponding to the 1.5″ fiber-aperture radius. The MPA/JHU catalog also includes the emission- and absorption-line fluxes (e.g., Hα, Hβ, [O III], [N II] and $D_n(4000)$; Tremonti et al. 2004) and the photometric properties (e.g., five photometric magnitudes). As a parameter representing a fraction of disk-

[1]The MPA/JHU galaxy catalog is available at http://www.mpa-garching.mpg.de/SDSS/DR7

and elliptical-like morphology of galaxies, we use the fracDeV (Abazajian et al. 2004), which is the best-fit coefficient of a combination of exponential and de Vaucouleurs (1948) rules to the surface brightness of galaxies. When the fracDeVs of galaxies are less/greater than 0.8, we define them as disk/elliptical galaxies. We calculate the inclination i from the r-band axial ratios and absolute magnitudes using Table 8 in Padilla & Strauss (2008). We estimate the halo circular velocity $v_{\rm cir}$ from M_*. First, we convert M_* into the halo mass $M_{\rm h}$ with the stellar-to-halo mass ratio (SHMR) given by Behroozi et al. (2013), who derive the SHMR at $z = 0$–8 with the abundance matching method. Then, $v_{\rm cir}$ are calculated by equations in Mo & White (2002) expressed as

$$v_{\rm cir} = \left(\frac{GM_{\rm h}}{r_{\rm h}}\right)^{1/2}, \tag{4.1}$$

$$r_{\rm h} = \left(\frac{GM_{\rm h}}{100\Omega_{\rm M}H_0^2}\right)^{1/3}(1+z)^{-1}, \tag{4.2}$$

where G is the gravitational constant and $r_{\rm h}$ the halo radius.

We use similar criteria to Chen et al. (2010) to select the star-forming galaxies from the main galaxy sample (Strauss et al. 2002). The redshift range is from $z_{\rm sys} = 0.05$ to 0.18. The criteria to select actively star-forming disk galaxies are $D_n(4000)$ less than 1.5 and r-band fracDeV less than 0.8. AGNs are excluded with the classification by Kauffmann et al. (2003b). We also exclude galaxies whose SFR or stellar mass values are not listed in the MPA/JHU catalog.

In addition to the criteria in Chen et al. (2010), we apply two additional selection criteria for our study. First, we select the galaxies with $\Sigma_{\rm SFR} \geq 10^{-0.8}$ M$_\odot$ yr^{-1} kpc^{-2}, which is above a canonical threshold $\Sigma_{\rm SFR} > 10^{-1}$ M$_\odot$ yr^{-1} kpc^{-2} for local galaxies to launch the outflows (Heckman 2002). Second, we chose face-on galaxies whose inclinations are $i < 30°$ because the typical opening angle of the outflows is $< 60°$ for the SDSS galaxies (Chen et al. 2010). We find 1321 galaxies that satisfy all of the selection criteria.

Finally, we select galaxies to obtain similar stellar mass distributions among redshifts. The blue dashed line in Figure 4.1 indicates the normalized distribution of

the stellar masses of the galaxies. Other cyan and orange solid lines show the distributions at $z \sim 1$ and 2, respectively, which are derived in Section 4.2 and 4.3. To construct samples with similar stellar mass distributions at $z \sim 0$–2, we randomly select the high-mass galaxies at $z \sim 0$ to match the distribution at $z \sim 0$ to that at $z \sim 1$. The final galaxy sample contains 802 galaxies. We refer to the final sample as the $z0$-sample. The normalized distribution of stellar masses for the $z0$-sample is shown in Figure 4.1 with the blue solid line. Figure 4.2 plots the distribution of the $z0$-sample on the SFR–M_* with the blue circles. The median stellar mass of the $z0$-sample is $\log(M_*/M_\odot) = 10.46$.

4.2 Galaxies at $z \sim 1$

We select galaxies at $z \sim 1$ from the DEEP2 DR4 (Newman et al. 2013) [2]. We use galaxy properties taken from the DEEP2 DR4 redshift catalog. The catalog provides the absolute B-band magnitude M_B, $(U-B)$ color in the rest frame, systemic redshift $z_{\rm sys}$, and object classification. The last two parameters are determined by the `spec1d` redshift pipeline. The `spec1d` pipeline minimizes the χ^2 value between the observed spectra and spectral template to find the best-fit $z_{\rm sys}$ value Newman:2013. The error of $z_{\rm sys}$ is ~ 16 km s^{-1}. We also use $(B-V)$ color measured by C. N. A. Willmer (in private communication).

The absorption lines at $z \sim 1$ available for outflow studies are the Mg I λ2852.96 and Mg II $\lambda\lambda$2796.35, 2803.53 absorption lines. These lines fall in the wavelength range of DEEP2 spectra, 6500 to 9100 Å, at $1.2 < z < 1.5$. Although the Fe II $\lambda\lambda$2586.65, 2600.17 lines are useful for outflow studies because they have fine-structure emission lines and therefore less affected by emission filling, the Fe II lines are unfortunately unavailable within the DEEP2 wavelength coverage.

To select galaxies exhibiting the Mg I and Mg II absorption lines in their spectra, we firstly adopt the criteria used in Weiner et al. (2009). They select spectra whose wavelengths are extending to 2788.7 Å in the rest frame. To avoid the AGN/QSO contamination, they exclude the galaxies at $z \geq 1.5$ or classified as AGN in the

[2]The DEEP2 DR4 is available at http://deep.ps.uci.edu/DR4/home.html

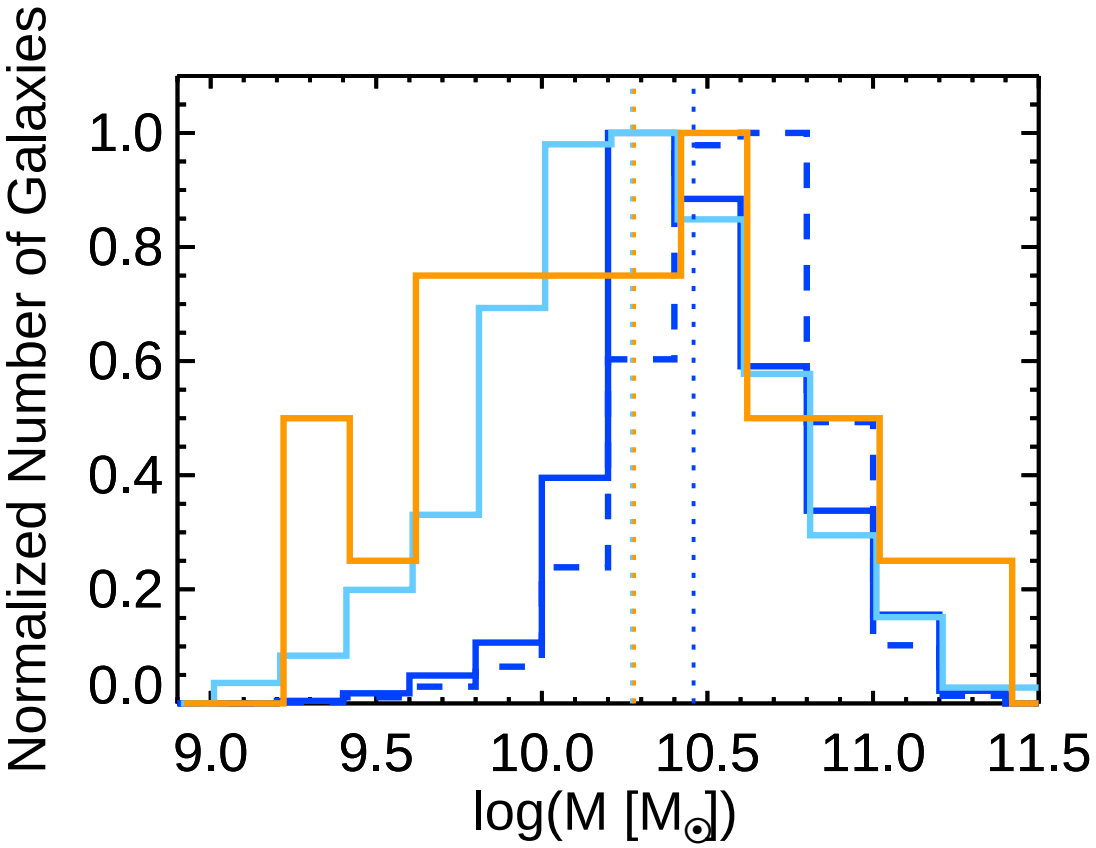

Figure 4.1 Normalized stellar-mass histograms of the samples at $z \sim 0$, 1, and 2. The blue, cyan, and orange solid lines indicate 802 galaxies in the z0-sample, 1337 galaxies in the z1-sample, and 25 galaxies in the z2-sample, respectively. The blue dashed line denotes the SDSS galaxies that satisfy the selection criteria described in Section 4.1. The blue, cyan, and orange vertical dotted lines show the median stellar masses of the z0-, z1-, and z2-samples. The histograms are normalized to the maximum number of the bins.

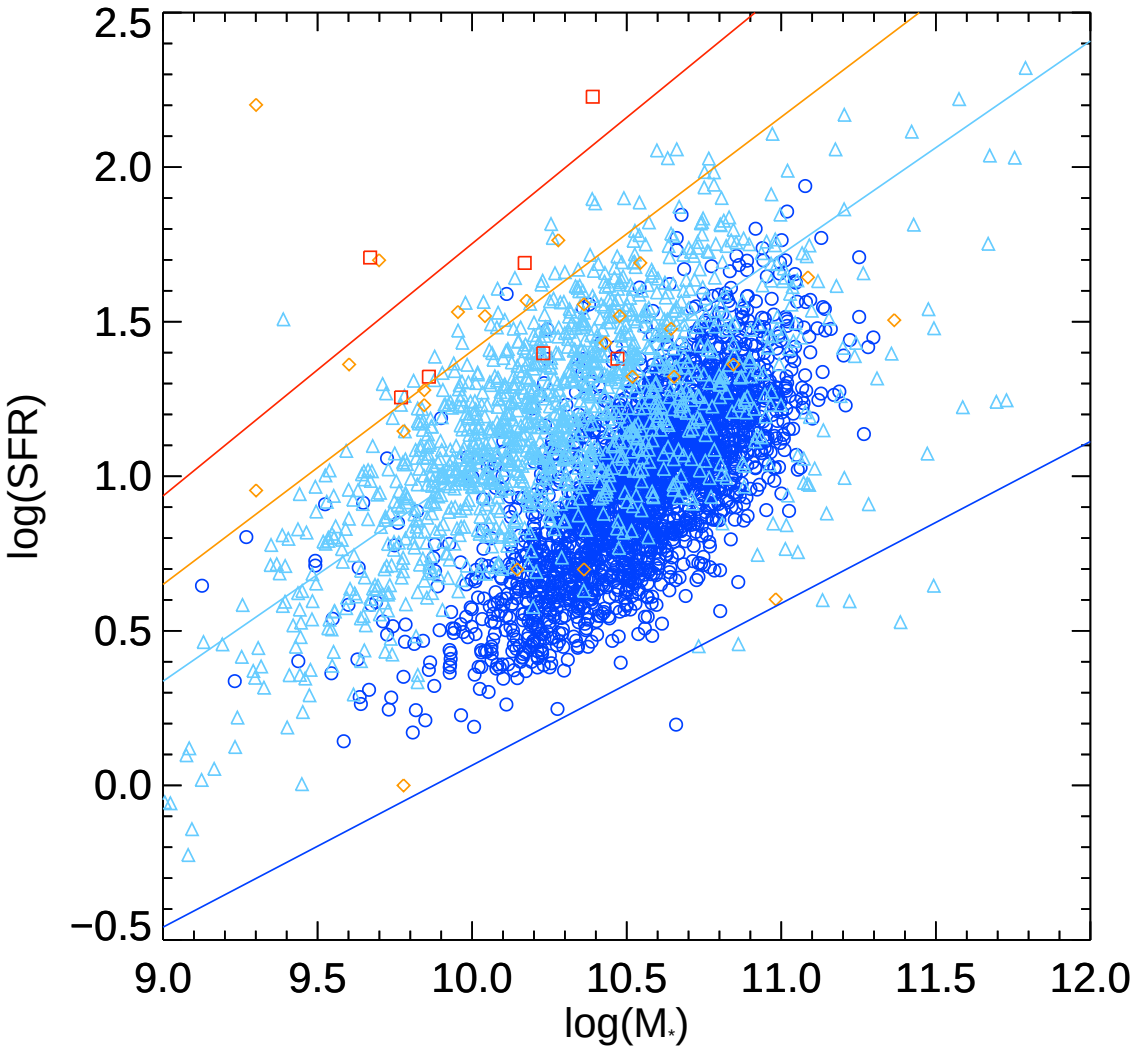

Figure 4.2 SFR as a function of the stellar mass for the samples $z \sim 0$, 1, 2, and 5–6. The blue circles, the cyan triangles, the orange diamonds, and the red squares indicate the galaxies in the $z0$-, $z1$-, $z2$-, and $z6$-samples, respectively. The intrinsic scatter of 0.2 dex (Mostek et al. 2012) is added to SFR of galaxies in the z1-sample for the display purpose. The blue, cyan, orange, and red solid lines are the star-formation main sequences calculated with Equation (28) of Speagle et al. (2014) at $z = 0.1$, 1, 2, and 6, respectively.

object classification (Newman et al. 2013). In addition to these criteria in Weiner et al. (2009), we remove the galaxies that are placed on the red sequence (Willmer et al. 2006; Martin et al. 2012). We also remove the low-S/N galaxies that significantly affect the normalization procedure described below. Our final sample contains 1337 galaxies at $1.2 \lesssim z_{\rm sys} < 1.5$ with the median value of $\langle z \rangle = 1.37$. We refer to this sample as the $z1$-sample.

We compute the stellar mass and SFR of the galaxies in $z1$-sample using equations presented in the literature. The stellar mass is calculated from M_B, $(U-B)$, and $(B-V)$ colors by Equation (1) of Lin et al. (2007). We rewrite the equation from Vega to AB magnitudes using the transformation in Willmer et al. (2006) and Blanton & Roweis (2007):

$$\begin{aligned}\log(M_*/M_\odot) = &-0.4(M_B - 5.48) + 1.737(B-V) \\ &+ 0.309(U-B) - 0.130(U-B)^2 \\ &- 0.268z + 1.123. \end{aligned} \tag{4.3}$$

The normalized distribution of the stellar mass for the $z1$-sample is shown in Figure 4.1 with the cyan line. The median stellar mass is $\log(M_*/M_\odot) = 10.24$. The SFR is calculated from M_B and $(U-B)$. Using Equation (1) and Table 3 in Mostek et al. (2012), we derive the SFR by

$$\begin{aligned}\log \mathrm{SFR} = &0.381 - 0.424(M_B + 21) \\ &- 2.925(U-B) - 2.603(U-B)^2. \end{aligned} \tag{4.4}$$

The SFR value in this equation is calculated with a Salpeter (1955) IMF. We apply a correction factor of 0.62 to obtain the quantities with a Chabrier (2003) IMF. Figure 4.2 plots the distribution of the stellar mass and SFR values of the $z1$-sample with the cyan triangles. We estimate the $v_{\rm cir}$ values using Equation (4.1) and (4.2) with the SMHR at $z \sim 1$.

4.3 Galaxies at $z \sim 2$

We draw the sample from the Erb et al. (2006a) catalog for our sample at $z \sim 2$. As shown in Steidel et al. (2010), this sample contains galaxy–galaxy pairs; the circum-galactic medium around foreground galaxies gives rise to absorption lines in the spectra of the background galaxies. For this reason, we remove 6 background galaxies of the galaxy–galaxy pairs from our sample. Finally, we obtain the spectra of 25 galaxies in the Erb et al. (2006a) catalog. We refer to this sample as the $z2$-sample.

We take $z_{\rm sys}$, the stellar mass, and SFR of the $z2$-sample from Erb et al. (2006a). The systemic redshifts $z_{\rm sys}$ are determined by the Hα emission lines detected in the NIR spectra. The typical rms error of $z_{\rm sys}$ is 60 km s^{-1} (Steidel et al. 2010). The stellar mass and SFR are derived from the spectral energy distribution fitting to the U_n, G, R, J, and K-band magnitudes. The mid-infrared magnitudes taken with Infrared Array Camera on the Spitzer Space Telescope are also used, if they are available. The normalized distribution of the stellar mass for the $z2$-sample is shown in Figure 4.1 with the orange line. The median stellar mass of the $z2$-sample is $\log(M_*/M_\odot) = 10.28$. The M_* and SFR values of $z2$-sample are plotted in Figure 4.2 with the orange squares. We estimate the $v_{\rm cir}$ values from the stellar mass using Equation (4.1) and (4.2) with the SMHR at $z \sim 2$.

4.4 Galaxies at $z = 5$–6

Our sample consists of seven galaxies at $z = 5$–6 listed in Capak et al. (2015). As described in Section 3.2.5, we obtain the rest-frame FUV spectra of seven LBGs in Capak et al. (2015). We refer to this sample as the $z6$-sample.

The ALMA follow-up observations are conducted in a project of #2012.1.00523.S (PI: P. Capak). The Band 7 observations have detected the [C II] 158 μm emission lines in all of the nine LBGs. Previous studies report possible present and past outflow signatures in the [C II] emission lines of these galaxies (Gallerani et al. 2018; Fujimoto et al. 2019). In this study, we use the systemic redshifts measured from the [C II]

emission lines by Capak et al. (2015). In contrast to [O III] 88 μm or optical nebular emission lines that come from only H II regions, the [C II] emission arises from H II regions and photo-dissociated regions, which may results in some uncertainties in the measured redshifts. However, by detecting both [C II] and [O III] emission lines in objects at $z > 6$ with ALMA, recent studies reveal that redshifts determined by [C II] and [O III] are consistent within the errors (Marrone et al. 2018; Decarli et al. 2017; Walter et al. 2018) or show offsets less than 50 km s^{-1} at most (Hashimoto et al. 2019). There is good evidence therefore that measurements of the [C II] emission lines provide reliable systemic redshifts. The median redshift error is $\sim 2 \times 10^{-4}$, corresponding to ~ 10 km s^{-1}. The systemic redshifts of our galaxies are listed in Table 4.1.

We use SFR and M_* derived by Capak et al. (2015). The SFR is estimated from the sum of the rest-frame UV and IR luminosity. The stellar mass is estimated from the spectral energy distribution fitting to the optical to IR photometry taken from the COSMOS photometric redshift catalog (Ilbert et al. 2013) and the Spitzer-Large Area Survey with Hyper-Suprime-Cam (SPLASH; Steinhardt et al. 2014). We estimate the $v_{\rm cir}$ values using Equation (4.1) and (4.2) with the SMHR at $z \sim 6$, although it should be noted that observational constraints are less complete and potentially less robust at $z > 4$ than at $z \lesssim 2$.

Table 4.1 Galaxy properties of seven LBGs

name	R.A.	Decl.	S/N of DEIMOS spectra (pixel^{-1})	$z_{\rm sys}$	$z_{\rm sys}$ error (km s^{-1})	$\log(M_*/M_\odot)$	$\log(SFR)$ ($M_\odot$ yr^{-1})	$\log(M_h/M_\odot)$	$\log(v_{\rm cir})$ (km s^{-1})
HZ1	09:59:53.25	02:07:05.43	0.348115	5.6885	9	10.47 ± 0.13	$1.38^{+0.10}_{-0.06}$	$12.9^{+0.5}_{-0.5}$	$2.8^{+0.2}_{-0.2}$
HZ2	10:02:04.10	01:55:44.05	0.455985	5.6697	30	10.23 ± 0.15	$1.40^{+0.08}_{-0.04}$	$12.0^{+0.5}_{-0.3}$	$2.49^{+0.2}_{-0.08}$
HZ4	09:58:28.52	02:03:06.74	0.616747	5.5440	9	9.67 ± 0.21	$1.71^{+0.31}_{-0.19}$	$11.4^{+0.2}_{-0.1}$	$2.29^{+0.05}_{-0.04}$
HZ6	10:00:21.50	02:35:11.08	0.776667	5.2928	5	10.17 ± 0.15	$1.69^{+0.28}_{-0.12}$	$11.9^{+0.4}_{-0.2}$	$2.45^{+0.1}_{-0.07}$
HZ7	09:59:30.48	02:08:02.81	0.275164	5.2532	20	9.86 ± 0.21	$1.32^{+0.09}_{-0.04}$	$11.6^{+0.2}_{-0.1}$	$2.34^{+0.07}_{-0.05}$
HZ8	10:00:04.06	02:37:35.81	0.216720	5.1533	10	9.77 ± 0.15	$1.26^{+0.11}_{-0.05}$	$11.5^{+0.1}_{-0.1}$	$2.31^{+0.04}_{-0.03}$
HZ10	10:00:59.30	01:33:19.53	0.625486	5.6566	9	10.39 ± 0.17	$2.23^{+0.08}_{-0.08}$	$12.5^{+0.7}_{-0.5}$	$2.7^{+0.2}_{-0.2}$

Note. — The raw DEIMOS spectra are downloaded from KOA (PI: P. Capak). The $z_{\rm sys}$, M_*, and SFR values are drawn from Capak et al. (2015). The $M_{\rm h}$ and $v_{\rm cir}$ values are estimated in Section 4.4. The physical parameters of the composite spectrum are the truncated mean discarding the maximum and minimum values.

[a]The systemic redshift $z_{\rm sys}$ is determined by the [C II] 158 μm emission line taken by ALMA.

CHAPTER 5
ANALYSIS AND MEASUREMENTS

We analyze metal absorption resonance lines in galaxy spectra to study outflow properties. The blueshift of the lines reflects the line-of-sight velocity of the outflowing gas because the outflowing gas gives rise to the blueshifted absorption lines due to the Doppler shift. The absorption lines used for each redshift sample are Na I D $\lambda\lambda$5891.58,5897.56 for the z0-sample; Mg I λ2852.96 and Mg II $\lambda\lambda$2796.35,2803.53 for the z1-sample; Si II λ1260, C II λ1334.53, Si II λ1527, and C IV $\lambda\lambda$1548.20,1550.78 for the z2-sample; and Si II λ1260, C II λ1334.53, Si IV $\lambda\lambda$1394, 1403 for the z6-sample.

We assume that absorption profiles consist of three components: the intrinsic component composed of stellar absorption and nearby nebular emission lines, the systemic component produced by static gas in the ISM of the galaxies, and the outflow component produced by the outflowing gas launched from the galaxies. The stellar atmospheres of cool stars specifically give rise to the strong Na I D absorption, which impacts on the results of the outflow analysis (Chen et al. 2010). The stellar atmospheres moderately affect the absorption profiles of Mg I, Mg II, Si II, C II and C IV (Rubin et al. 2010; Coil et al. 2011; Steidel et al. 2016). The static gas in the ISM produces absorption lines at the systemic velocity while the outflowing gas makes absorption lines blueshifted (e.g., Martin 2005; Chen et al. 2010; Rubin et al. 2014).

In this thesis, we follow Chen et al. (2010) in a large part of our analysis. We explain the three-step procedures of analysis below. First, we create high-S/N composite spectra for the following absorption-line analysis. Second, we determine the stellar continua of the stacked spectra for the intrinsic components of the absorption lines. Third, we model the absorption lines with the stellar continuum and obtain the outflow components. There are some exceptions for the z6-sample in the second and third procedures, due to its relatively low S/N.

5.1 Spectral Stacking

The absorption-line analysis requires high-S/N continuum spectra. Because the individual spectra have S/N low for the absorption-line analysis, we produce high-S/N composites by stacking the individual galaxy spectra.

The $z0$-sample is divided into SFR bins in which S/N pixel^{-1} of the composite spectra reaches 300 at 6000–6050 Å. We scale wavelengths of individual spectra from the observed-frame wavelength $\lambda_{\rm rest}$ to the rest-frame wavelength $\lambda_{\rm obs}$ following $z_{\rm sys}$ by

$$\lambda_{\rm rest} = \lambda_{\rm obs}(1 + z_{\rm sys}). \tag{5.1}$$

The re-sampling process is conducted with the `IDL` procedure `CONBINE1FIBRE`, which is used in the SDSS reduction pipeline. First, the `CONBINE1FIBER` procedure performs the B-spline fitting to an individual spectrum by minimizing the chi-square value between the individual flux density $f_i(\lambda)$ and the B-spline curve $B(\lambda)$:

$$\chi^2_{\text{B-spline}} = \frac{1}{2}\sum_{k=0}^{m}\left(\frac{B(\lambda_k) - f_i(\lambda_k)}{\sigma_i(\lambda_k)}\right)^2 \tag{5.2}$$

$$B(\lambda) = \sum_{j=0}^{n} N_{j,d}(\lambda) Q_j(\lambda_j), \tag{5.3}$$

where $\sigma_i(\lambda)$ is the noise spectrum, $Q_j(\lambda_j)$ the control points, $N_{j,d}(\lambda)$ the B-spline basis function, and d the degree of the curve and $d = 3$ is applied in the procedure. The number of the control points is 1.2 times less than the number of the wavelength bins in the spectra. Then, the procedure re-sample the flux densities in the new rest-frame wavelength bins to be $f'_i(\lambda_k) = B^{\rm best}(\lambda_k)$, where $f'_i(\lambda)$ is the de-redshifted individual spectrum, $f^{\rm best}(\lambda)$ the best-fit curve, λ_k is the wavelengths in the bins of the individual spectrum. The spectral errors are interpolated to match the new wavelengths.

The `CONBINE1FIBRE` procedure construct a re-sampled spectrum well with the cubic B-spline curve, but this interpolation is not statistically strict and does not preserve electron counts. We additionally make re-sampled spectra by putting pixel

values into the nearest bins in the new wavelength bins. If a new wavelength bin includes values from more than one pixels, a new pixel value is calculated with the inverse-variance-weighted mean. Although this re-sampling method reduces the spectral resolution by the bin width, the method keeps the flux density and its error to be values based on the electron counts. The best-fit values and errors obtained in the following sections show 0.02 dex differences in average among spectra produced with the two re-sampling methods, and these difference do not change the conclusions.

We normalize flux densities to the continua at $\lambda_{\rm norm} = 5800$–$5850$ and 5920–5970 Å around Na I D absorption lines to obtain the normalized spectra:

$$f_i^{\rm norm}(\lambda) = \frac{f_i'(\lambda)}{{\rm avg}[f_i'(\lambda_{\rm norm})]}, \tag{5.4}$$

where ${\rm avg}[f_i'(\lambda_{\rm norm})]$ gives the average value of $f_i'(\lambda_{\rm norm})$. The throughput correction does not affects the spectral flux densities. The normalized individual spectra are combined with an inverse-variance weighted mean:

$$F(\lambda) = \frac{\sum_i \frac{1}{\sigma_i^{\rm norm}(\lambda)^2} f_i^{\rm norm}(\lambda)}{\sum_i \frac{1}{\sigma_i^{\rm norm}(\lambda)^2}}, \tag{5.5}$$

$$\frac{1}{\sigma(\lambda)^2} = \sum_i \frac{1}{\sigma_i^{\rm norm}(\lambda)^2} \tag{5.6}$$

where $F(\lambda)$ and $\sigma(\lambda)$is the flux density and the noise of the composite spectrum, respectively, and $\sigma_i(\lambda)$ is the noise spectra of the normalized individual spectra. We exclude bad pixels identified as `OR_MASK` by the SDSS reduction pipeline. We obtain six composite spectra for the $z0$-sample.

The stacking methods for the other samples are the same as $z0$-sample, but for some points. The wavelengths of the spectra in the other sample are converted from air to vacuum with the method in Ciddor (1996). The $z1$-sample is divided into three subsamples in low, medium, and high SFR bins, while the $z2$- and $z6$-samples are not divided into subsamples. The wavelength range used for normalization is $\lambda_{\rm norm} = 2810$–$2840$ Å for $z1$-sample, $\lambda_{\rm norm} = 1410$–$1460$ Å for $z2$-sample,

and $\lambda_{\rm norm}$ = 1300–1350 Å for $z6$-sample. For the $z2$-sample, bad pixels are not excluded since they are not detected by the reduction pipeline. Finally, we obtain three composite spectra for the $z1$-sample, and one composite spectrum for the $z2$- and $z6$-samples, respectively. Figure 5.1 shows stacked spectra of the $z0$-sample, $z1$-sample, and $z2$-sample with the black lines. The top panel of Figure 5.2 shows the composite spectrum and its error spectrum of the $z6$-sample. The continuum S/N of the composite spectrum is 1.4 pixel^{-1} around the Si II λ1260 absorption line. The physical parameters of the composite spectrum are the median values for the $z0$-, $z1$-, and $z2$-samples. Since the size of the $z6$-sample is small, we use the truncated mean discarding the maximum and minimum values. We note that HZ10 in the $z6$-sample has much higher SFR than the other galaxies in the sample. By constructing another composite spectrum without HZ10, we check whether this high-SFR galaxy affects our results to confirm that our conclusion does not change. Properties of the stacked spectra are listed in Table 5.1.

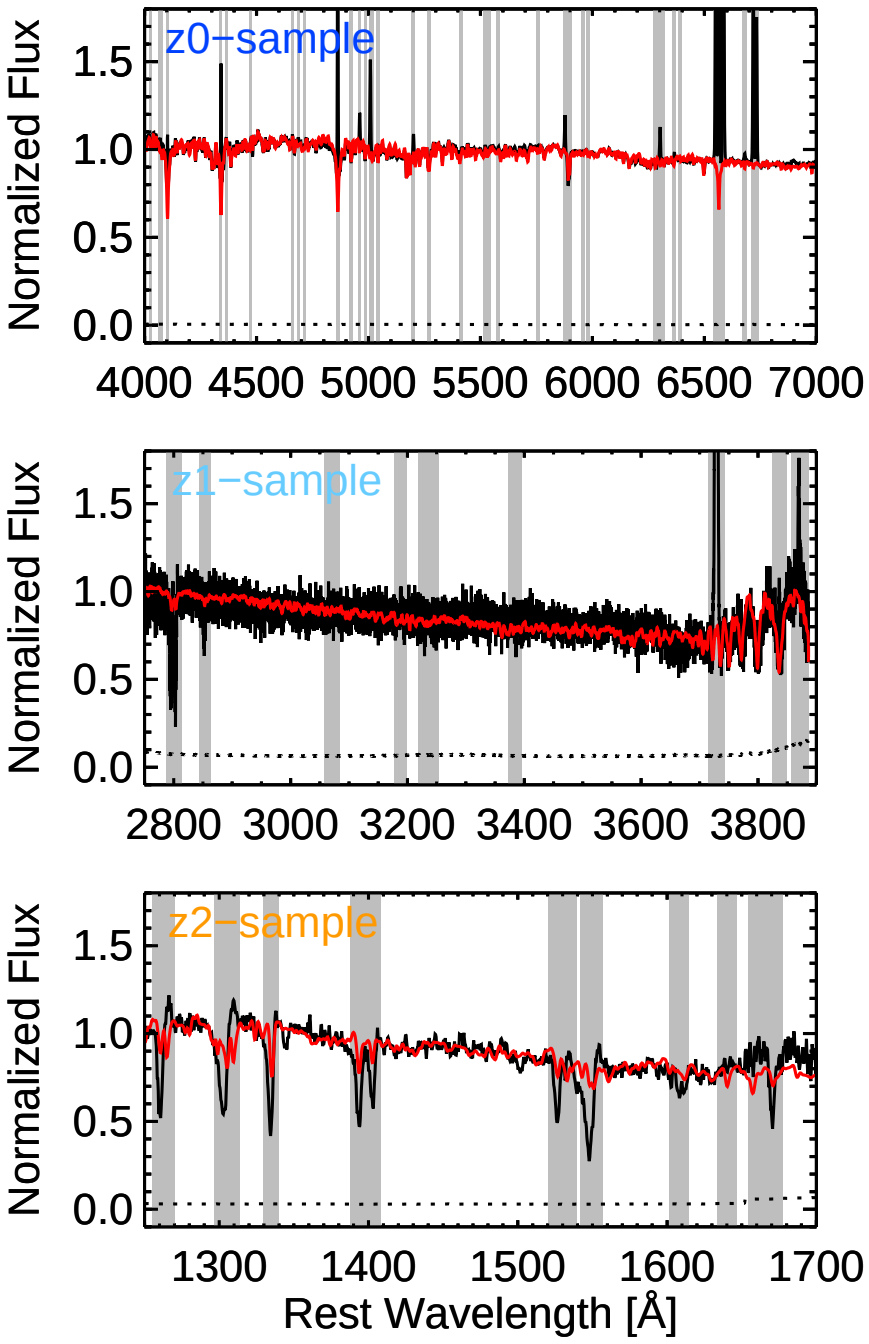

Figure 5.1 Examples of the composite spectra (black) and the best-fit continuum models (red). The spectra of the $z0$-, $z1$-, and $z2$-samples are shown from top to bottom. The panels show the wavelength range used for the stellar continuum fitting. The gray shaded region is not used for the fitting because there exist emission and absorption lines arisen from the ISM. The doted lines denote 1σ uncertainties of the spectra at pixel.

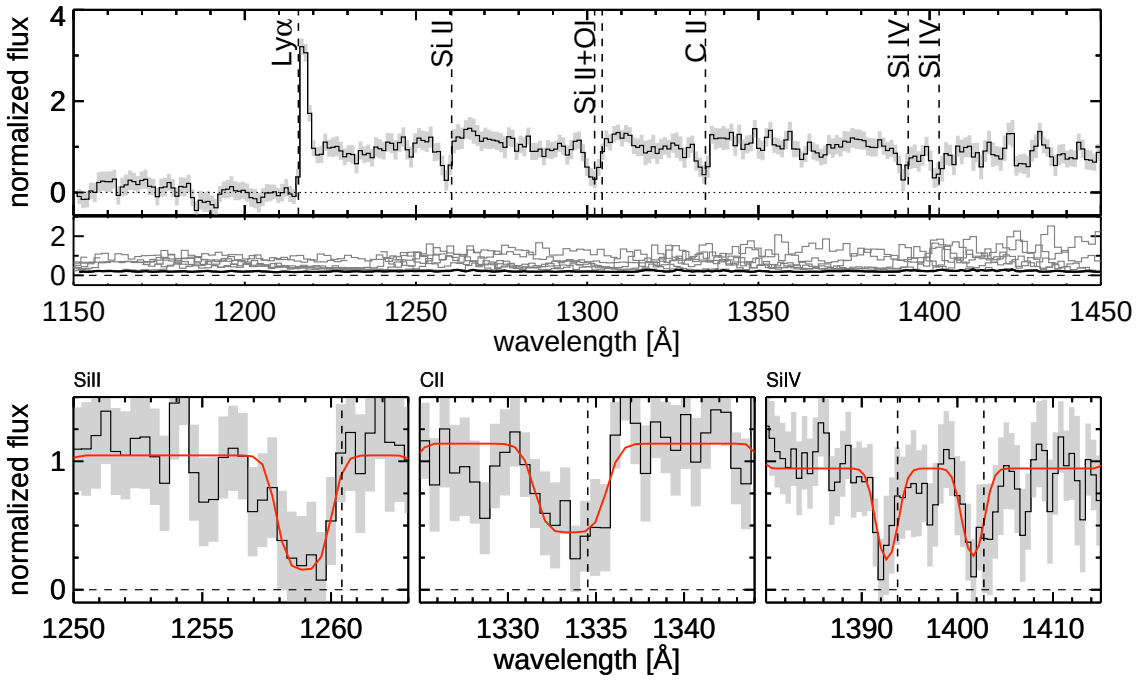

Figure 5.2 Top: composite spectrum of the $z6$-sample. The gray shade indicates the 1σ error at each pixel. The spectral resolution is smoothed for the display purpose. The rest wavelengths of the emission and absorption lines are plotted with the dashed vertical lines. The second panel under the main panel shows the 1σ error spectra. The gray and black lines denote the errors of the normalized individual spectra and the composite spectrum, respectively. The wavelengths of the individual spectra are corrected to the rest frame using the systemic redshift determined by ALMA [C II] observation. Bottom: Si II, C II, and Si IV absorption lines from left to right. The red solid lines are the best-fit absorption model. The vertical and horizontal dashed lines denote the rest wavelengths of the absorption lines and zero flux, respectively.

Table 5.1 Properties of the stacked spectra

sample	line	number	z	logSFR ($M_\odot$ yr^{-1})	$\log M_*$ ($M_\odot$)	$v_{\rm out}$ (km s^{-1})	$v_{\rm max}$ (km s^{-1})	η
z0-sample	Na I D	126	0.064	0.49	10.2	146 ± 5.2	221 ± 18	1.2 ± 0.84
	Na I D	113	0.075	0.69	10.3	152 ± 4.4	261 ± 12	1.2 ± 0.59
	Na I D	109	0.085	0.80	10.4	160 ± 4.5	299 ± 11	1.3 ± 0.53
	Na I D	138	0.11	0.93	10.5	144 ± 4.3	267 ± 11	0.83 ± 0.37
	Na I D	141	0.13	1.1	10.6	153 ± 4.3	327 ± 10	1.0 ± 0.37
	Na I D	123	0.14	1.3	10.8	165 ± 9.7	373 ± 20	1.1 ± 0.49
z1-sample	Mg I	662	1.4	1.0	9.99	220 ± 38	486 ± 64	4.6 ± 3.3
	Mg I	394	1.4	1.3	10.4	164 ± 16	309 ± 91	1.8 ± 3.2
	Mg I	277	1.4	1.5	10.6	175 ± 19	382 ± 98	1.2 ± 2.0
	Mg II	662	1.4	1.0	9.99	207 ± 5.0	445 ± 9	...
	Mg II	394	1.4	1.3	10.4	180 ± 16	442 ± 27	...
	Mg II	277	1.4	1.5	10.6	241 ± 7.1	569 ± 12	...
z2-sample	Si II 1260	25	2.2	1.4	10.3	453 ± 20	708± 20	...
	C II	25	2.2	1.4	10.3	428 ± 20	759± 20	3.6 ± 1.2
	Si II 1527	25	2.2	1.4	10.3	508 ± 32	797± 31	...
	C IV	25	2.2	1.4	10.3	445 ± 16	776± 16	...
z6-sample	Si II 1260	7	5.4	1.5	10.1	366^{+99}_{-63}	690^{+260}_{-120}	...
	C II	7	5.4	1.5	10.1	210^{+74}_{-120}	720^{+140}_{-460}	...
	Si IV	7	5.4	1.5	10.1	220^{+100}_{-150}	610^{+240}_{-96}	...
	Si II +C II	7	5.4	1.5	10.1	...	700^{+180}_{-110}	...

Note. — Columns (3) Number of galaxies used for a composite spectrum. (4) Redshift. (5) Star formation rate. (6) Stellar mass. (7) Central outflow velocity defined in Section 5.4. (8) Maximum outflow velocity defined in Section 5.4. (9) Mass loading factor defined in Section 7.4.

5.2 Stellar Continuum Determination

We determine the stellar continuum with a full spectral fitting of SSP models to the stacked spectra. The SSP models reconstruct spectra of stellar population synthesis, which have parameters of age, metallicity, IMF, and star-formation history, using a stellar spectral library. For the $z0$-sample, we adopt Bruzual & Charlot (2003) SSP models, which have a high spectral resolution in the optical wavelength range of the SDSS spectra. We use the 30 template spectra of instantaneous starbursts with 10 ages of 0.005, 0.025, 0.1, 0.29, 0.64, 0.90, 1.4, 2.5, 5, and 11 Gyr, and three metallicities of $Z = 0.004$, 0.02, and 0.05. For the $z1$- and $z2$-samples, we adopt Maraston et al. (2009) SSP models based on Salpeter IMF because the template spectra of Bruzual & Charlot (2003) models have a low spectral resolution at wavelengths less than 3300 Å. Maraston et al. (2009) models have a high spectral resolution of $R \sim 10000$ in the wavelength range of 1000–4700 Å. We use the 30 template spectra of instantaneous starbursts with 10 ages of 1, 5, 25, 50, 100, 200, 300, 400, 650, and 900 Myr, and three metallicities of $Z = 0.001, 0.01$, and 0.02. The stellar continuum for the $z6$-sample is not derived because the composite spectrum has the low-S/N continuum. In Section 5.3 we evaluate this impact to the results.

For all samples, each template spectrum is convolved with a Gaussian profile representing the stellar velocity dispersion of each stacked spectrum. We construct the best-fit models of the stacked spectra by fitting a linear combination of template spectra with the starburst extinction curve of Calzetti et al. (2000). The fits are conducted with the `IDL` routine `MPFIT`, which performs non-linear least-squares fitting in a robust manner with the Levenberg-Marquardt technique (Markwardt 2009). We use a linear combination of all 30 template spectra for the $z0$-sample, while for the $z1$- and $z2$-sample spectra we use a combination of 10 template spectra of a fixed metallicity, due to low-S/N of the composite spectra. Since our main results are insensitive to differences of metallicity, the metallicity is fixed at $Z = 0.01$ for $z1$- and $z2$-samples. The rest-frame wavelength ranges used for fitting are 4000–7000 Å for the $z0$-sample, 2750–3500 Å for the $z1$-sample, and 1200–1600 Å for the $z2$-sample. In the fitting we omit the wavelength ranges of all of the emission and absorption lines

arisen from the ISM. Figure 5.1 shows the stacked spectra (black) and the best-fit models (red) of the $z0$-, $z1$-, and $z2$-samples.

5.3 Absorption-line Profile Modeling

5.3.1 Blueshifts of absorption lines

If the spectra includes absorption raised by the outflowing gas, absorption lines are expected to be blueshifted. The bottom panels of Figure 5.2 show clear blueshifted absorption lines. To check whether the absorption lines are blueshifted, we fit a Gaussian profile to the absorption lines of the composite spectra divided by the stellar continua in the $z0$-, $z1$-, $z2$-, and $z6$-samples. The free parameters are three: the central velocity, the area, and the width. We confirm that the central velocities of all of the composite spectra are blueshifted with the 5σ significance levels, indicating the existence of the outflow components.

5.3.2 The model of absorption profiles

With the best-fit models of the stellar continuum, we estimate the systemic and outflow components of the absorption lines. The normalized line intensity $I_{\rm obs}(\lambda)$ is assumed to be expressed by three components:

$$I_{\rm obs}(\lambda) = I_{\rm int}(\lambda)\ I_{\rm sys}(\lambda)\ I_{\rm out}(\lambda), \tag{5.7}$$

where $I_{\rm int}(\lambda)$ is the intrinsic component, and $I_{\rm sys}(\lambda)$ and $I_{\rm out}(\lambda)$ are the systemic and the outflow components whose continua are normalized to unity. $I_{\rm int}(\lambda)$ represents the background intensity absorbed by the ISM and outflowing clouds. We use a stellar continuum determined in Section 5.2 for $I_{\rm int}(\lambda)$. Because there is an emission line near the Na I D line, the intrinsic component for the Na I D line is explained later in the case (ii). The line intensity model is convolved with a Gaussian profile representing the stellar velocity dispersion of stacked spectra.

We model the systemic and outflow components with two equations proposed

in Rupke et al. (2005a). In this model, the normalized line intensity $I(\lambda)$ of each component is given by

$$I(\lambda) = 1 - C_{\rm f} + C_{\rm f} e^{-\tau(\lambda)}, \tag{5.8}$$

where $\tau(\lambda)$ is the optical depth, and $C_{\rm f}$ the covering factor. Although $C_{\rm f}$ is a function of the wavelength (Martin & Bouché 2009), we assume that $C_{\rm f}$ is independent of the wavelength. Under the curve-of-growth assumption, the optical depth is written with a Gaussian function as

$$\tau(\lambda) = \tau_0 e^{-(\lambda-\lambda_0)^2/(\lambda_0 b_{\rm D}/c)^2}, \tag{5.9}$$

where c is the speed of light, τ_0 the optical depth at the central wavelength of the line λ_0, and $b_{\rm D}$ the Doppler parameter in units of speed. We describe parameters on the systemic and outflow components with the subscript of "sys" and "out." In Equations (5.8) and (5.9), the normalized intensity $I(\lambda)$ has 4 parameters: λ_0, τ_0, $C_{\rm f}$, and $b_{\rm D}$. The central wavelength $\lambda_{0,\rm sys}$ of the systemic component is fixed at the rest-frame wavelength $\lambda_{\rm rest}$. Hence, the model of $I_{\rm obs}(\lambda)$ includes 7 $(= 4 + 3)$ free parameters in total: $\lambda_{0,\rm out}$, $\tau_{0,\rm out}$, $C_{\rm f,out}$, $b_{\rm D,out}$, $\tau_{0,\rm sys}$, $C_{\rm f,sys}$, and $b_{\rm D,sys}$.

Equations (5.7)–(5.9) are modified in the following three cases. (i) The first case is applied for the doublet lines: Na I D, Mg II, and C IV. We define the optical depth of the blue and red lines of the doublet as $\tau_{\rm B}(\lambda)$ and $\tau_{\rm R}(\lambda)$ whose central wavelengths are $\lambda_{0,\rm B}$ and $\lambda_{0,\rm R}$, respectively. The total optical depth is written as

$$\tau(\lambda) = \tau_{\rm B}(\lambda) + \tau_{\rm R}(\lambda), \tag{5.10}$$

where $\tau_{\rm B}$ and $\tau_{\rm R}$ follow Equation (5.9). Because the blue lines have oscillator strengths twice higher than the red lines for all of the doublet lines, the central optical depths of the blue lines $\tau_{0,\rm B}$ are related to those of the red lines $\tau_{0,\rm R}$ by $\tau_{0,\rm R} = \tau_{0,\rm B}/2$. The ratio of the central wavelengths $\lambda_{0,\rm B}/\lambda_{0,\rm R}$ of the outflow component is fixed to the rest-frame doublet wavelengths ratio. We assume that $b_{\rm D}$ and $C_{\rm f}$ are identical between the blue and red lines because these doublet lines should arise from the same gas clumps. The number of free parameters therefore remains unchanged.

(ii) The second case is applied for Na I D, which has a neighboring emission line

He I λ5877.29. We model the emission line profile $I_{\rm emi}(\lambda)$ of He I using a Gaussian function with additional 2 free parameters. In this case, the intrinsic component of Equation (5.7) is expressed as

$$I_{\rm int}(\lambda) = I_{\rm cont}(\lambda) + I_{\rm emi}(\lambda), \tag{5.11}$$

where $I_{\rm cont}(\lambda)$ is the stellar continuum given in Section 5.2. For Na I D, there are the total of 9 ($= 7+2$) free parameters in $I_{\rm obs}(\lambda)$ that are composed of 7 free parameters of Equations (5.8)–(5.9) and the 2 parameters of the Gaussian function $I_{\rm emi}(\lambda)$.

(iii) The third case is applied for the $z6$-sample. Because the composite spectrum of $z6$-sample exhibits large noises and lower S/N than the other composites, we treat $I_{\rm int}(\lambda)$ as a constant free parameter, $I_{\rm int}(\lambda) = I_0$, instead of normalizing the spectrum by a stellar continuum. In addition, we exclude the systemic component. Therefore, Equation (5.7) becomes

$$I_{\rm obs}(\lambda) = I_0 I_{\rm out}(\lambda). \tag{5.12}$$

The free parameters are five: I_0, v_0, $C_{\rm f}$, τ_0, and $b_{\rm D}$.

We fit an Equation (5.7) profile to the composite spectra $F(\lambda)$ with the `MPFIT` routine by minimizing the chi-square value:

$$\chi^2 = \sum_k \left(\frac{F(\lambda_k) - G \otimes I_{\rm obs}(\lambda_k)}{\sigma(\lambda_k)} \right)^2, \tag{5.13}$$

where $\sigma(\lambda)$ is the noise spectra of the composite spectra and $G \otimes I_{\rm obs}$ expresses the Gaussian convolution of the fitting profile with the instrumental resolution.

We place three constrains of the fitting parameters. First, we constrain the covering fraction to $0 \leq C_{\rm f,out} \leq 0.2$ ($0 \leq C_{\rm f,sys} \leq 1$) for Na I D and Mg I (the other absorption lines), because Martin & Bouché (2009) show that the covering fraction of Na I D and Mg I are smaller than those of Mg II. Second, $b_{\rm D,out}$ of the $z2$-sample is fixed at 130 km s^{-1} that is the average value of the $z1$-sample, while $b_{\rm D,sys}$ of the $z2$-sample is fixed at ≤ 150 km s^{-1}. Third, we place the upper limit of $\tau_{0,\rm out}$ so that the column densities of hydrogen N(H) calculated with Equations (2.33) are as much

as $\log N(\mathrm{H})$ $[\mathrm{cm}^{-2}] \leq 21.5$ (Rupke et al. 2005a; Martin 2006; Rubin et al. 2014).

5.3.3 The best-fit results

Figure 5.4 shows the best-fit results of Na I D for the z0-sample, Mg I and Mg II for the z1-sample, and C II and C IV for the z2-sample. Our procedure provides the reasonable results, detecting the blueshifted outflow components that are shown with the dashed blue lines in the figure. The bottom panels of Figure 5.2 show the best-fit models of the Si II, C II, and Si IV absorption lines with the red lines, demonstrating that the absorption lines are blueshifted. Table A.1 lists the best-fit parameters.

The errors of the best-fit parameters are evaluated with the error matrix and the montecarlo resampling method. In the montecarlo resampling method, we obtain parameter distributions by fitting the line profile to 1000 resampled fluxes based on the spectral noises and use the 50 ± 34th percentile values for their error. In the left panels of Figure 5.3, as a proxy of λ_{out} (Equation 5.14), we compare the v_{out} resampled distributions with the least chi-square values at a fixed v_{out}. The errors measured from the resampling method, shown by the vertical dashed lines, are in good agreement with values at $\chi^2 = \chi^2_{\mathrm{min}} + 1$, where χ^2_{min} is the minimum chi-square value calculated with Equation (5.13). This implies that the errors measured from the resampling method is consistent with 1σ single parameter error. We see that these errors are comparable to the errors estimated from the error matrix.

Figure 5.4 indicates that the best-fit Na I D profile is composed of the large intrinsic and small outflow components. Since the intrinsic component is estimated with the Bruzual & Charlot (2003) SSP model, a different SSP model may systematically affect our results. To evaluate the systematics we analyze the Na I D lines with another SSP model, Maraston & Strömbäck (2011) based on the MILES stellar library (Sánchez-Blázquez et al. 2006). The outflow velocities measured with Maraston & Strömbäck (2011) are very similar to those measured with Bruzual & Charlot (2003); their difference is only 10–30 km s^{-1}. This difference is attributed to the Na ID stellar absorption line of the Maraston & Strömbäck (2011) model shallower than that of the Bruzual & Charlot (2003) model. This result is consistent with the results presented

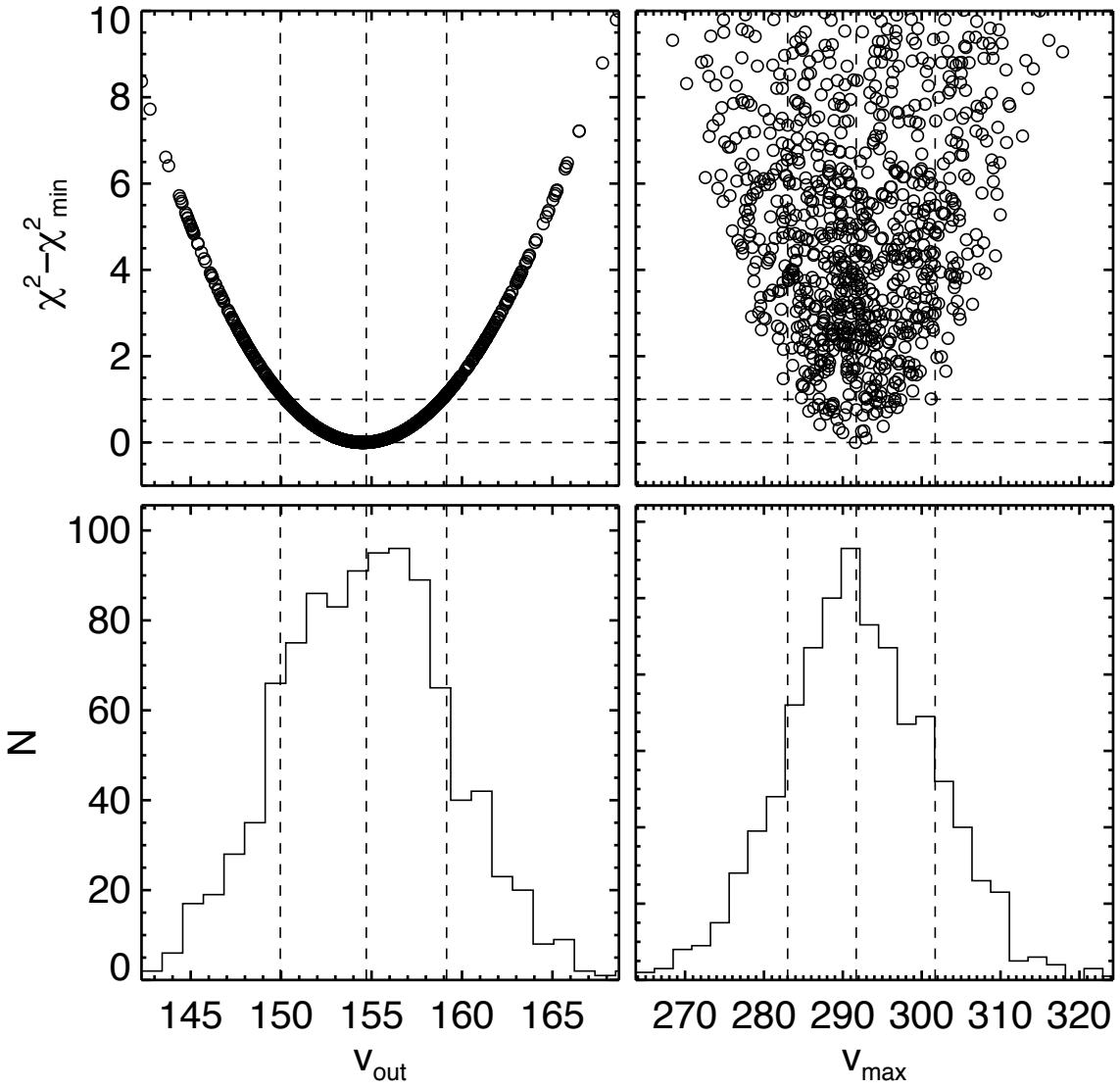

Figure 5.3 Resampled distributions (Bottom) and $\chi^2-\chi^2_{\rm min}$ value (Top) of a composite spectrum of the $z0$-sample. The left and right panels show the distributions of $v_{\rm out}$ and $v_{\rm max}$, respectively. The top left panel shows the minimum $chi^2-\chi^2_{\rm min}$ values at fixed $v_{\rm out}$ values. The top right panel shows the $chi^2-\chi^2_{\rm min}$ values of the resampled distributions. The vertical dashed lines indicate the 50 ± 34th percentile values of the resampled distributions. The horizontal lines in the top panels indicate the values of zero and one. This panels illustrate that the errors measured from the resampling method is consistent with 1σ single parameter error.

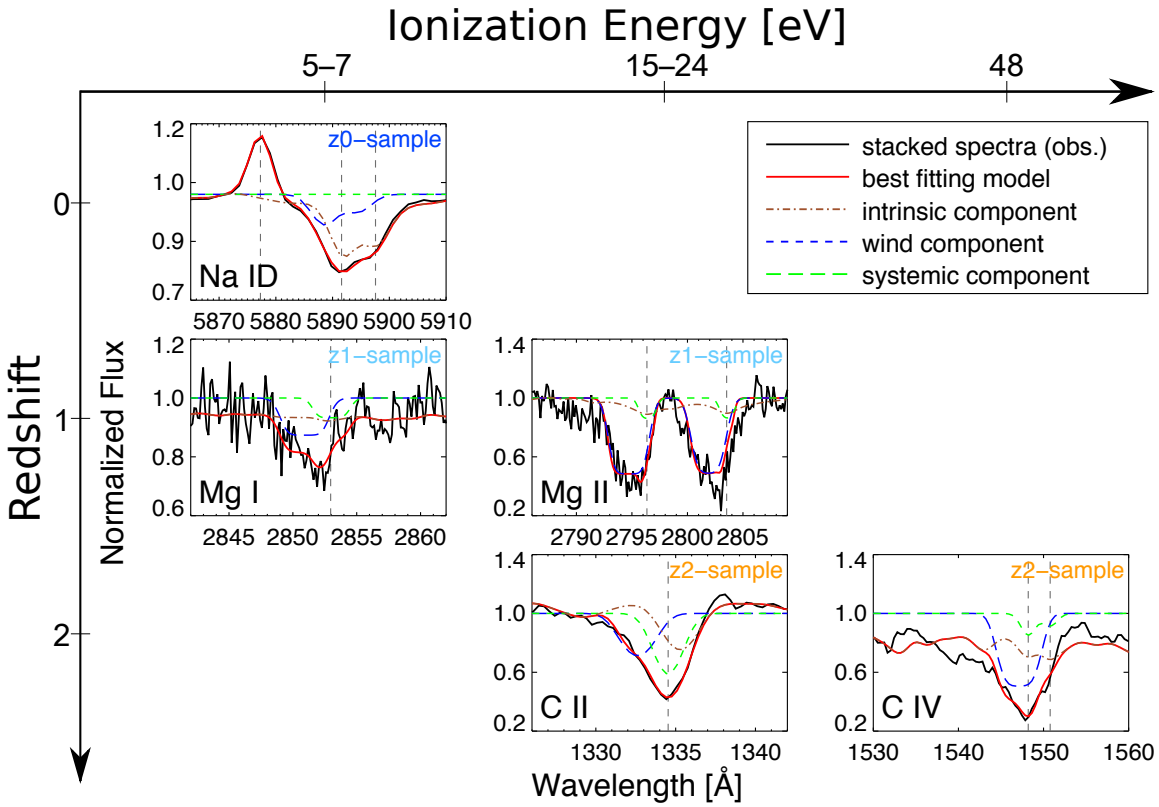

Figure 5.4 Examples of the stacked spectra around the absorption lines (black line). The red lines represent the best-fit models. The dot-dashed brown, dashed blue, and long-dashed green indicate the breakdowns of the lines for the intrinsic, wind, and systemic components, respectively. In this figure, the redshift (the ionization energy) increases from top to bottom (from left to right). The ions of the absorption lines are written at the bottom-left corner of the panels, and the samples are written at the top-right corner. The vertical dashed gray lines denote the rest-frame wavelengths of the absorption lines, except for the line at 5877.29 Å in the top-left panel, which represents the wavelengths of He I emission.

in the appendix in Chen et al. (2010), who evaluate the systematics that different SSP models give[1].

We note that there exists a plausible shallow absorption around 1540 Å in the bottom-right C IV panel in Figure 5.4. Even in the case that the outflow components can be determined by a deep C IV absorption line, the shallow absorption may produce a systematic uncertainty of the outflow velocities. It is possible that this shallow absorption arises from stellar winds of young stars that broaden the C IV absorption line (Schwartz & Martin 2004; Schwartz et al. 2006). Du et al. (2016) reproduce the shallow blueshifted absorption using SSP models from Leitherer et al. (2010) that includes the predicted absorption profiles of the stellar wind. This suggests that the SSP models including the stellar wind effects are preferable for the analysis of the high-ionized absorption lines. Because we do not use the C IV absorption line for discussion, the results of C IV are not relevant to our main scientific results.

Table A.1 shows that three best-fit parameters of the outflow components, $\tau_{0,\mathrm{out}}$, $C_{\mathrm{f,out}}$, and $b_{\mathrm{D,out}}$, reach the edges of the parameter constraints. We evaluate the effects of these constraints on the conclusions. The $\tau_{0,\mathrm{out}}$ fitting range is mainly constrained by the upper limit of the Hydrogen column density. Because the Hydrogen column density larger than this upper limit becomes unreasonably large values in comparison with previous studies (Rupke et al. 2005a; Martin 2006; Rubin et al. 2014), this constraints are appropriate. If we change the $C_{\mathrm{f,out}}$ upper limits for the Na I D absorption lines of the $z0$-sample from 0.2 to 0.3, τ becomes small. The main results in this thesis do not change due to this correlation between $C_{\mathrm{f,out}}$ and τ. The Doppler width $b_{\mathrm{D,out}}$ is limited for the absorption lines of the $z2$-sample. The weak $b_{\mathrm{D,out}}$ constraints are demonstrated in an extreme case in Section 6.1: the one-component fitting that is identical for the $z6$-sample (Equation 5.12). While the outflow central velocity show 0.4 dex offset between the one- and two-component fitting, the results of the maximum outflow velocity are not affected by the differences of the fitting profiles and the $b_{\mathrm{D,out}}$ constraints (see Section 6.1 and Figure 6.4).

[1] As shown in Section 6.2.3, a decrease in outflow velocities at $z \sim 0$ strengthens the redshift evolution of outflow velocities from $z \sim 0$ to 2. Thus systematics given by SSP models do not change our conclusion.

5.4 Outflow Velocity

We measure the velocity of the outflowing gas. Here we define two types of the velocity from the best-fit parameters to the absorption lines: the central outflow velocity $v_{\rm out}$ and the maximum outflow velocity $v_{\rm max}$[2]. The central outflow velocity $v_{\rm out}$ represents the bulk motion of the gas, which is defined with the central wavelength of the outflow component as:

$$v_{\rm out} = \frac{\lambda_{\rm rest} - \lambda_{0,\rm out}}{\lambda_{\rm rest}} c. \tag{5.14}$$

The sign of the $v_{\rm out}$ value is positive when the absorption component is blueshifted. The errors of the $v_{\rm out}$ are converted from the $\lambda_{0,\rm out}$ errors.

The maximum outflow velocity $v_{\rm max}$ reflects the gas motion at large radii of the outflows, based on a simple scenario that the outflowing gas is accelerated towards the outside of the halo (Martin & Bouché 2009; Heckman et al. 2015). Therefore, $v_{\rm max}$ is an indicator of whether the outflowing gas can escape the galactic halo to the IGM. We define the maximum outflow velocity $v_{\rm max}$ to represent the velocity where the best-fit outflow component has a 90% flux from the continuum to the bottom of the thick absorption line, i.e., $I_{\rm out}(\lambda_{\rm max}) = 1 - 0.1 C_{\rm f,out}$, where $\lambda_{\rm max}$ is the wavelength at which the velocity reaches the maximum outflow velocity. Hence, the velocity is given by

$$\begin{aligned} v_{\rm max} = \frac{\lambda_{\rm rest} - \lambda_{\rm max}}{\lambda_{\rm rest}} c &= \frac{\lambda_{\rm rest} - \lambda_{0,\rm out}}{\lambda_{\rm rest}} c + b_{\rm D,out} \sqrt{-\ln\left(\frac{1}{\tau_{0,\rm out}} \ln \frac{1}{0.9}\right)} \\ &= v_{\rm out} + b_{\rm D,out} \sqrt{-\ln\left(\frac{1}{\tau_{0,\rm out}} \ln \frac{1}{0.9}\right)}. \end{aligned} \tag{5.15}$$

The sign of the $v_{\rm max}$ value is defined as positive. The $v_{\rm max}$ errors are evaluated with the 1000 montecarlo resampling and the error propagation using the error matrix. The right panel of Figure 5.3 shows the $v_{\rm max}$ distribution and the chi-square values of the resampling. Although we do not compute the minimum chi-square values

[2]Throughout this thesis, $v_{\rm max}$ is not the maximum circular velocity in the rotation curve of a galaxy or halo, which is often used in theoretical papers.

at fixed $v_{\rm max}$ values, the edge of the chi-square distribution traces the curve of the minimum chi-square values in the figure. The 50 ± 34th percentile values of the $v_{\rm max}$ distribution is consistent with 1σ single parameter error. The errors estimated from the error matrix is comparable to the errors measured with the resampling. We note the effects of the stacking processes on the outflow velocities in Section A.2.

Table A.1 lists the minimum chi-square values and the degree of freedom of the fitting. The chi-square values are acceptable for the Mg I absorption lines of the $z1$-samples and the C II absorption lines of the $z2$-sample, showing that the fitting profiles are appropriate to model the absorption lines. On the other hand, the fits to the Na I D lines of the $z0$-samples and the Mg II lines of the $z1$-samples result in too large chi-square values to be accepted. Figure 5.5 shows the Na I D absorption line (black), the best-fit curve (red), and the residual of them for the composite spectrum with the lowest SFR in the $z0$-sample. The residuals are large at $\lambda > 5890$ Å which is caused by the offset between the spectrum and the best-fit continuum. This is attributed to the strong Na I D stellar-absorption lines in the SSP models reported in previous studies (Chen et al. 2010; Concas et al. 2019). The large residuals at $\lambda > 5890$ Å do not affects the absorption-line fitting because the fitting mainly contribute to reduce χ^2 values at $\lambda < 5890$ Å. Although the χ^2 values at $\lambda < 5890$ Å are even large for all of the $z0$-samples, the best-fit values become acceptable if we make the spectral errors 1.4 times higher by considering a possibility that we have underestimated the errors of the composite spectra. In that case the best-fit errors become 1.4 times larger, but this small change does not affects the conclusions.

To compare the best-fit results derived above with acceptable best-fit results, we perform multi-component fitting to the Mg II absorption lines. The absorption-line components are given by Equations 5.8 and 5.9 with a free parameter of the normalization. First, we mask the spectra with the wavelength range of 2795–2799.5 Å, where the emission filling is strong. For the spectrum with the low SFR in the $z1$-sample, the two-component fitting yields an acceptable values of $\chi^2/{\rm dof} = 148.7/125$. We find that the spectra with the medium and high SFR in the $z1$-sample have extended blue tail of the Mg II lines, which do not exist in the other absorption lines (Figure 5.4). This Mg II blue tail is also seen in the literature for both individual

(Rubin et al. 2014) and composite spectra (Weiner et al. 2009; Zhu et al. 2015). Since the blue tail prevent fair comparisons between the Mg II lines and other absorption lines, we mask the spectra with the wavelength range of 2789–2792 Å. The masked region is illustrated in Figure 5.6. For the spectrum with the medium SFR, we make the spectral errors 1.2 times higher and find that the one-component fitting gives $\chi^2/\mathrm{dof} = 127.3/122$. For the spectrum with the high SFR, the one-component fitting gives $\chi^2/\mathrm{dof} = 138.6/122$. In this analysis, we compute the v_{max} values to be the velocity at which the flux becomes 90% of the continua from the bottom of the best-fit curve. The obtained v_{max} values are $v_{\mathrm{max}} = 495^{+22}_{-17}, 447^{13}_{12}, 533^{+14}_{-14}$ km s^{-1} for the spectra from the low to high SFR, respectively. The low/high SFR spectrum exhibits higher/lower v_{max} values than the values listed in Table 5.1. These differences are small and do not affect the main results in this thesis.

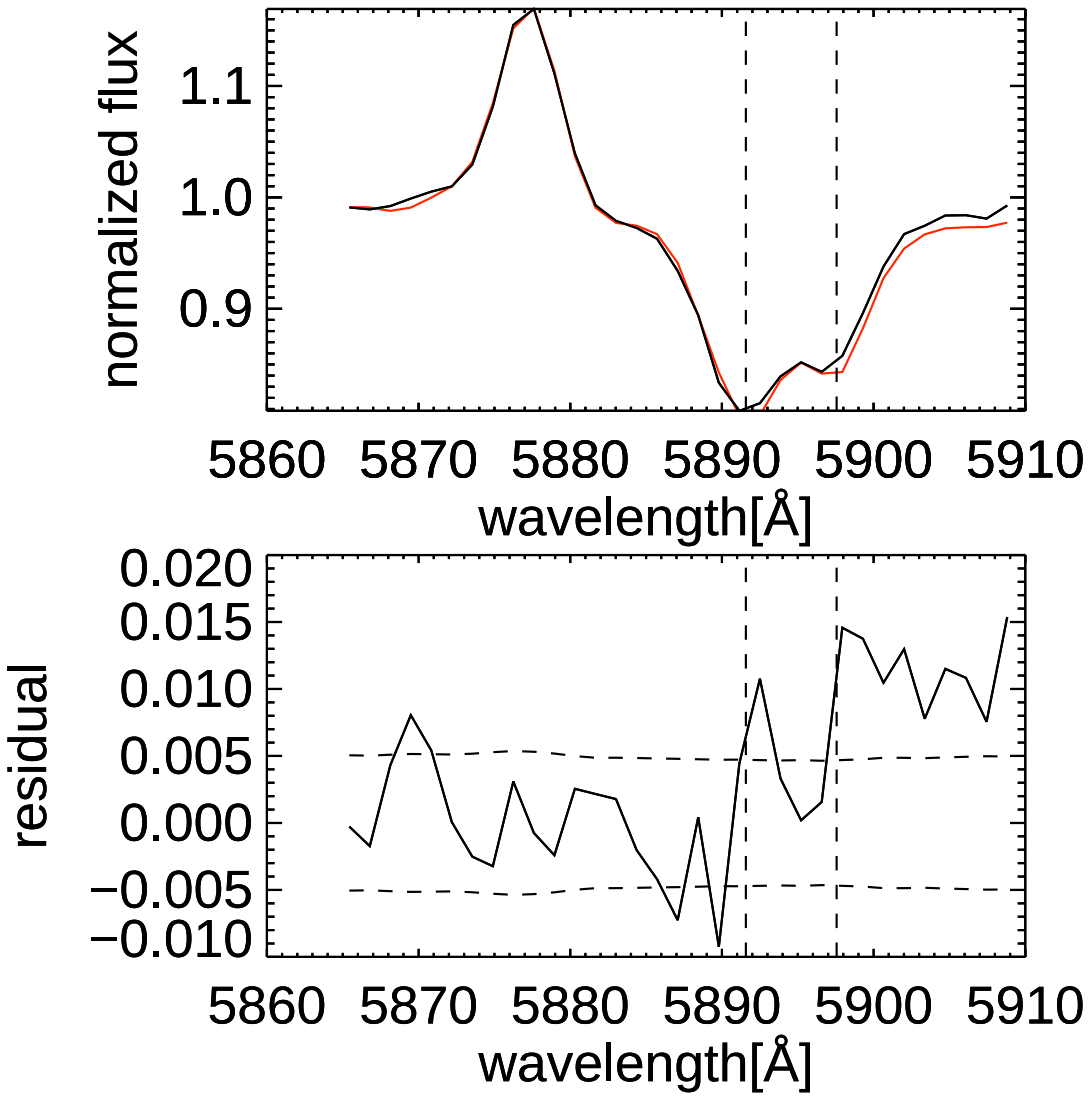

Figure 5.5 (Top) Na I D absorption line of the galaxy with the lowest SFR of the $z0$-sample. The red solid line shows the best-fit curve. The vertical dashed lines indicate the rest-wavelengths of the Na I D doublet. (Bottom) Residuals between the composite spectrum and the best-fit curve. The horizontal dashed lines denote the 1.4 times 1σ error spectrum from zero.

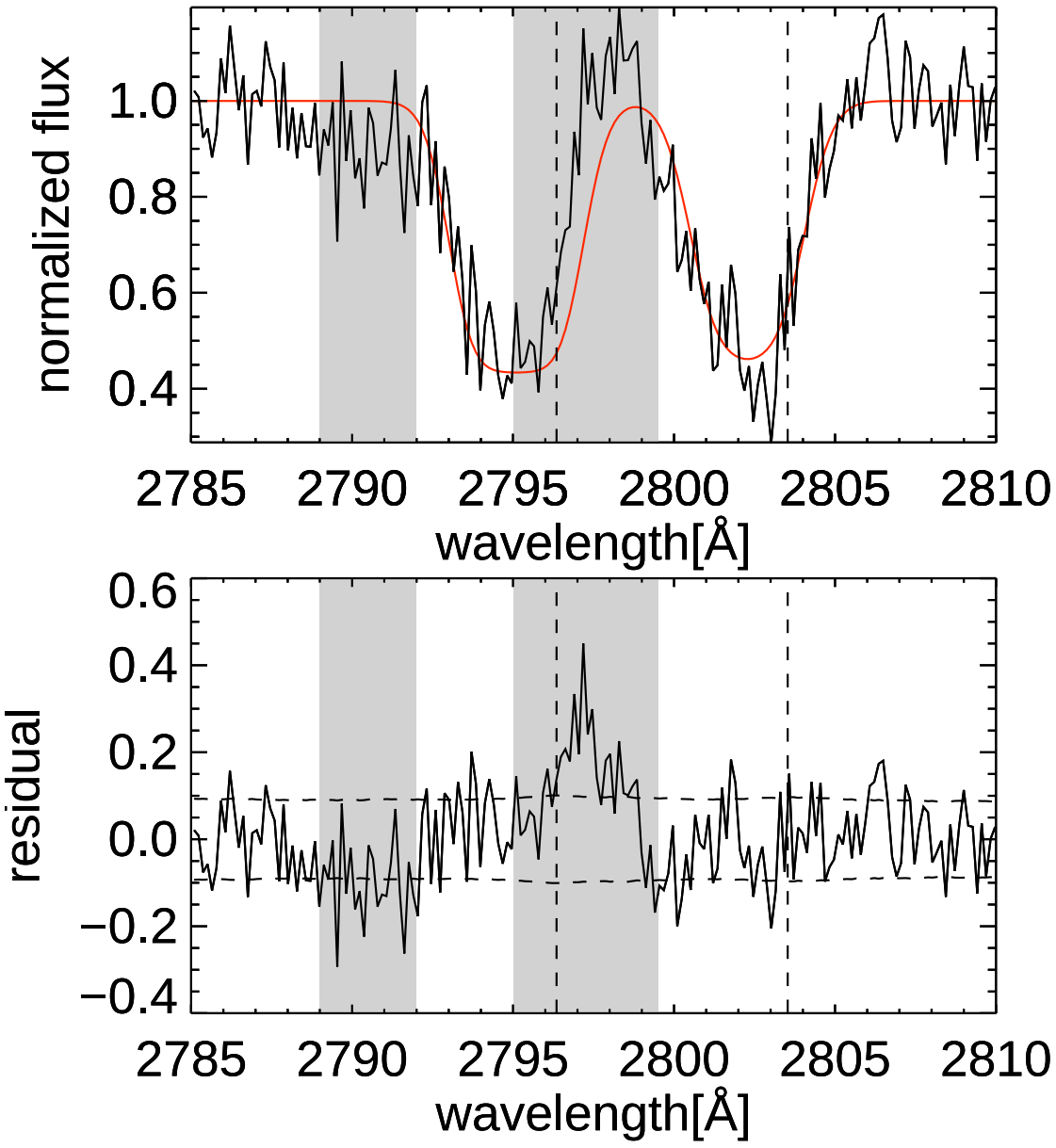

Figure 5.6 (Top) Mg II absorption line of the galaxy with the medium SFR of the $z1$-sample. The red solid line shows the best-fit curve. The vertical dashed lines indicate the rest-wavelengths of the Mg II doublet. The shaded regions are masked for the fitting. (Bottom) Residuals between the composite spectrum and the best-fit curve. The horizontal dashed lines denote the 1.2 times 1σ error spectrum from zero.

CHAPTER 6
RESULTS

6.1 Measurements of Outflow Velocity

Table 5.1 lists the outflow velocities measured from the absorption lines. The best-fit values are $v_{\rm out} \simeq 150$–170 km s^{-1} for the $z0$-sample, $v_{\rm out} \simeq 160$–240 km s^{-1} for the $z1$-sample, $v_{\rm out} \simeq 430$–450 km s^{-1} for the $z2$-sample, and $v_{\rm out} \simeq 210$–370 km s^{-1} for the $z6$-sample. These values are all significantly positive, implying that the absorption lines are blueshifted by the outflows. Figures 6.1–6.3 show $v_{\rm max}$ and $v_{\rm out}$ as a function of SFR for $z0$-, $z1$-, and $z2$-samples, respectively, comparing them to previous work.

Figure 6.1 shows $v_{\rm max}$ and $v_{\rm out}$ of the $z0$-sample with the blue circles. The measured values in this work are as high as those of galaxies at $z \sim 0$ in the literature. We perform a power-law fitting to $v_{\rm max}$ and $v_{\rm out}$ with the form of $\log V = \log V_1 + \alpha \log {\rm SFR}$. The best-fit parameters are $V_1 = 174 \pm 9$ and $\alpha = 0.25 \pm 0.04$ for $V = v_{\rm max}$; and $V_1 = 145 \pm 12$ and $\alpha = 0.03 \pm 0.03$ for $V = v_{\rm out}$. The parameter α for $v_{\rm max}$ is significantly higher than zero, implying that $v_{\rm max}$ depends on SFR. Our measurement of $\alpha = 0.25 \pm 0.04$ for $v_{\rm max}$ is consistent with the results of Martin (2005) and Martin et al. (2012) who claim that $v_{\rm max}$ exhibits a steep slope of $\alpha = 0.35 \pm 0.06$ with SFR. This value is also within a secure range $\alpha = 0.2$–0.3 presented in a review Rupke (2018). On the other hand, the parameter α for $v_{\rm out}$ suggests no relation with SFR, which agrees with Chen et al. (2010), Martin et al. (2012), and Rubin et al. (2014), who use similar techniques to measure the central outflow velocity.

Figure 6.2 compares $v_{\rm max}$ and $v_{\rm out}$ of the $z1$-sample with those of galaxies at $z \sim 1$ in the literature. The measurements in this work are in good agreement with the previous measurements. Particularly, the $v_{\rm max}$ values are consistent with those in Weiner et al. (2009), who measure the outflow velocities using the DEEP2 DR3 spectra. We find a weak positive scaling relation between $v_{\rm out}$ and SFR. In the literature, whereas $v_{\rm out}$ of individual galaxies show no correlation (Kornei et al. 2012; Martin et al. 2012; Rubin et al. 2014), those of stacked galaxies show a positive correlation (Weiner et al. 2009; Bordoloi et al. 2014). The positive scaling relation in

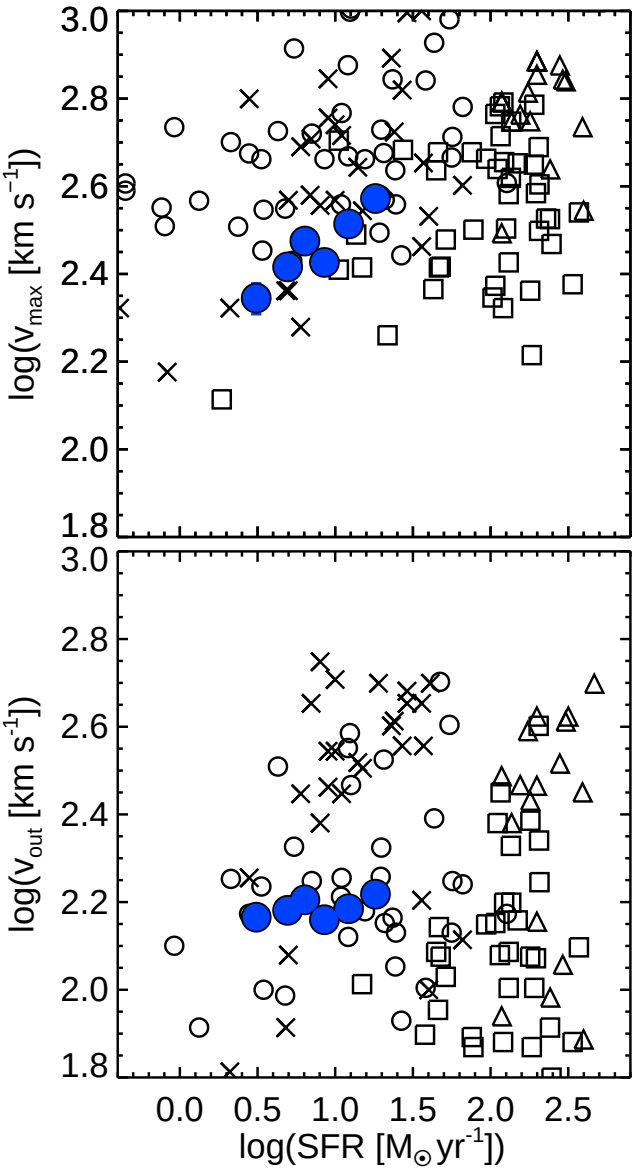

Figure 6.1 Outflow velocities at $z \sim 0$. Top: Maximum outflow velocity (blue filled circle) of the $z0$-sample as a function of SFR. Error bars denote the 1σ fitting error, although the bars are smaller than the point size. The open symbols show the maximum outflow velocities of local galaxies in the literature: Heckman et al. (2015, cross), Martin (2005, triangle), Rupke et al. (2005b, square), and Chisholm et al. (2015, circle). Bottom: Central outflow velocity of the $z0$-sample. The symbols are the same as those in the top panel of this figure.

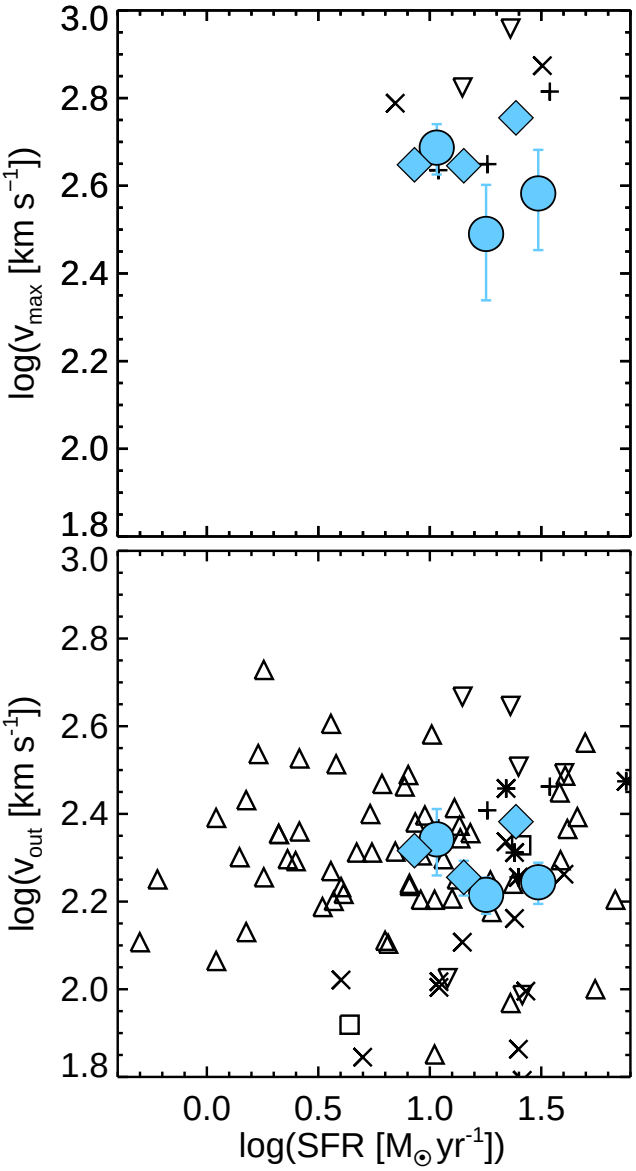

Figure 6.2 Same as Figure 6.1, but for the outflow velocities at $z \sim 1$. Top: Maximum outflow velocity of the $z1$-sample for Mg I and Mg II (cyan filled circle and diamond, respectively) as a function of SFRs.. Error bars denote the 1σ fitting errors. The open symbols show the maximum outflow velocities of galaxies at $z \sim 0.5$–1 in the literature: Kornei et al. (2012, cross), Rubin et al. (2014, triangle), Bordoloi et al. (2014, square), Weiner et al. (2009, plus), Martin et al. (2012, upside-down triangle), and Du et al. (2016, asterisk). Bottom: Central outflow velocity of the $z1$-sample. The symbols are the same as those in the top panel of this figure. In both panels, the cyan diamonds are offset in SFR by 0.1 dex for clarity.

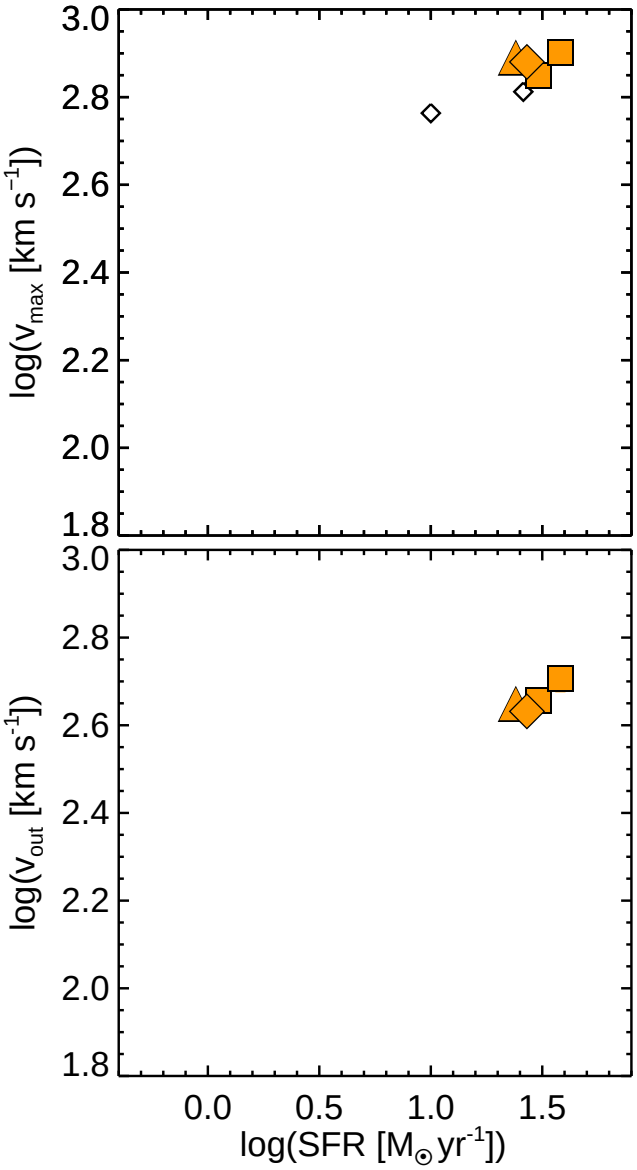

Figure 6.3 Same as Figure 6.1, but for the outflow velocities at $z \sim 2$. The orange diamond, triangle, and squares indicate the central outflow velocities of the $z2$-sample for C II, C IV, and Si II respectively. Error bars denote the 1σ fitting errors. The open diamonds show the maximum outflow velocities of galaxies in Erb et al. (2012). The orange triangle and squares are offset in SFR for clarity.

Figure 6.2 is consistent with the previous results on the stacked galaxies.

Figure 6.3 shows the outflow velocities estimated with the C II, Si II λ1260, Si II λ1527, and C IV lines of the $z2$-sample. Low-ionized elements (Si II and C II) have ionization potentials lower than that of hydrogen (13.6 eV), while high-ionized elements (C IV) have a much higher ionization potential. Despite the different elements and ionization energy, these outflow velocities exhibit comparable values. Unlike the C II and C IV lines, the Si II λ1260 and λ1527 lines have their associated Si II* λ1265 and λ1533 fine-structure emission lines, respectively. Therefore, emission filling in the Si II absorption lines is predicted to be weaker than that of the C II and C IV lines. The measurement results indicate that this difference of the lines do not change the outflow velocities in our analysis. In the remainder of this thesis, we use the C II line to estimate outflow parameters of the $z2$-sample and refer to Si II λ1260 as Si II.

Figure 6.3 compares the $z2$-sample and the literature at $z \sim 2$. Steidel et al. (2010) statistically study the outflow velocities ($\Delta v_{\rm IS}$) of the UV-selected galaxies at $z \sim 2$ with the sample drawn from Erb et al. (2006a), which is the identical catalog that we use in this work. They compute the mean outflow velocity of $\langle \Delta v_{\rm IS} \rangle = -164 \pm 16$ km s^{-1}, which is lower than $v_{\rm out}$ of the $z2$-sample (orange symbols). This arises from different methods to measure the velocities: the outflow velocity measured with the one-component fitting become lower than those with the two-component fitting. We confirm this by fitting Equation (5.12) to the C II absorption line of the $z2$-sample. The measured $v_{\rm out}$ value is 175 ± 12 km s^{-1}, which is consistent with $\Delta v_{\rm IS}$. Therefore, it is quantitatively reasonable that $\Delta v_{\rm IS}$ is lower than $v_{\rm out}$, even though both are subsamples drawn from Erb et al. (2006a). Steidel et al. (2010) also find that the scaling relation of central outflow velocities at $z \gtrsim 2$ is flatter than that at $z < 2$, but we can not mention the scaling relation of the $z2$-sample due to its small sample size.

The best-fit $v_{\rm out}$ values of the $z6$-sample are consistent with the values estimated in the literature that analyzes the data of the same galaxies (Pavesi et al. 2016; Gallerani et al. 2018). HZ10 has the Si II, Si II λ1304/O I, and Si IV absorption lines blueshifted by 100 ± 180 km s^{-1} with respect to the [C II] emission line (Pavesi et al. 2016). The composite emission of the [C II] line in HZ1–9, without HZ5, is reported

to have the broad wings that are possibly generated by the outflows with the velocity of $\sigma = 220$–500 km s^{-1} (Gallerani et al. 2018).

The derived maximum outflow velocities for Si II, C II, and Si IV of the $z6$-sample are $v_{\rm max}^{\rm SiII} = 690^{+260}_{-120}$ km s^{-1}, $v_{\rm max}^{\rm CII} = 720^{+140}_{-460}$ km s^{-1}, and $v_{\rm max}^{\rm SiIV} = 610^{+240}_{-96}$ km s^{-1}, respectively. Although the low- and high-ionized elements trace the different state of the ISM, $v_{\rm max}^{\rm SiII}$ and $v_{\rm max}^{\rm CII}$ are consistent with $v_{\rm max}^{\rm SiIV}$ within the 1σ errors. This consistency agrees with the results of the $z2$-sample and previous work on outflows at $z \sim 0$ (Chisholm et al. 2016b). To estimate effects of the different fitting profile for the $z6$-sample (Equation 5.12), and to compare the velocities at $z \sim 6$ with ones at lower redshifts, we re-analyze the normalized composite spectrum of the $z2$-sample to measure the maximum outflow velocity with the one-component absorption-line profile. We find that the new $v_{\rm max}$ value is 60 km s^{-1}lower than the $v_{\rm max}$ value measured with the two-component fitting. This systematics do not affect our conclusions.

Si II and C II have similar ionization potentials and oscillator strengths, and exhibit similar maximum outflow velocities. To obtain a typical $v_{\rm max}$ value of the $z = 5$–6 galaxies, we additionally measure the maximum outflow velocity by a simultaneous fitting to Si II and C II, adopting $v_{\rm max}$ as a free parameter instead of $\lambda_{0,\rm out}$, using Equation (5.15). Both lines are assumed to have the same C_f. The measured value is $v_{\rm max} = 700^{+180}_{-110}$ km s^{-1}, which is consistent with $v_{\rm max}^{\rm SiII}$ and $v_{\rm max}^{\rm CII}$, but its error is smaller than those of $v_{\rm max}^{\rm SiII}$ and $v_{\rm max}^{\rm CII}$. Table 5.1 lists the measurements of $v_{\rm max}$ and $v_{\rm out}$ for each absorption lines. These are the first measurements of the $v_{\rm max}$ values at $z = 5$–6 with the absorption lines. The $v_{\rm max}$ values are consistent with the results of the [C II] emission analysis by Gallerani et al. (2018). They stack the ALMA [C II] emission lines of HZ1–9, without HZ5, to present an possible outflow signature with a broad [C II] component of a highest velocity of ~ 500–700 km s^{-1}, although this broad flux excess may include emission from satellites around the central galaxies.

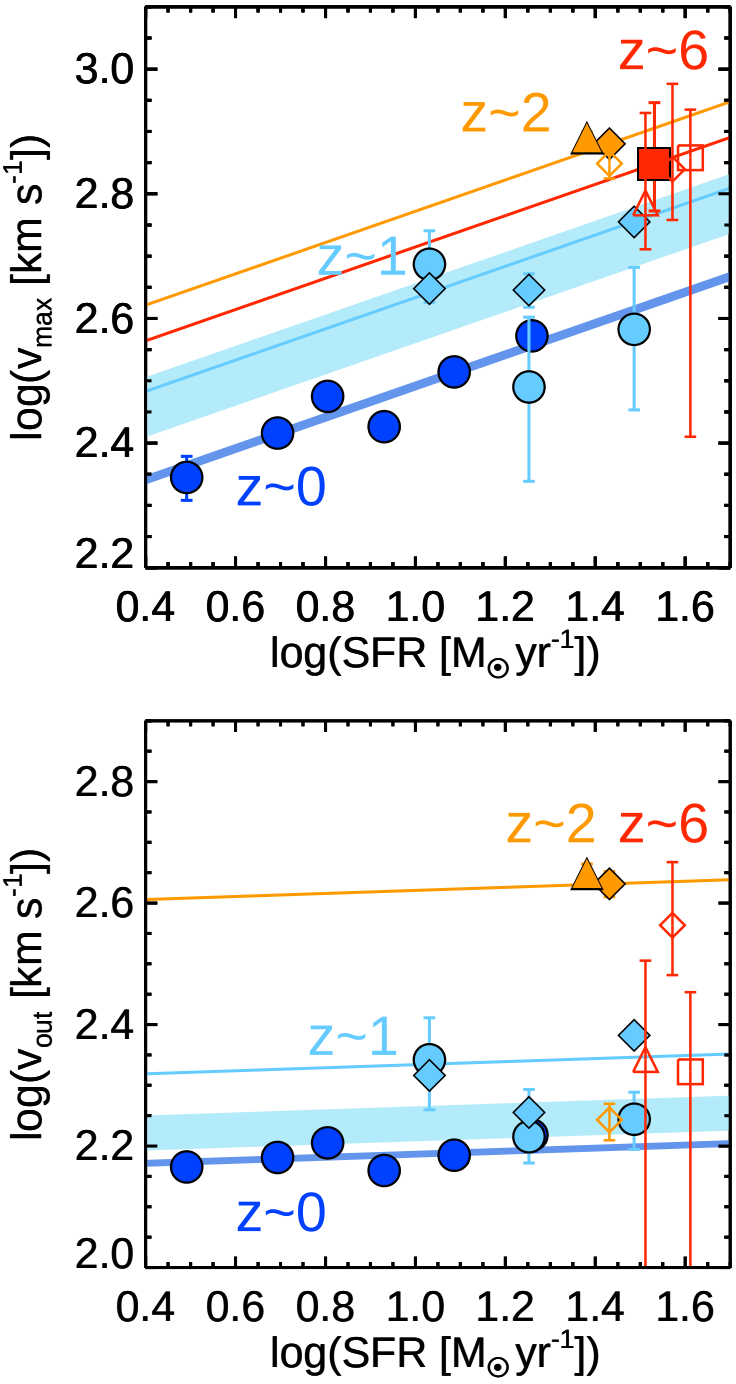

Figure 6.4 (Next page)

6.2 Outflow Velocities vs. Galaxy Properties at $z = 0$–6

6.2.1 Velocities as a function of SFR

We show the $v_{\rm max}$ and $v_{\rm out}$ measurements of the $z0$-, $z1$-, $z2$-, and $z6$-samples as a function of SFR with the blue, cyan, orange, and red symbols, respectively, in Figure 6.4. For a comparison with the $z6$-sample, the figure also shows the velocities of the $z2$-sample measured by fits of only the outflow component (Equation 5.12), with the orange open diamonds. The figure suggests an increasing trend of the outflow velocity from $v_{\rm max} \simeq 200$–400 km s^{-1} at $z \sim 0$ to $v_{\rm max} \simeq 700$ km s^{-1} at $z \sim 6$ in the similar stellar mass range. However, Martin & Bouché (2009) and Chisholm et al. (2016b) demonstrate that the outflow velocity depends on the depths of the absorption lines whereas Tanner et al. (2016) show that the outflow velocity depends on ionization energy of the ions used for velocity measurements. For these reasons, we compare the outflow velocities of the absorption lines that have similar depths and ionization energy, as shown in Figure 5.4. We describe the details of our comparisons below.

First, we compare the $z0$-sample with the $z1$-sample. We use the velocities computed from the Na I D and Mg I absorption lines, respectively, which are depicted with

Figure 6.4 Outflow velocities as a function of SFR of the $z0$- (blue symbol), $z1$- (cyan symbol), $z2$- (orange symbol), and $z6$-samples (red symbol). Top: Maximum outflow velocity as a function of SFR. Each symbol corresponds to the metal absorption lines used for the measure: Na I D (blue circle), Mg I (cyan circle), Mg II (cyan diamond), C II (orange diamond), C IV (orange triangle), and Si II +C II (red square). The circles, diamonds and squares, and triangle indicate the low (5–7 eV), medium (15–24 eV), and high (48 eV) ionization energy, respectively. The red open symbols show the measurements with C II (diamond), Si II (square), and Si IV (triangle). The orange open diamond indicates the velocity with C II measured with a fit of only the outflow component. Error bars denote the 1σ fitting errors. The blue and cyan shades show the best-fit lines for Na I D and Mg I, respectively, with 1σ fitting error range. The cyan line denotes the best-fit line for Mg II and the orange and red lines pass through the measurements with C II and Si II +C II, respectively, with the same slope. Bottom: Central outflow velocity as a function of SFRs. The symbols are the same as those in the top panel of this figure. In both panels, the orange triangles and open symbols are offset in SFR for clarity.

the circles in Figure 6.4. The ionization energies of Na I D, $\simeq$ 5.1 eV, is similar to that of Mg I, $\simeq$ 7.6 eV. In Section 6.1, we obtain the best-fit parameters of the scaling relation $\log V = \log V_1 + \alpha \mathrm{SFR}$ for Na I D of the $z0$-sample: $V_1 = 174 \pm 9$ (145 ± 12) and $\alpha = 0.25 \pm 0.04$ (0.03 ± 0.03) for $V = v_{\rm max}$ $(v_{\rm out})$. We assume that the scaling slope α exhibits no evolution along the redshift. Therefore, to compare the velocities at a fixed SFR, we fit the scaling relation to $v_{\rm max}$ $(v_{\rm out})$ for Na I D and Mg I, with slopes fixed at $\alpha = 0.25$ (0.03). The best-fit parameter sets are $V_1 = 174 \pm 2$ (145 ± 2) and $V_1 = 227 \pm 27$ (163 ± 11) for Na I D and Mg I, respectively. The blue and cyan shades in Figure 6.4 illustrate the best-fit relations of Na I D at $z \sim 0$ and Mg I at $z \sim 1$, respectively. The widths of the shades represent the 1σ fitting error ranges. Figure 6.4 indicates that $v_{\rm max}$ $(v_{\rm out})$ at $z \sim 1$ is significantly higher than that at $z \sim 0$.

Second, to compare the $z1$- with $z2$-samples, we use the velocities computed from Mg II and C II absorption lines, respectively. The measurements are depicted with the diamonds in Figure 6.4. The ionization energies of Mg II and C II are $\simeq$ 15 eV and $\simeq$ 24 eV, respectively. In the same manner as Mg I of the $z1$-sample, we fit the scaling relation to $v_{\rm max}$ $(v_{\rm out})$ of Mg II with a slope fixed at $\alpha = 0.25$ (0.03). We obtain the best-fit parameters of $V_1 = 241 \pm 4$ (251 ± 3) for $V = v_{\rm max}$ $(v_{\rm out})$. The cyan lines in Figure 6.4 illustrates the best-fit relations of Mg II at $z \sim 1$. For comparison, the orange lines show the lines with $\alpha = 0.25$ (0.03) through the orange diamonds. Figure 6.4 suggests that $v_{\rm max}$ $(v_{\rm out})$ at $z \sim 2$ is significantly higher than the one at $z \sim 1$.

We note that there is a large $v_{\rm out}$ difference between Mg II and C II. It is possible that the large systemic component in the C II line (Figure 5.4) generate the high $v_{\rm out}$ measurement of C II. Figure 6.4 demonstrates that fitting only the outflow component to the C II line (orange open diamond) results on the $v_{\rm out}$ value comparable to Mg II. The $z6$-sample, which only the outflow component is fitted to, also exhibit similar $v_{\rm out}$ values with the red open symbols. In addition, to evaluate outflow velocities with a small systemic component, we fit the C II line with $C_{\rm f,sys} = 0.1$, which is the median of the best-fit $C_{\rm f,sys}$ values at $z \sim$ 0–1, and without the constraints on $b_{\rm D,out}$. The best-fit $v_{\rm out}$ value drops to $\simeq 208 \pm 30$ km s^{-1}, which is consistent with the velocity of Mg II. On the other hand, the best-fit $v_{\rm max}$ ($\simeq 719 \pm 39$ km s^{-1}) is consistent with the values estimated without a constraint to $C_{\rm f,sys}$. Thus, the $v_{\rm max}$ value is not affected

by $C_{\rm f,sys}$ and our conclusions do not change. We think that the results of $v_{\rm out}$ are sensitive to the systemic component.

Finally, in Figure 6.4, the $v_{\rm max}^{\rm SiII}$, $v_{\rm max}^{\rm CII}$, $v_{\rm max}^{\rm SiIV}$, and $v_{\rm max}$ values are plotted with the open orange square, diamond, triangle, and filled red square, respectively. We find that the $v_{\rm max}$ value at $z = 5$–6 is ~ 0.2 dex higher than the relation at $z \sim 0$ and comparable to the value at $z \sim 2$, although the SFR values at $z \sim 0$ are not as high as those at $z = 5$–6.

In summary, we find that the outflow velocity shows a strong increase from $z \sim 0$ to 2 and a slight or no increase from $z \sim 2$ to 6 in galaxies with similar M_* and SFR. Although there is some implication of the redshift evolution of the outflow velocities (Du et al. 2016; Rupke et al. 2005b), this is the first time to identify the clear trend of the redshift evolution of the outflow velocities in the wide redshift range.

6.2.2 Velocities as a function of $v_{\rm cir}$

Figure 6.5 illustrates $v_{\rm max}$ as a function of $v_{\rm cir}$ that are calculated from M_* with the SHMR given by Behroozi et al. (2013) and Equations (4.1) and (4.2). The data points are located in different $v_{\rm cir}$ ranges depending on the redshifts, because the galaxies at $z = 0$–6 have similar stellar mass M_* and halo mass $M_{\rm h}$ values, but the halo size $r_{\rm h}$ decreases with decreasing redshift (Equation 4.2). In the figure, $v_{\rm max}$ tightly correlates with $v_{\rm cir}$ at $z \sim 0$. A correlation with a similar slope at $z \sim 0$ is also seen in the cyan diamonds at $z \sim 1$. Although only one measurement is available at $z \sim 2$ and $z = 5$–6, the two data points at $z \sim 2$–6 appear to follow the relation at $z \sim 0$–1. Therefore, Figure 6.5 suggests a single relation between $v_{\rm max}$ and $v_{\rm cir}$ that holds over $z \sim 0$–6. The dotted line indicates a relation at $z = 0$ obtained from observations by the Cosmic Origin Spectrograph mounted on the Hubble Space Telescope (Heckman & Borthakur 2016), which has a similar slope to our measurements. The offset between our data points and the dotted line may arise from different method to measure the maximum outflow velocity and the fact that our data points represent the average properties of galaxies at each redshift while their extreme-starburst galaxies have much higher SFR than our galaxies.

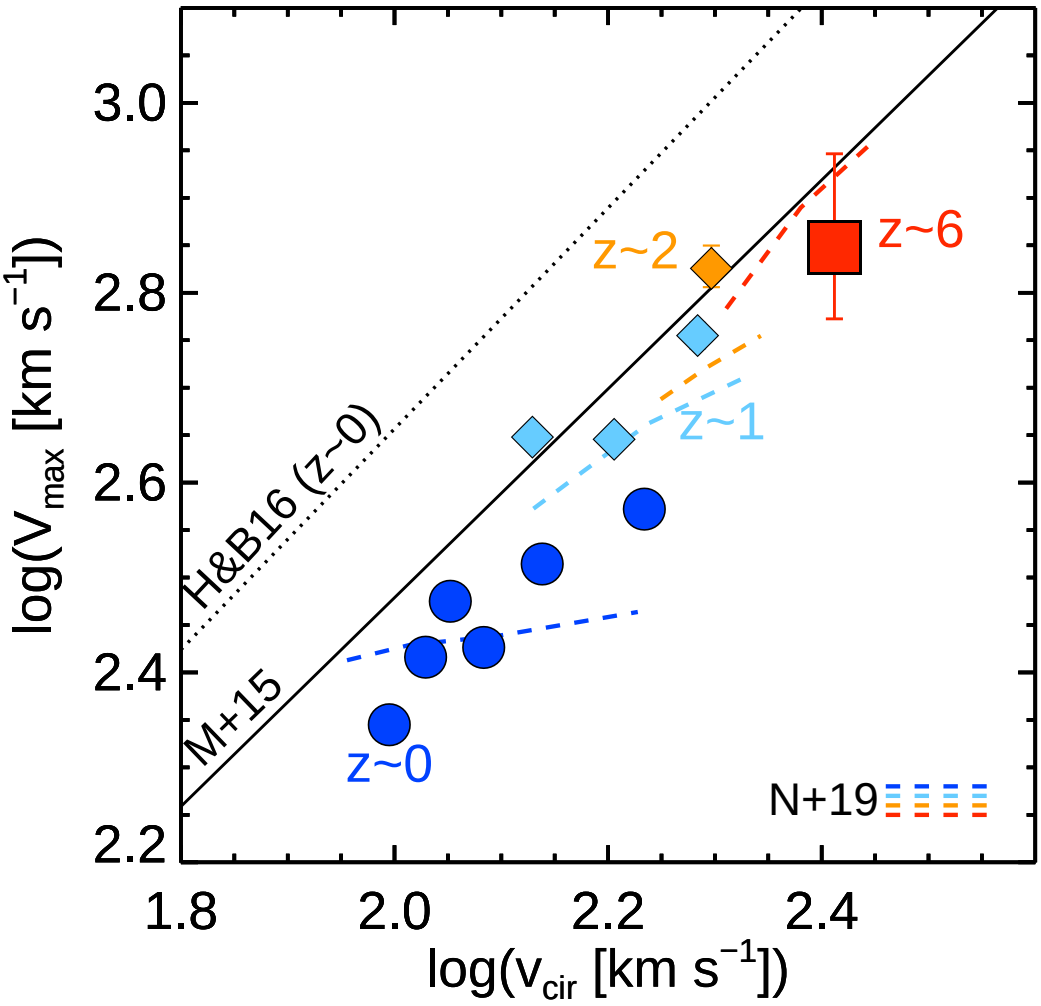

Figure 6.5 $v_{\rm max}$ as a function of the circular velocity $v_{\rm cir}$ that are converted from the stellar mass. The symbols are the same as in Figure 6.4. The solid black line and colored dashed lines represent a theoretical relation at $z = 0.5$–4 predicted by the FIRE simulations (the flux-weighted average 90th percentile velocity; Muratov et al. 2015) and relations at $z = 0$ (blue), 1 (cyan), 2 (orange), and 6 (red) predicted by the IllustrisTNG simulation (90th percentile velocity; Nelson et al. 2019), respectively. The dotted line indicates a relation of extreme-starburst galaxies $z \sim 0$ Heckman & Borthakur (2016).

6.2.3 Selection biases

This section describes the effects of the selection biases. There are three sources of possible systematics in our analysis. The first is the selection criterion of the SFR surface density $\Sigma_{\rm SFR}$ for the $z0$-sample. In Section 4.1, we select the galaxies with a criterion of $\Sigma_{\rm SFR}$ larger than $10^{-0.8}$ $M_\odot$ yr^{-1} kpc^{-2}. We do not apply this criterion for the other samples, but galaxies at $z > 0$ are likely to satisfy it. A large fraction of the $z1$-sample meets the $\Sigma_{\rm SFR}$ criterion because the galaxies in the $z1$-sample exhibit the median SFR of ~ 7 $M_\odot$ yr^{-1} and the median Petrosian radius of 5.2 kpc which is estimated from photometry of a part of galaxies taken with Hubble Space Telescope/Advanced Camera for Surveys (Weiner et al. 2009). All of the $z2$-sample also meet the criterion of $\Sigma_{\rm SFR}$ (Erb et al. 2006a). The galaxy size of the $z6$-sample is unavailable, but their high SFR and high redshift suggest the SFR surface density high enough to meet the criterion Shibuya et al. (2015). Therefore, this criterion is likely to be satisfied by the $z1$-, $z2$-, and $z6$-samples.

The second is the selection criterion of the inclination i for the $z0$-sample. We select the galaxies with $i < 30°$, which is much less than $60°$ that is the typical outflow opening angle of the SDSS galaxies (Chen et al. 2010). Although it is difficult to estimate i from image of high-z galaxies, it is reported that the outflows of the galaxies at $z \sim 1$–2 is more spherical than those at $z \sim 0$ (Weiner et al. 2009; Martin et al. 2012; Rubin et al. 2014). In addition, the galaxies under these criteria of $\Sigma_{\rm SFR}$ and i should decrease the outflow velocities of the $z0$-sample, indicating the redshift evolution of the outflow velocities more clearly.

The third is the differences of instrumental resolutions. It is possible that low spectral resolutions may systematically increase the values of $v_{\rm max}$. We convolve the highest resolution ($R \sim 5000$) spectra of the $z1$-sample with SDSS ($R \sim 2000$) and LRIS ($R \sim 800$) spectral resolutions and compare the $v_{\rm max}$ values of the original and the convolved spectra. We confirm that the systematics of the different spectral resolution is negligible in our results.

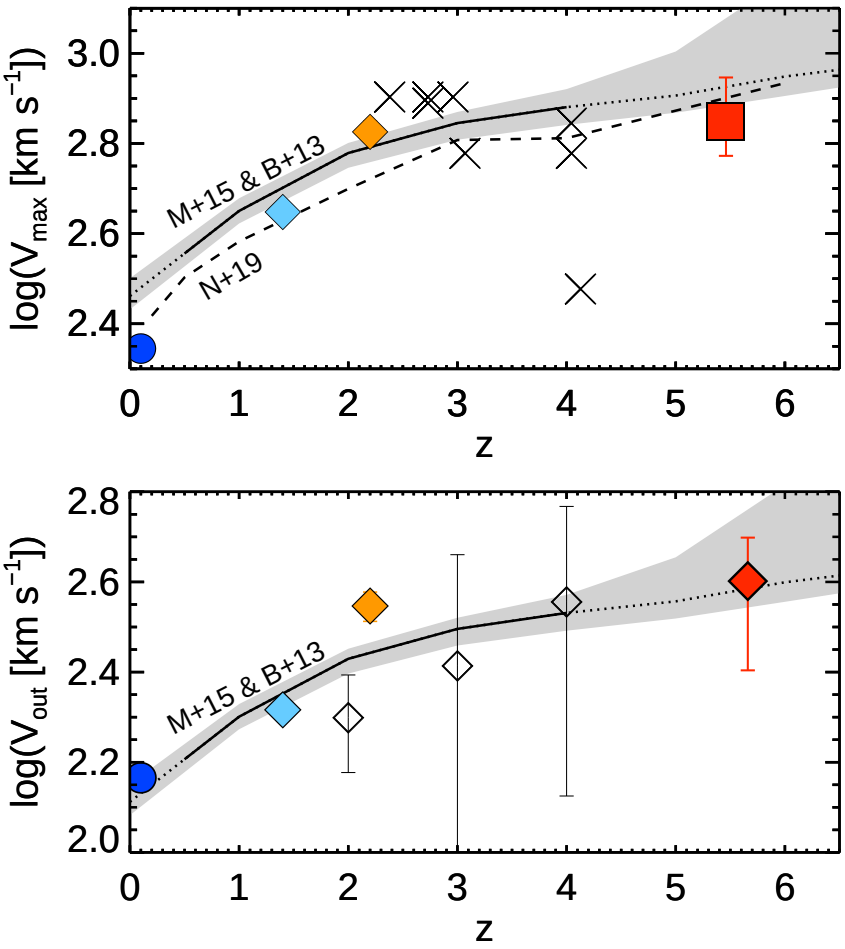

Figure 6.6 Redshift evolution of $v_{\rm max}$ (top) and $v_{\rm out}$ (bottom) in the star-forming galaxies with $M_* \sim 10^{10.1}$ $M_\odot$. The colored symbols are the same as in Figure 6.4, but for the red diamond that denotes $v_{\rm out}$ of the galaxies at $z = 5$–6 measured by a fit of the two-component Gaussian profile to the C II line. To compare the literature, we plot the values of the individual gravitationally-lensed sources in Jones et al. (2013, cross) and the composite spectra at $z \sim 2$, 3, and 4 presented by Du et al. (2018, open diamond), which have the median stellar masses of $\log(M_*/M_\odot) = 10.00$, 9.87, and 9.72, respectively. The solid lines indicate the evolution of the flux-weighted 90th (top) and 50th (bottom) outflow velocities at $M_* = 10^{10.1}$ $M_\odot$ in the FIRE simulations (Muratov et al. 2015) that we convert from the velocity–$v_{\rm cir}$ relation at $z = 0.5$–4 using Equations (4.1)–(4.2) and the SHMR of Behroozi et al. (2013). The evolution is extrapolated to $z < 0.5$ and $z > 4$ (dotted line) and the errors of the SHMR are shown in the shaded regions. The dashed line in the top panel indicates the evolution of the 90th percentile velocity at $M_* = 10^{10.1}$ $M_\odot$ in the IllustrisTNG simulation (Nelson et al. 2019).

6.3 Redshift Evolution of Outflow Velocities

We illustrate the redshift evolution of $v_{\rm max}$ in star-forming galaxies with $M_* \sim 10^{10.1}$ $M_\odot$ in the top panel of Figure 6.6. As shown in Section 6.2, $v_{\rm max}$ strongly increases from $z \sim 0$ to 2 and slightly or no increase from $z \sim 2$ to 6. Although many studies measure outflow velocities at a fixed redshift, a few studies investigate the redshift evolution of the velocities in wide redshift ranges. Jones et al. (2013) present the maximum outflow velocity of gravitationally lensed sources at $z \sim 2$–4 (cross). The stellar mass of these sources is not estimated and the outflow velocity of them is measured in a different manner from ours. However, the sources show similar outflow velocities to our $v_{\rm max}$ values at $z \sim 2$ and $z = 5$–6, except for a data point of $v_{\rm max} \simeq 300$ km s^{-1}. Jones et al. (2013) suggest a decrease in $v_{\rm max}$ at high redshift that is not statistically significant. We find no decrease at $z = 5$–6.

Du et al. (2018) discuss the redshift evolution of the central outflow velocity measured with a two-component fitting. As described in Section 5.3, because the composite spectrum of the $z6$-sample has large noises, we use only the outflow component for the fitting. A two-component fitting produces larger errors of the best-fit values than a one-component fitting, but to compare the velocity with the results of Du et al. (2018) at $z \lesssim 4$, we fit a two-component profile to the C II absorption line in the composite spectrum at $z = 5$–6. The fitting profile is a two-component Gaussian profile, which includes fewer fitting parameters than the two-component profile in this work. This analysis is identical to that used in Du et al. (2018). Before the fitting, the composite spectrum is smoothed by a Gaussian kernel so that the spectral resolution become similar to the composite spectrum at $z \gtrsim 2$ in Du et al. (2018). For a comparison, we also analyze the composite spectrum of the $z2$-sample.

The measured velocities are $v_{\rm out,gauss} = 400^{+100}_{-150}$ km s^{-1} at $z = 5$–6 and $v_{\rm out,gauss} = 352^{+26}_{-27}$ km s^{-1} at $z \sim 2$. In the bottom panel of Figure 6.6, we plot the measured $v_{\rm out,gauss}$ values, showing that the $v_{\rm out}$ and $v_{\rm out,gauss}$ redshift evolution has similar features to the $v_{\rm max}$ evolution: a strong increase from $z \sim 0$ to 2 and no increase from $z \sim 2$ to 6 within the errors. The latter is consistent with a result of Du et al. (2018). The $v_{\rm max}$, $v_{\rm out}$, and $v_{\rm out,gauss}$ values at $z \sim 0$, 1, 2, and 5–6 are listed in Table 6.1.

Table 6.1 Values of the data points at each redshift in Figure 6.6

redshift	$v_{\rm out}$ (km s^{-1})	$v_{\rm max}$ (km s^{-1})	$\log(M_*/M_\odot)$[a]
$z\sim0$	146 ± 5.2	221 ± 9.9	10.2
$z\sim1$	207 ± 5.0	445 ± 5.7	10.0
$z\sim2$	352^{+26}_{-27}[b]	673^{+35}_{-33}[b]	10.3
$z=5$–6	400^{+100}_{-150}[b]	700^{+180}_{-110}	10.1

[a]The mean stellar mass of the galaxies.

[b]This central outflow velocities are measured with two-component Gaussian fitting ($v_{\rm out,gauss}$).

The open diamonds indicate $v_{\rm out,gauss}$ at $z\sim2$, 3, and 4 given by Du et al. (2018). The $v_{\rm out,gauss}$ value of the z6-sample is comparable to those at $z\sim3$ and 4 within the marginally large error bars. However, the value of the z2-sample denoted by the orange diamond is not consistent with the one at $z\sim2$ denoted by the open diamond. In addition, the error bars of the open diamonds are generally larger than those of the filled symbols, in spite of the fact that Du et al. (2018) stacked a larger number of galaxy spectra than this study. These results may be attributed to the uncertainty of the systemic redshifts in Du et al. (2018), who determine the systemic redshifts from the Lyα emission or interstellar absorption lines. When individual spectra are stacked using the systemic redshifts, the uncertainties of the systemic redshifts broaden absorption lines in the composite spectrum. It is possible that this broadened absorption line produces low values and large errors of the best-fit parameters measured with the two-component fitting, which are sensitive to absorption-line profiles. We note that the median stellar masses of the galaxies in Du et al. (2018) are $\log(M_*/M_\odot)=10.00$, 9.87, and 9.72 at $z\sim2$, 3, and 4, respectively, which are less than M_* of our galaxies. It is also possible that this small M_* (i.e., small $v_{\rm cir}$) may lead to the low $v_{\rm out}$ value at $z\sim2$.

CHAPTER 7
DISCUSSION

7.1 Comparisons with theoretical models

Recent numerical and zoom-in simulations can be used to predict outflow velocities. These simulations compute energy input to the ISM surrounding SNe and investigate the statistics of galaxy and outflow properties (e.g., Muratov et al. 2015; Christensen et al. 2016; Mitchell et al. 2018; Nelson et al. 2019). Here we compare our results with simulation work that studies the redshift evolution of the outflow velocities. In the figures we convert M_* ($v_{\rm cir}$) into $v_{\rm cir}$ (M_*) in the simulation work by using Equations (4.1)–(4.2) and the SHMR in Behroozi et al. (2013).

Nelson et al. (2019) analyze ∼20,000 galaxies in the IllustrisTNG simulation to provide statistical relations between outflow and galaxy properties, including SN and AGN feedback. Figure 6.5 shows the outflow velocity, $v_{\rm out,90,r=10\ kpc}$, defined as the 90th percentile of the flux-weighted velocity distribution at a radius of 10 kpc, at z = 0.2, 1, 2, and 6 in stellar mass ranges similar to observational data points at the redshifts. This theoretical prediction by Nelson et al. (2019) agrees well with our observational measurements, although the scaling slope at $z \sim 0$ is different.

Muratov et al. (2015) calculate the flux-weighted velocity of the outflowing gas at one quarter of the halo virial radius with the Feedback in Realistic Environments (FIRE) simulations, which computes the thermal and momentum input to the ISM considering the stellar and SN feedback. The outflow velocity in the FIRE simulations tightly correlates with the halo circular velocity and the correlation does not exhibit the significant evolution over $z \sim 0.5$–4. Figure 6.5 illustrates that the correlation in the FIRE simulations at $z = 0.5$–4 is in good agreement with the tight linear relation which we present in Section 6.2. The measured outflow velocity of the z0-sample is $\sim$ 0.1 dex lower than the theoretical prediction, as Muratov et al. (2015) predict a drop of the outflow velocity at $z < 0.5$.

The increase in the maximum outflow velocity is also predicted by Barai et al. (2015), who carry out the Multi-Phase Particle Integrator (MUPPI) cosmological

simulations to find the outflow velocities evolution from $z \sim 0.8$ to 3.0, although we cannot quantitatively compare our results with this simulations.

These agreements with theoretical work support our result that $v_{\rm max}$ correlates with $v_{\rm cir}$ in a given stellar mass range. However, we note two factors that are important when one compares observations and theories: gas phases and galactocentric radii of outflows. Our observational technique traces low-ionized elements in warm gas ($\lesssim 10^4$ K). On the other hand, Muratov et al. (2015) and Nelson et al. (2019) compute the $v_{\rm max}$–$v_{\rm cir}(M_*)$ relation from outflowing gas with all temperatures. It is noteworthy that a non-negligible fraction of outflowing gas in numerical simulations would be in a hot, diffuse phase which are not observable with optical absorption lines (e.g., Mitchell et al. 2018; Nelson et al. 2019). Moreover, in some numerical simulations, outflows in a hot phase tend to exhibit faster velocities than those in cold phases (e.g., Tanner et al. 2016; Gallerani et al. 2018; Mitchell et al. 2018).

In addition to the gas phases, galactocentric distances of outflowing gas are different between observations and simulations. The observations with the "down-the-barrel" technique integrate outflowing-gas absorption along the line of sight and cannot explicitly distinguish absorption components at different radii. while most simulations compute outflow velocities at fixed radii. Even among the simulations, Nelson et al. (2019) and Muratov et al. (2015) compute velocities at different radii, 10 kpc and 0.25 halo virial radius, respectively, despite a radial dependence of outflow velocities (Nelson et al. 2019). Considering these all factors, it is difficult to interpret the similar $v_{\rm max}$–$v_{\rm cir}$ relation in this work, Nelson et al. (2019), and Muratov et al. (2015). Nevertheless, the agreement perhaps suggests that multi-phase outflows are accelerated following a common $v_{\rm max}$–$v_{\rm cir}$ relation, irrespective of gas phases.

In Figure 6.6 the black solid and dot-dashed lines indicate the redshift evolution of predicted outflow velocities at $M_* = 10^{10.1}$ $M_\odot$ based on the results given by the FIRE (Muratov et al. 2015) and the IllustrisTNG (Nelson et al. 2019) simulations, respectively. The evolution based on the simulations is in good agreement with the measured $v_{\rm max}$ and $v_{\rm out}$ values in this work, and also with those in Du et al. (2018) and Jones et al. (2013), except for one at $z \sim 4$.

7.1.1 Physical interpretation of the maximum outflow velocity

As discussed in the previous section, there are several problems when comparing observational results with theoretical predictions. One of the problems in observations is whether the derived maximum outflow velocity is the terminal outflow velocity, which is used in many outflow theories.

In monotonic accelerated outflow models, the galactocentric radii correspond to the velocities, i.e., the maximum outflow velocity traces the gas at the largest radius (Martin & Bouché 2009; Prochaska et al. 2011). Martin & Bouché (2009) estimate that the cold outflows can be detected up to $\simeq$ 6 kpc with the "down-the-barrel" technique on the assumption of the unity covering fraction at a launch radius $r_1 \simeq 200$ pc and the spectral continuum S/N of ~ 10 pixel^{-1}. Chisholm et al. (2016a) construct a similar accelerated model and fit it to the Si IV absorption line. The computed launch radius is 63 pc and the outflowing gas almost reaches the maximum velocity at $\lesssim$ 500 pc, although they assumes the terminal velocity of the outflows to be the maximum outflow velocity computed from the observation. The QSO absorption lines in QSO–galaxy pairs can trace the outflowing gas at large radii more directly than the "down-the-barrel" technique. Schroetter et al. (2019) observe 22 QSO–galaxy pairs with the Multi Unit Spectroscopic Explorer (MUSE) mounted on the Very Large Telescope and estimate the outflow velocities to be $\simeq$ 50–300 km s^{-1} at the galactocentric radii of 10–100 kpc, which is comparable to or less than the $v_{\rm max}$ values in this work, in consideration of the mass range. Given these observational results, the maximum outflow velocity of the cold outflows computed with the "down-the-barrel" technique is comparable to the terminal outflow velocity in theory.

However, the observational results above depend on the models adopted by the authors and S/N ratio of spectra. Because the covering fraction decreases with increasing radius, the "down-the-barrel" technique may miss the highest velocity components at large radii even in the accelerated scenario (Martin & Bouché 2009). As some numerical simulations predict, it is possible that the cold and warm outflowing gas is destructed by the interaction with the hot fluid outflows (e.g., Scannapieco & Brüggen 2015). In this case, the observable cold outflows may disappear during their

acceleration, showing rapid decreases of the covering fraction and the optical depth. The maximum outflow velocity is usually used to distinguish whether the outflows can escape the host galaxy into the IGM, but the uncertainties in the galactocentric distance of the outflowing gas make it difficult to estimate the escape velocity of the host galaxy. When the outflow velocity is smaller than the escape velocity, the acceleration models break and gas recycling to the host galaxy is predicted in fountain models, but again it is challenging to observe the radial acceleration of the outflows directly.

As a future prospects, revealing the outflow spacial structures by observations is a key to the acceleration process of the outflows and an interpretation of the outflow maximum velocity. High resolution spectroscopy of individual galaxies will present detailed absorption profiles that represent the velocity structure of the outflows along the line of sight (Chisholm et al. 2016a). The integral-field spectroscopy with the "down-the-barrel" technique and the spectroscopy of several background sources around a foreground galaxy will give spatial information of the outflows that is important to construct the outflow structure models. Although these observations are useful for future outflow studies, we still require better outflow models and theoretical predictions to reproduce the outflow properties from the high-resolution and the spatial observations. It is also desirable to derive the outflow properties in numerical simulations, such as the FIRE simulations and IllustrisTNG, in mock manners of observations, with considering the radiation transfer.

7.2 Physical Origins of $v_{\rm max}$ Evolution

In Section 6.3, we find that the redshift evolution of the outflow velocities at $z = 0$–6 at a fixed stellar mass of $M_* \sim 10^{10.1}$ $\mathrm{M}_\odot$. Moreover, the comparisons with the simulations in Section 7.1 support a monotonic increase in $v_{\rm max}$ from $z = 0$ to 6 at the fixed stellar mass. This increase can be explained by a tight correlation between $v_{\rm max}$ and $v_{\rm cir}$ and a monotonic increase in $v_{\rm cir}$with increasing redshift.

While $M_{\rm h}$ does not significantly change around $M_* \sim 10^{10.1}$ $\mathrm{M}_\odot$ at $z \sim 0$–6 (Behroozi et al. 2013), $r_{\rm h}$ is proportional to $(1+z)^{-1}$ at a fixed M_h (Equation 4.2).

This redshift dependence of the halo size is caused by the high cosmic density $\bar{\rho}$ at high redshift, following the equation of $\bar{\rho} \propto (1+z)^3$. Even if the stellar and halo mass is the same, dark halos at high redshift are dense and compact. This size evolution is observed in the effective radii of galaxies (Shibuya et al. 2015). Hence, Equation (4.1) gives the redshift dependence of the halo circular velocity as

$$v_{\rm cir} \propto (1+z)^{0.5}. \tag{7.1}$$

Given that $v_{\rm max}$ has the linear correlation with $v_{\rm cir}$ as shown in Figure 6.5, the redshift evolution in $v_{\rm max}$ (Figure 6.6) is explained as reflecting the redshift dependence of $v_{\rm cir}$. The power-law index of 0.5 reproduces the strong increase in $v_{\rm max}$ from $z \sim 0$ to 2 and the slight increase from $z \sim 2$ to 6.

7.3 Outflow-velocity correlation with $v_{\rm cir}$ and SFR

The outflow maximum velocity tightly correlates with the halo circular velocity (Figure 6.5), but it also has a strong correlation with SFR. To study the fundamental parameter that determines the outflow velocity over all redshifts, it is worth discussing correlations of $v_{\rm max}$ with galaxy properties over the wide redshift range. If there exists the fundamental parameter, it should exhibit a single scaling relation with $v_{\rm max}$ that holds at fixed redshifts and throughout all redshifts.

Figure 7.1 plots $v_{\rm max}$ as a function of $v_{\rm cir}$, M_*, SFR, SFR/M_*, and $\Sigma_{\rm SFR}$. Because galaxy sizes are unavailable at high-z due to the spacial resolutions, $\Sigma_{\rm SFR}$ is estimated on the assumption that galaxy sizes are proportional to redshifts by $(1+z)^{-1}$ (Shibuya et al. 2015). First, we calculate the Spearman's rank correlations, r, between $v_{\rm max}$ and the galaxy properties over all redshifts. While M_* has no correlation with $v_{\rm max}$, the other galaxy properties exhibit strong correlations of $r = 0.81$ ($v_{\rm cir}$), 0.78 (SFR), 0.90 (SFR/M_*), and 0.89 ($\Sigma_{\rm SFR}$) with the $> 3\sigma$ significance levels. Next, we perform a linear fitting to the data points both only at $z \sim 0$ and at all redshifts. The best-fit results are illustrated in Figure 7.1. The best-fit slopes at all redshifts (black dashed line) are positive for $v_{\rm cir}$, SFR, SFR/M_*, and $\Sigma_{\rm SFR}$. For $v_{\rm cir}$ and SFR, the

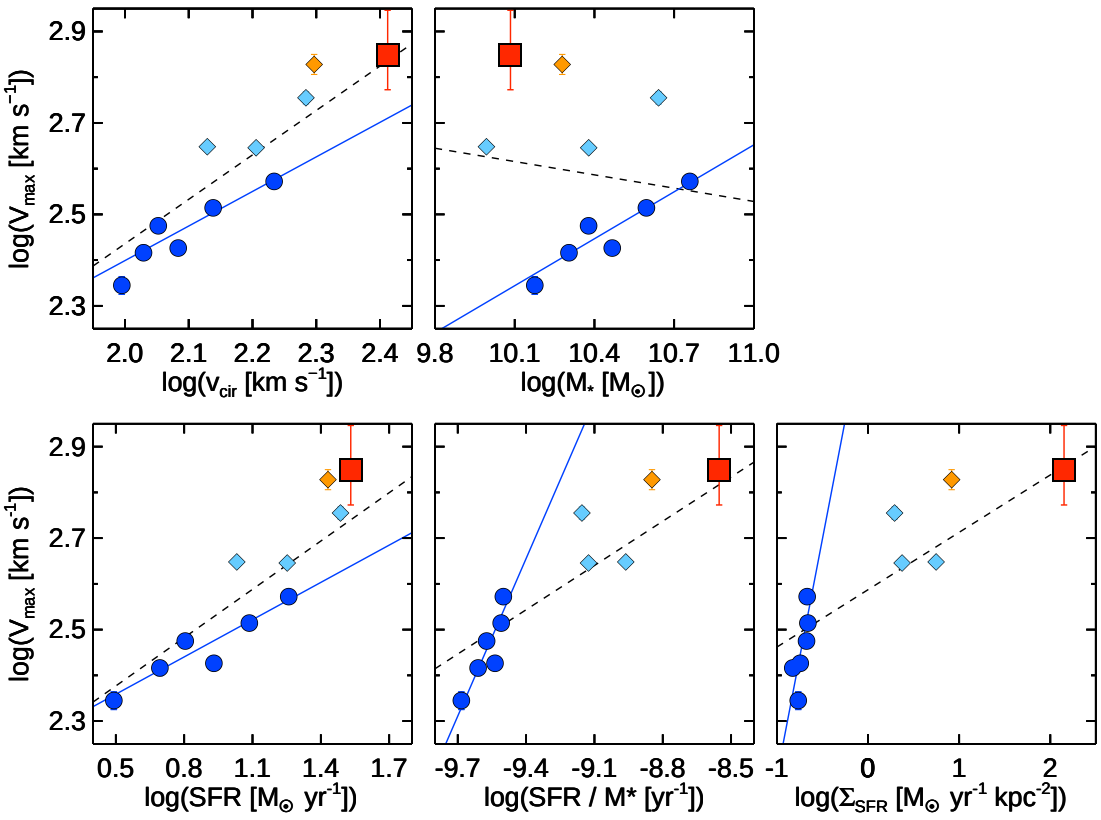

Figure 7.1 Correlations between $v_{\rm max}$ and galaxy properties. The symbols are the same as in Figure 6.5. The blue solid lines indicate the best-fit linear relations to the measurements of the $z0$-sample. The black dashed lines denote the best-fit linear relations to the measurements throughout all redshifts.

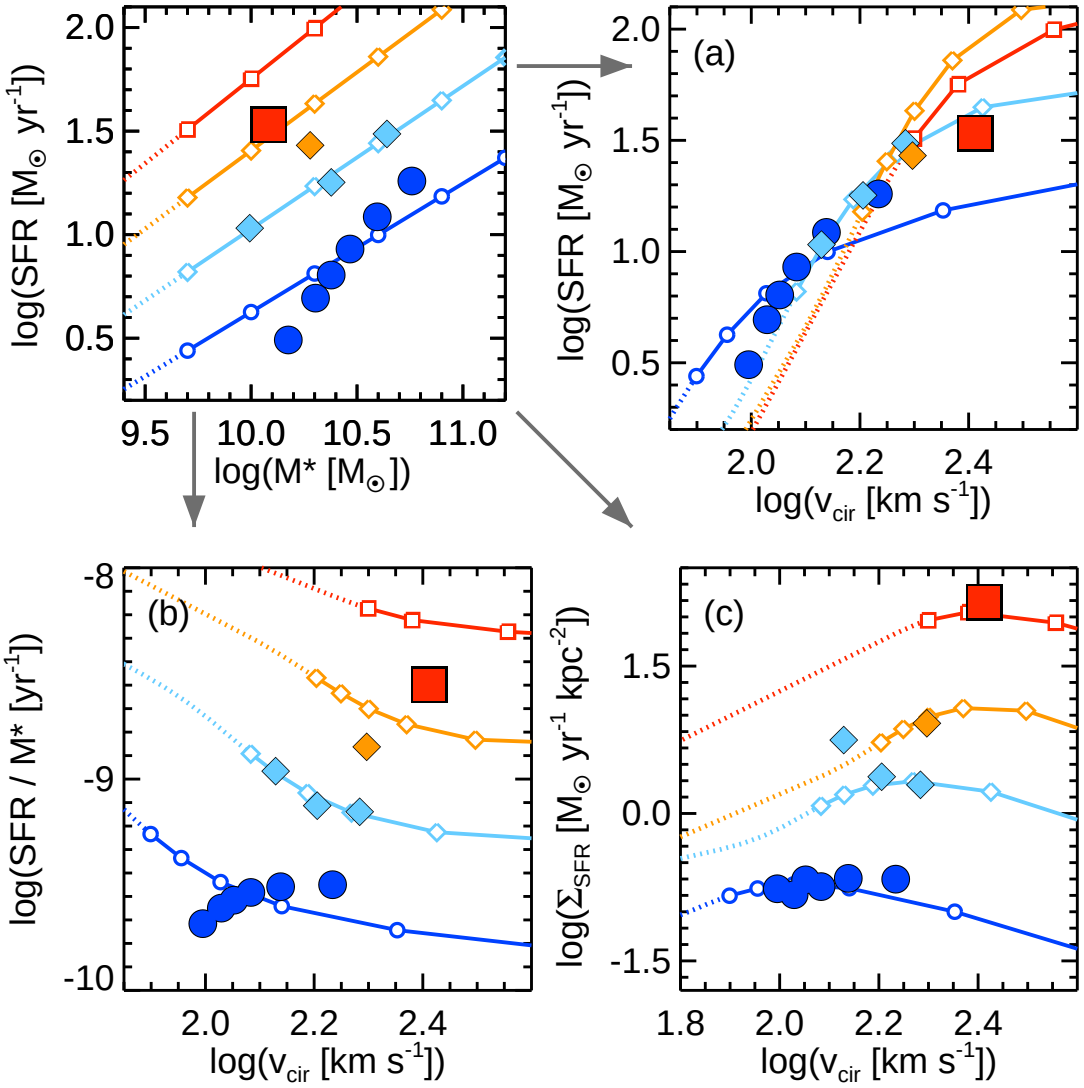

Figure 7.2 Models of the correlations of SFR, SFR/M_*, and $\Sigma_{\rm SFR}$ with $v_{\rm cir}$ for the star-forming main-sequence galaxies. The top left panel shows the main sequences at $z \sim 0.5$ (blue), 1 (cyan), 2 (orange), and 6 (red) that are presented by Speagle et al. (2014). The open symbols on the solid lines are plotted at the intervals of 0.3 dex of M_* for reference. The main sequences are extrapolated to $\log(M_*/{\rm M}_\odot) < 9.7$, indicated by the dotted lines. The filled symbols are the same as in Figure 6.5. (a) SFR versus $v_{\rm cir}$ where $v_{\rm cir}$ is converted from M_* in the top panel using the SHMR in Behroozi et al. (2013). SFR correlates with $v_{\rm cir}$ over $z = 0$–6. (b) SFR/M_* versus $v_{\rm cir}$. (c) $\Sigma_{\rm SFR}$ versus $v_{\rm cir}$; $\Sigma_{\rm SFR}$ is estimated on the assumption that galaxy sizes are proportional to redshifts by $(1+z)^{-1}$ (Shibuya et al. 2015). In the panels (b) and (c), the colored data points, which are in a similar M_* range, exhibit positive correlations. However, the solid lines demonstrate that the relations of the main-sequence galaxies depend on redshifts. Given a $v_{\rm cir}$–$v_{\rm max}$ correlation, the panels (b) and (c) suggest that SFR/M_* and $\Sigma_{\rm SFR}$ are unlikely to be the fundamental parameter.

data points show relatively small scatter within ~ 0.1 dex with respect to the best-fit relation at all redshifts. For SFR/M_* and $\Sigma_{\rm SFR}$, however, the best-fit relations at $z \sim 0$ (blue line) have large offsets from the data points at $z \sim$ 1–6, and the slopes of the best-fit relations at $z \sim 0$ and at all redshifts are very different from each other. These correlation and linear-fitting tests demonstrate that M_*, SFR/M_* and $\Sigma_{\rm SFR}$ show scaling relations at $z \sim 0$, but those scaling relations cannot explain the outflow velocity throughout all redshifts. Therefore, $v_{\rm cir}$ and SFR are likely to have the tightest single relations with $v_{\rm max}$ from $z \sim 0$ to 6.

The strong $v_{\rm max}$-correlations with $v_{\rm cir}$ and SFR imply a strong correlation between $v_{\rm cir}$ and SFR. To understand the SFR–$v_{\rm cir}$ relation independent of redshifts, it is helpful to see the distribution of the star-forming main-sequence galaxies on a SFR–$v_{\rm cir}$ plane. The top left panel of Figure 7.2 illustrates the main sequences at $z \sim 0.5$, 1, 2, and 6 that are presented by Speagle et al. (2014). The galaxies in the z0-, z1-, z2-, and z6-samples have similar stellar masses in the range of $10.0 < \log(M_*/{\rm M}_\odot) < 11.0$. We note that the main sequence at $z \sim 0.5$ (blue line) agrees with galaxies at $z \sim 0.1$ (blue circles) because we construct the z0-sample with the high $\Sigma_{\rm SFR}$ galaxies to select galaxies launching the outflows. By converting M_* into $v_{\rm cir}$, we plot the main sequences on a SFR–$v_{\rm cir}$ plane in the panel (a) of Figure 7.2. They show similar positive relations at all redshifts, leading to a positive correlation of the main-sequence galaxies, irrespective of redshifts. The data points indeed exhibit a strong positive correlation ($r = 0.99$) at the 5.8σ significance level. This result naturally explains that $v_{\rm max}$ has a correlation with $v_{\rm cir}$ and SFR simultaneously. In other words, constraining the fundamental parameter requires more measurements in a wide range of the stellar masses, SFR, and redshifts.

In the panels (b) and (c) of Figure 7.2, we plot the main sequences on SFR/M_*–$v_{\rm cir}$ and $\Sigma_{\rm SFR}$–$v_{\rm cir}$ planes, respectively, which are useful to understand Figure 7.1. Contrary to those on the SFR–$v_{\rm cir}$ plane, the main sequences have offsets in the positive direction from low to high redshifts. This demonstrates that the apparent positive correlation of the data points on the SFR/M_*–$v_{\rm cir}$ and $\Sigma_{\rm SFR}$–$v_{\rm cir}$ planes are simply because the galaxies have the similar stellar masses. Given a redshift-independent correlation between $v_{\rm cir}$ and $v_{\rm max}$ as discussed above, Figure 7.2 illustrates scaling

relations between $v_{\rm max}$ and galaxy properties at each redshift, which clearly reproduces the distribution of the data points in Figure 7.1. These simple models suggest that $v_{\rm max}$–SFR/M_* and $v_{\rm max}$–$\Sigma_{\rm SFR}$ relations of the main-sequence galaxies depend on redshifts, namely, that SFR/M_* and $\Sigma_{\rm SFR}$ are unlikely to be the fundamental parameter.

The parameters which most strongly correlate with $v_{\rm max}$ are $v_{\rm cir}$ and SFR, suggesting that the fundamental parameter is $v_{\rm cir}$ or SFR. This result agrees with previous observational studies that present positive correlations of $v_{\rm max}$ with M_* (Martin 2005; Rubin et al. 2014; Erb et al. 2012) or SFR (Kornei et al. 2012; Heckman et al. 2015; Heckman & Borthakur 2016). In many cases, the outflow properties are assumed to be connected with star-forming activities in galaxies. However, $v_{\rm cir}$ affects SFR through the halo accretion rate (e.g., Harikane et al. 2018; Tacchella et al. 2018) and this process contributes to form the SFR–$v_{\rm cir}$ correlation in Figure 7.2. Thus, because $v_{\rm cir}$ represents two key parameters for the outflow velocity, the gravitational potential and the star-forming activity, it is important to consider the possibility that $v_{\rm cir}$ is the fundamental parameter to determine the outflow velocity.

7.4 Mass Loading Factor

We have presented the results and discussion of the outflow velocities so far. Another important parameter of the outflows is the mass loading factor η, which is defined by Equation (2.1). The mass loading factor represents how effectively the outflows contribute the feedback process of the galaxy formation and evolution by transporting mass, energy, momentum, metal, and dusts into the CGM and IGM. In Section 7.4 and 7.5, we use the $z0$-, $z1$-, and $z2$-samples to derive and discuss the mass loading factor because of the low-S/N composite of $z6$-sample and limited redshift range of compliment chemical and radio observations used in following discussion.

Estimates of η requires many uncertain parameters. We assume that the fitting parameters of the outflow component can reproduce the outflow mass rate. We follow the derivations in previous studies that estimate the mass loading factor using the "down-the-barrel" technique (e.g., Weiner et al. 2009; Martin et al. 2012; Rubin et al.

2014). Our aim is to compare our observational results with theoretical predictions on the redshift evolution of the mass loading factors (Muratov et al. 2015; Barai et al. 2015; Mitra et al. 2015), under the set of the fiducial parameters.

We use the absorption lines of Na I D, Mg I, and C II to calculate η of the z0-, z1-, and z2-samples, respectively. Although the ionization energy and the absorption-line depth of C II is higher and deeper, respectively, than Na I D and Mg I, we directly compare the values of η estimated with the lines. This is because Figure 6.4 shows that $v_{\rm out}$ of Mg I and Mg II are comparable despite their different the ionization energy and the absorption-line depths.

To estimate $\dot{M}_{\rm out}$, we use the spherical flow model (Rupke et al. 2002; Martin et al. 2012) that assumes the bi-conical outflow which has the opening solid angle Ω. In the model, $\dot{M}_{\rm out}$ is given by Equation (2.39):

$$\dot{M}_{\rm out} = \bar{m}_p \Omega C_f r_1 N({\rm H}) v_{\rm out}. \tag{7.2}$$

We simply assume $\bar{m}_p = 1.4$ atomic mass unit and $\Omega = 4\pi$ that is a case of a spherical outflow. We also assume that r_1 is the same as the effective radius which are obtained from the r_e–M_* relation of Shibuya et al. (2015).

We estimate $N({\rm H})$ from $N({\rm X}^n)$ that is the column density of an ion ${\rm X}^n$. We define the gas-phase abundance of an element X with respect to hydrogen as $({\rm X/H})_{\rm gas} \equiv N({\rm X})/N({\rm H})$, where the column density of an element $N({\rm X})$ is given by $N(X) = \sum_n N({\rm X}^n)$. The ion column density $N({\rm X}^n)$ is expressed with Equation (2.33) as

$$N({\rm X}^n) = \frac{\tau_{0,{\rm out}} b_{\rm D,out}}{1.497 \times 10^{-15} \lambda_{\rm sys} f}. \tag{7.3}$$

The fitting parameters $\tau_{0,{\rm out}}$ and $b_{\rm D,out}$ are obtained in Section 5.3. The oscillator strengths f are taken from Morton (1991). Therefore, we can compute $N({\rm X}^n)$.

The ion column density $N({\rm X}^n)$ can be converted into the hydrogen column density $N({\rm H})$ with three parameters: the ionization fraction $\chi({\rm X}^n) \equiv N({\rm X}^n)/N({\rm X})$, the dust depletion factor $d({\rm X}) \equiv ({\rm X/H})_{\rm gas}/({\rm X/H})_{\rm c}$, and the cosmic metallicity at the redshifts $\mu({\rm X}) \equiv ({\rm X/H})_{\rm c}$, where the subscript c refers to the cosmic average. We thus estimate

N(H) with

$$N(\mathrm{H}) = \frac{N(\mathrm{X}^n)}{\chi(\mathrm{X}^n) d(\mathrm{X}) \mu(\mathrm{X})}. \tag{7.4}$$

Because it is difficult to obtain these three parameters by observations, we adopt fiducial parameters for our calculations as our best estimate. Given the redshift evolution of the metallicity (Zahid et al. 2013; Madau & Dickinson 2014), we assume that μ(X) is the solar metallicity at $z \sim 0$, and a half of the solar metallicity at $z \sim 1$ and 2, i.e., $\mu(\mathrm{X}) = 0.5(\mathrm{X/H})_\odot$. According to Morton (2003), the solar metallicity values are $\log(\mathrm{Na/H})_\odot = -5.68$, $\log(\mathrm{Mg/H})_\odot = -4.42$, and $\log(\mathrm{C/H})_\odot = -3.48$. The dust depletion factors are scaled to Milky Way values taken from Savage & Sembach (1996): d(Na) = 0.1, d(Mg) = 0.03, and d(C) = 0.4. Since `CLOUDY` photoionization models (Ferland et al. 1998, 2013) suggest $\chi(\mathrm{Na\,I\,D}) = 10^{-4}$–1 (Murray et al. 2007; Chisholm et al. 2016b), we take the moderate ionization fraction of $\chi(\mathrm{Na\,I\,D}) = 0.1$. Given a high ionization parameter at $z \gtrsim 1$ (Nakajima & Ouchi 2014), we choose $\chi(\mathrm{Mg\,I}) = \chi(\mathrm{Na\,I\,D})/2 = 0.05$. Because Si II, which has a similar ionization energy to C II, exhibits $\chi(\mathrm{Si\,II}) \simeq 0.2$ (Chisholm et al. 2016b), we assume $\chi(\mathrm{C\,II}) = 0.2$ that is the same value as Si II. In summary, the parameters for Na I D, Mg I, and C II are (χ, d, μ) = (0.1, 0.1, 2.1×10^{-6}), (0.1, 0.03, 1.9×10^{-5}), and (0.2, 0.4, 1.7×10^{-4}), respectively. The hydrogen column density N(H) is calculated by Equation (7.4) with the parameter sets of (χ, d, μ).

We estimate $\dot{M}_{\rm out}$ by Equation (7.2) with the fitting parameters C_f and $v_{\rm out}$ that are measured in Section 5.3. If we use the velocity of $v_{\rm max}/2$, instead of $v_{\rm out}$, the result does not change. Finally, the mass loading factor η is obtained by Equation (2.35). We find that our samples show $0 \lesssim \log\eta \lesssim 1$, which are consistent with the results of previous studies (e.g., Heckman et al. 2015). Figure 7.3 shows η as a function of the halo circular velocity $v_{\rm cir}$. We fit a power-law function to the z0-sample values and obtain the best-fit relation $\eta = \eta_1 v_{\rm cir}^a$ for $\eta_1 = 2.9 \pm 16.3$ and $a = -0.2 \pm 1.1$. This scaling relation is consistent with the previous studies within the 1σ uncertainties: $a = -0.98$ for strong outflows investigated with the UV observations of the local galaxies (Heckman et al. 2015) and $a = -1.0$ for $v_{\rm cir} > 60$ km s^{-1} found with the FIRE simulations (Muratov et al. 2015). Our result, $a = -0.2 \pm 1.1$, is consistent

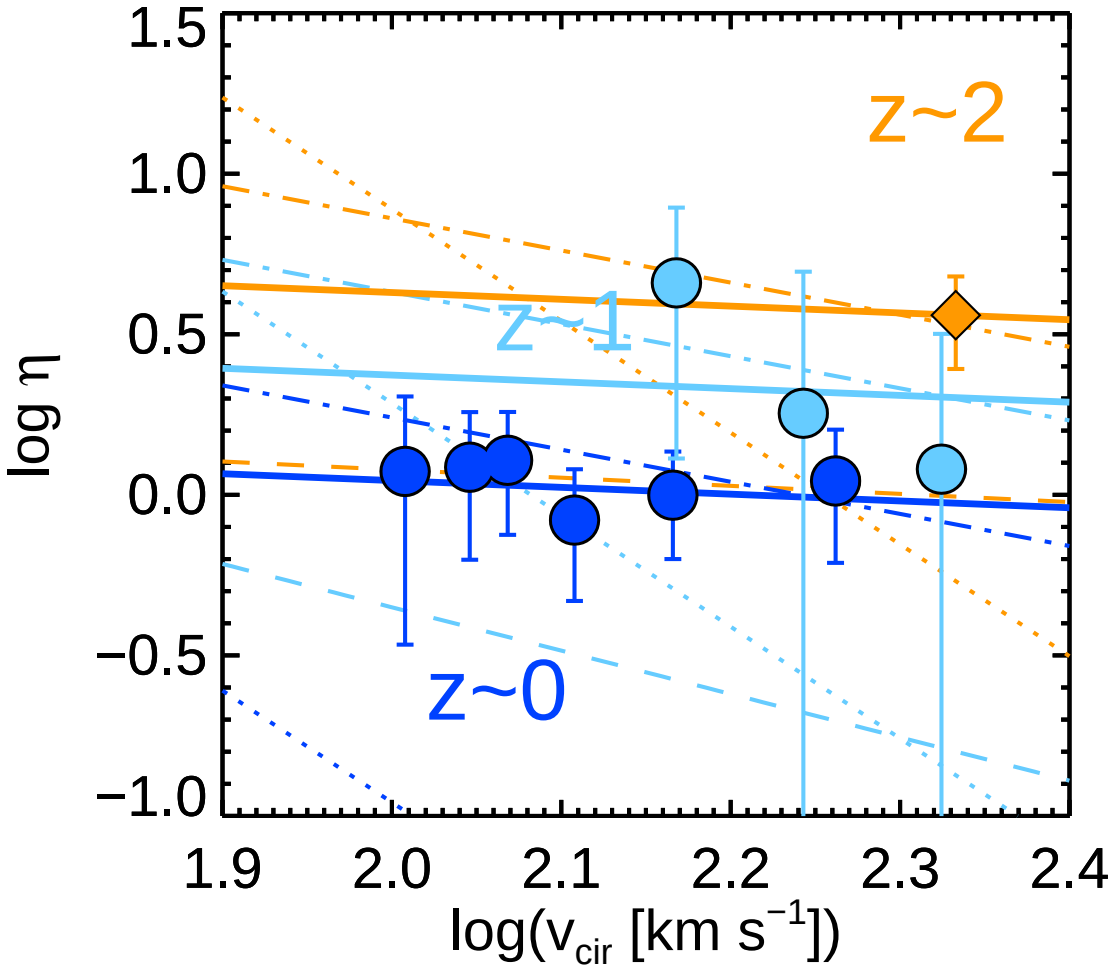

Figure 7.3 Mass loading factor as a function of $v_{\rm cir}$. The data points are the same as those in Figure 6.4. The colors of blue, cyan, and orange correspond to $z \sim 0$, 1, and 2, respectively. The solid lines denote the least-square fitting results. The dot-dashed, dashed, and dotted lines indicate the models presented by Muratov et al. (2015), Barai et al. (2015), and Mitra et al. (2015), respectively.

with the momentum-driven model ($a = -1$), although it is also consistent with no correlation, i.e., $a = 0$. It is not conclusive, but we can rule out the energy-driven model ($a = -2$) at the 90 percentile significance level. We also plot the data of the $z1$- and $z2$-samples in Figure 7.3, but we cannot discuss the scaling relation of them due to few data points. Given Equations (7.2) and (7.4), changes of the fiducial parameter sets do not change the best-fit slope at a fixed redshift.

Figure 7.3 suggests that the data points are consistent with an η increase from $z \sim 0$ to 2 at a given circular velocity. We fit a power-law function $\eta = \eta_1 v_{\rm cir}^a$ to the $z0$-, $z1$-, and $z2$-samples at the fixed slope of $a = -0.2$ that is the best-fit parameter of the $z0$-sample. We obtain the best-fit parameters $\eta_1 = 2.9 \pm 0.5$, 6.3 ± 4.5, and 11.3 ± 3.6 for the $z0$-, $z1$-, and $z2$-samples, which are illustrated in Figure 7.3 with the blue, cyan, and orange solid lines, respectively.

The redshift evolution of η is obtained as $\eta \propto (1+z)^{1.2\pm0.3}$ with a power-law fitting.

7.5 Physical Origins of η Evolution

The redshift evolution of the mass loading factor is theoretically investigated at a fixed halo circular velocity. The FIRE simulations (Muratov et al. 2015) and the MUPPI simulations (Barai et al. 2015) compute the mass loading factor with numerical simulations to find an increase of η with increasing redshift. In particular, the relation $\eta \propto (1+z)^{1.3}$ found by Muratov et al. (2015) agrees with our results (Figure 7.3). Mitra et al. (2015) present an analytic baryon-cycle equilibrium model to reproduce the statistical galaxy relations and predict an increasing trend of the mass loading factor. On the other hand, the illustrisTNG simulations (Nelson et al. 2019) shows a significant decrease at high-mass regime due to the SMBH activity.

In this section, we discuss the physical origins of the outflow redshift evolution. In some theories, the origin links with a large amount of gas at high redshift. Barai et al. (2015) claim that gas-rich galaxies at high redshift launch outflows with high $v_{\rm out}$ and η. Similarly, Hayward & Hopkins (2015) find that the η value increases exponentially with an increase in the gas fractions towards high redshift.

Here, we connect the redshift evolution of the outflows with the redshift evolution of SFR and the cool-gas mass in a galaxy. If we assume that $\dot{M}_{\rm out}$ is proportional to the cool HI gas mass $M_{\rm gas}^{\rm cool}$, we can rewrite Equation (2.35) as

$$\eta = \frac{\dot{M}_{\rm out}}{\rm SFR} \propto \frac{M_{\rm gas}^{\rm cool} v_{\rm out}}{\rm SFR}. \tag{7.5}$$

Hence, the mass of the cool gas in the galaxy is

$$M_{\rm gas}^{\rm cool} \propto \frac{\eta {\rm SFR}}{v_{\rm out}}. \tag{7.6}$$

Below we calculate the redshift dependence of SFR, $v_{\rm out}$, η, and $M_{\rm gas}^{\rm cool}$ at a fixed stellar mass of $\log(M_*/M_\odot) = 10.5$. The redshift evolution of SFR at a fixed stellar mass is given by Speagle et al. (2014):

$${\rm SFR}/M_* \propto (1+z)^{2.8}. \tag{7.7}$$

If we assume that $v_{\rm out}$, $v_{\rm max}$, and $v_{\rm cir}$ follow the same dependence on z, their evolution is expressed as Equation (7.1). By assuming a momentum-driven model, the redshift evolution of η derived from our measurements is $\eta \propto (1+z)^{1.2\pm0.3} v_{\rm cir}^{-1}$. Substituting these equations into Equation (7.6), we obtain the redshift dependence of $M_{\rm gas}^{\rm cool}$ by

$$M_{\rm gas}^{\rm cool} \propto (1+z)^{3.0\pm0.3}. \tag{7.8}$$

Equation (7.8) suggests that increasing $M_{\rm gas}^{\rm cool}$ causes the increases in outflow velocities, mass loading factors, and SFR with increasing redshift. This increasing trend of $M_{\rm gas}^{\rm cool}$ is consistent with independent observational results. If we assume that the molecular gas mass is proportional to $M_{\rm gas}^{\rm cool}$ at a given stellar mass, there is a relation of $M_{\rm gas}^{\rm cool} \propto (1+z)^{2.7}$ at $z \sim 0$–3 obtained by the radio observations of Genzel et al. (2015). This relation is consistent with Equation (7.8) within the 1σ uncertainty.

As noted in Section 7.4, the parameter sets used for deriving η include large uncertainties. The uncertainties described in previous studies are factors of 1.7 for $\chi({\rm X}^n)$ (Chisholm et al. 2016b), 1.3 for $d({\rm X})$ (Savage & Sembach 1996), and 1.2 for

μ(X) (Zahid et al. 2013). The total uncertainty of $\chi(X^n)$, d(X), and μ(X) is $\simeq 0.4$ dex.

We thus think that the conclusion of an increase in η is not strong. However, we can securely claim that the theoretical models are consistent with our observational results under the assumption of the fiducial parameter sets shown in Section 7.4.

7.6 Lyman-continuum leakage

Finally, we discuss the cosmic reionization with absorption-line analysis of the $z6$-sample. The redshift $z = 5$–6 is near the end of the cosmic reionization, when the neutral IGM has been ionized. Plausible ionizing sources are young, low-mass galaxies (e.g., Robertson et al. 2015; Ishigaki et al. 2018), but their contribution is still a matter of debate. A key physical parameter is the escape fraction of the Lyman-continuum (LyC) photons from galaxies ($f_{\rm esc}$). Because it is possible that the outflows help increase $f_{\rm esc}$ by creating holes in the neutral ISM from which the LyC photons can escape, the high-z galaxies with outflows in this work are appropriate for the reionization study. However, direct measurements of $f_{\rm esc}$ are challenging for galaxies at $z = 5$–6 because the LyC photons almost disappear by ionizing the neutral IGM. In this section, we discuss the $f_{\rm esc}$ value of our galaxies at $z = 5$–6 with two indirect methods regarding the absorption lines.

In the first method, we calculate the covering fraction from the metal absorption lines. In cases of the optically-thick outflowing gas, absorption lines are saturated and the line depth gives the covering fractions. Assuming that the low-ionized elements are associated with the neutral-hydrogen gas, Jones et al. (2013) evaluate an upper limit of $f_{\rm esc}$from the maximum covering fraction ($C_f^{\rm max}$) of the low-ionized absorption lines. Because our composite spectrum has the low continuum S/N, we define $C_f^{\rm max}$ as $C_f^{\rm max} = 1 - F_{\rm SiII}$, where $F_{\rm SiII}$ is the median flux density of the Si II line from -350 to -100 km s^{-1} in the normalized spectrum. Its error is calculated with the parametric bootstrap method based on the spectral noise. The measured value is $C_f^{\rm max} = 0.8 \pm 0.2$. We note that this $C_f^{\rm max}$ value is likely smaller than the value evaluated by the method in Jones et al. (2013) because our $C_f^{\rm max}$ value is calculated

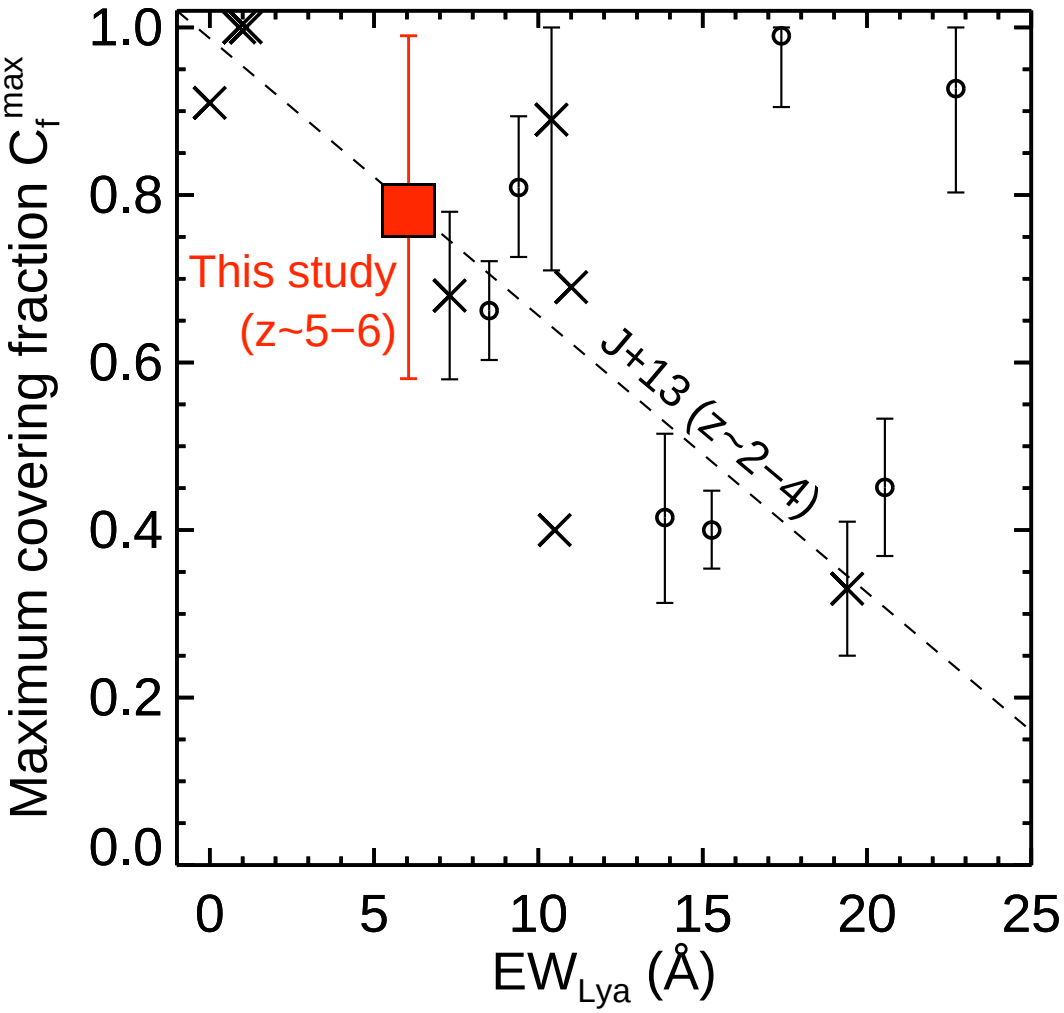

Figure 7.4 The maximum covering fraction $C_f^{\rm max}$ as a function of the Lyα equivalent width. The red square denotes the result at $z = 5$–6. The crosses and the open circles indicate the values of gravitationally-lensed sources at $z \sim 2$–4 (Jones et al. 2013) and $z \sim 4$–5 (Leethochawalit et al. 2016), respectively. The dashed line is the best-fit linear relation to the crosses (Jones et al. 2013).

in the wide velocity range of 250 km s^{-1}. We additionally measure the Lyα equivalent width (EW$_{\rm Ly\alpha}$) of the composite spectrum to be EW$_{\rm Ly\alpha} = 6.05 \pm 0.45$ Å, using the emission strength from the stellar continuum at 1216–1221 Å.

Figure 7.4 illustrates $C_f^{\rm max}$ as a function of EW$_{\rm Ly\alpha}$. Our measurement at $z = 5$–6 (red square) is consistent with previous results (Jones et al. 2013; Leethochawalit et al. 2016) and on the linear relation at $z \sim 2$–4 presented by Jones et al. (2013, dashed line). This is the first observational result showing that the linear relation between $C_f^{\rm max}$ and EW$_{\rm Ly\alpha}$ holds even at $z > 5$, provided that the relation is independent of the stellar mass. Using the $C_f^{\rm max}$ value corresponding to EW$_{\rm Ly\alpha} = 6.05$ Å on the relation, we obtain an upper limit of $f_{\rm esc}$ to be $\simeq 0.2$. This secure upper limit is too weak to constrain models where bright galaxies contribute to the cosmic reionization (e.g., $\sim 10\%$; Sharma et al. 2017). However, Jones et al. (2013) emphasize that the property derived by this method is an upper limit. Following an equation derived by Chisholm et al. (2018), who propose indirect estimations of $f_{\rm esc}$ using local LyC leaking galaxies, we obtain $f_{\rm esc} \lesssim 0.5 - 0.6 C_f^{\rm max} = 0.02$. Hence, the intrinsic $f_{\rm esc}$ is likely much lower than the upper-limit value.

In the second method, we consider the shape of the absorption-line profile using the outflow velocities. Chisholm et al. (2017a) calculate the ratio of the maximum outflow velocity to the central outflow velocity ($v_{90}/v_{\rm cen}$) of galaxies at $z = 0$. They find that the LyC leaking galaxies exhibit smaller ratios, $v_{90}/v_{\rm cen} \lesssim 5$, than galaxies without LyC leakage, although there are several galaxies with $v_{90}/v_{\rm cen} < 5$ but $f_{\rm esc} = 0$. Here we use $|v_{\rm max}/v_0|$ for an alternative to $v_{90}/v_{\rm cen}$ used in Chisholm et al. (2017a). The ratio for the galaxies at $z = 5$–6 is obtained to be $|v_{\rm max}/v_0| = 2.0 \pm 0.2$. This result suggests that the galaxies at $z = 5$–6 are the LyC leaking galaxies, in contrast to the result of the first method. Further studies on both the LyC photons and the absorption-line properties will provide key quantities to address the challenge of estimating $f_{\rm esc}$ for galaxies at the epoch of reionization.

CHAPTER 8
CONCLUSION

We study properties of galactic-scale cool/warm outflows in star-forming galaxies at $z \sim 0$, 1, 2, and 5–6. We construct rest-frame UV and optical spectroscopic samples of star-forming galaxies in a similar stellar-mass range, taken from the SDSS DR7 at $z \sim 0$, the DEEP2 DR4 at $z \sim 1$, and the Erb et al. (2006a,b) catalog at $z \sim 2$, and the Capak et al. (2015) catalog at $z = 5$–6. We stack individual galaxy spectra in bins of SFR with respect to the systemic redshift to obtain high-S/N composite spectra appropriate for the "down-the-barrel" technique. We model the blueshifted outflow component of absorption lines by fitting a multi-component profile to the absorption lines of Na I D $\lambda\lambda$5891.58,5897.56 for the $z \sim 0$ galaxies, Mg I λ2852.96 and Mg II $\lambda\lambda$2796.35,2803.53 for the $z \sim 1$ galaxies, Si II λ1260, C II λ1334.53, Si II λ1527, and C IV $\lambda\lambda$1548.20,1550.78 for the $z \sim 2$ galaxies, and Si II λ1260, C II λ1334.53, and Si IV λ1527 for the $z = 5$–6 galaxies. From the best-fit outflow component, the outflow properties are measured. Our findings are summarized below.

1) We measure the maximum outflow velocity $v_{\rm max}$ and the central outflow velocity $v_{\rm out}$. The $v_{\rm out}$ values are all significantly positive, indicating that the absorption lines are blueshifted by the outflows. The $v_{\rm max}$ and $v_{\rm cir}$ values at $z \sim 0$–2 are consistent with previous studies. The outflow velocities for the low-ionized lines are comparable to those for the high-ionized lines.

2) By determining the systemic redshift with the ALMA [C II] 158 μm line, we present the first measurement of the outflow velocities of galaxies at $z = 5$–6. A simultaneous fitting to the Si II and C II lines yields $v_{\rm max} = 700^{+180}_{-110}$ km s^{-1}. A two-component Gaussian fitting yields $v_{\rm out} = 400^{+100}_{-150}$ km s^{-1}.

3) The scaling relations between the outflow velocities and SFR at $z \sim 0$ are $v_{\rm max} \propto {\rm SFR}^{0.25\pm0.04}$ for $v_{\rm max}$ and $v_{\rm out} \propto {\rm SFR}^{0.03\pm0.03}$ for $v_{\rm out}$. The steep slope of $v_{\rm max}$ is consistent with previous studies. The flat slope of $v_{\rm out}$ is consistent with work that uses similar two-component fitting to measure the central outflow velocity.

4) The outflow velocities increase with increasing redshift in a similar stellar mass range. We compare the velocities measured with absorption lines with similar ionization energy and absorption depth: Na I D (IE $\simeq$ 5.1 eV) and Mg I (IE $\simeq$ 7.6 eV) from $z \sim 0$ to 1, and Mg II (IE $\simeq$ 15 eV) and C II (IE $\simeq$ 24 eV) from $z \sim 1$ to 2. This comparison demonstrates the redshift evolution of $v_{\rm max}$ and $v_{\rm out}$ that exhibits a strong increase from $z \sim 0$ to 2 and a weak increase from $z \sim 2$ to 6, at the fixed stellar mass of $\log(M_*/{\rm M}_\odot) \sim 10.1$.

5) Over $z \sim$ 0–6, $\log v_{\rm max}$ is linearly correlated with the halo circular velocity ($\log v_{\rm cir}$) that are estimated from the stellar mass. This linear correlation can explain the increasing features of the $v_{\rm max}$ evolution because $v_{\rm cir}$ is proportional to $(1+z)^{0.5}$ for the galaxies with $\log(M_*/{\rm M}_\odot) \sim 10.1$, at which the halo mass is almost constant over $z \sim$ 0–6.

6) The correlation between $v_{\rm max}$ and $v_{\rm cir}$ is in good agreement with relations predicted by the IllustrisTNG (Nelson et al. 2019) and the FIRE (Muratov et al. 2015) simulations. Although there are differences of gas phases and galactocentric radii between the simulation and observational work, this good agreement perhaps suggest that the multi-phase outflows are driven by a common $v_{\rm max}$–$v_{\rm cir}$ relation.

7) The outflow maximum velocity $v_{\rm max}$ strongly correlates with $v_{\rm cir}$, SFR, SFR/M_*, and $\Sigma_{\rm SFR}$ over $z =$ 0–6. Moreover, on the $v_{\rm max}$–$v_{\rm cir}$ and $v_{\rm max}$–SFR planes, the linear scaling relations at $z = 0$ explain the whole distribution from $z = 0$ to 6. Given that the $v_{\rm max}$–$v_{\rm cir}$ relation holds at any redshifts, the models of the star-forming main sequences reproduce the relation between $v_{\rm max}$ and galaxy properties at $z =$ 0–6. For these reasons, $v_{\rm cir}$ or SFR are likely to be the fundamental parameter to determine $v_{\rm max}$ with a single relation throughout all redshifts. Considering that $v_{\rm cir}$ has an impact on SFR through the halo accretion rate, it is possible that $v_{\rm cir}$ is the fundamental parameter.

8) We calculate the mass loading factor η using the absorption lies of Na I D at $z \sim 0$, Mg I at $z \sim 1$, and C II at $z \sim 2$, the spherical outflow model, and

assumptions of the fiducial parameters. The scaling relation between η and the halo circular velocity $v_{\rm cir}$ is given by $\eta \propto v_{\rm cir}^{a}$ for $a = -0.2 \pm 1.1$ at $z \sim 0$. The slope of $a = -0.2 \pm 1.1$ is consistent with a mechanism based on the momentum-driven model, which predicts $a = -1$.

9) The mass loading factor η is consistent with an increase from $z \sim 0$ to 2. The increase in η is by $\eta \propto (1+z)^{1.2\pm0.3}$ with the fiducial parameter sets assumed in Section 7.4. We note that the parameter sets include large uncertainties.

10) Our observations show the increases in $v_{\rm out}$, $v_{\rm max}$, and η with increasing redshift. Under the assumption that the outflow mass is proportional to the cold gas mass in galaxies, these results are consistent with an increase in the cold gas mass of high-redshift galaxies, which is confirmed by radio observations.

11) Absorption-line profiles are also used for indirect estimations of the escape fraction of the LyC photons ($f_{\rm esc}$). We find that the maximum covering fraction of the Si II line and the Lyα equivalent width of the composite spectrum at $z = 5$–6 are consistent with a relation at $z \sim 2$–4. The intrinsic $f_{\rm esc}$ would be much lower than the secure upper limit $f_{\rm esc} < 0.2$, while the ratio $|v_{\rm max}/v_0|$ is comparable to the values of the local LyC leaking galaxies.

Through this thesis, we have studied the galactic outflows in star-forming galaxies from $z \sim 0$ to 6. We have shown the increase of the outflow velocities from $z \sim 0$ to 6, and discuss the relation between the outflow and galaxy properties, the physical origin of the outflow redshift evolution, and connection with the numerical simulations. Using fiducial parameters, we have also estimated the mass loading factor and given an interpretation of its evolution. This is pioneering work to investigate the redshift evolution of the galactic outflows.

In early 2022, the Prime Focus Spectrograph (PFS) mounted on the Subaru telescope will start observations. The PFS is able to target 2,400 objects with fibers, in a wide field of view of 1.3 degree diameter, in the wavelength range from 3800 Å to 1.26 μm at a time. The Subaru strategic program with PFS will provide a large spectroscopic sample of galaxies at $z_{\rm sys} = 1$–4 and enables statistical outflow studies at high

redshift. Recently ALMA observations have been extending the redshift records of galaxies and advancing studies of high-z galaxies. The James Webb Space Telescope will be launched within a few years. These fantastic facilities will progress studies on the redshift evolution of the galactic outflows, contributing to revealing the barion cycle around galaxies and feedback process in the galaxy evolution.

APPENDIX A
EVALUATION OF THE ABSORPTION-LINE FITTING

A.1 Table of the Best-fit Values

Table A.1 lists the best-fit values, the minimum chi-square, and the degree of freedom for the composite spectra that includes spectra re-sampled with the nearest-bins methods.

Table A.1 Best-fit parameters of the composite spectra

sample	line	$\lambda_{\rm out}$ (Å)	$\tau_{0,\rm out}$	$C_{\rm f,out}$	$b_{\rm D,out}$ (km s^{-1})	$\tau_{0,\rm sys}$	$C_{\rm f,sys}$	$b_{\rm D,sys}$ (km s^{-1})	$\chi^2_{\rm min}$	DoF
z0-sample	Na I D	$5888.8^{+0.1}_{-0.1}$	$0.62^{+0.18}_{-0.08}$	0.20[a]	$59.5^{+7.3}_{-12.1}$	-[c]	-[c]	-[c]	145.1	22
z0-sample	Na I D	$5888.6^{+0.1}_{-0.1}$	$0.69^{+0.06}_{-0.06}$	0.20[a]	$78.5^{+6.3}_{-5.4}$	-[c]	-[c]	-[c]	227.0	22
z0-sample	Na I D	$5888.4^{+0.1}_{-0.1}$	$0.63^{+0.04}_{-0.04}$	0.20[a]	$107.1^{+7.1}_{-6.1}$	-[c]	-[c]	-[c]	104.9	22
z0-sample	Na I D	$5888.7^{+0.1}_{-0.1}$	$0.66^{+0.50}_{-0.12}$	$0.18^{+0.02}_{-0.06}$	$106.6^{+8.5}_{-7.6}$	-[c]	-[c]	-[c]	80.8	22
z0-sample	Na I D	$5888.7^{+0.1}_{-0.1}$	$0.75^{+0.04}_{-0.04}$	0.20[a]	$123.9^{+6.1}_{-5.8}$	-[c]	-[c]	-[c]	111.4	22
z0-sample	Na I D	$5888.3^{+0.4}_{-0.1}$	$0.80^{+0.17}_{-0.05}$	0.20[a]	$152.9^{+12.7}_{-6.4}$	-[c]	-[c]	-[c]	130.5	22
z1-sample	Mg I	$2851.0^{+0.4}_{-0.3}$	$6.27^{+2.98}_{-4.31}$	$0.17^{+0.03}_{-0.04}$	$143.2^{+24.5}_{-35.1}$	$3.8^{+3.8}_{-2.0}$	$0.10^{+0.03}_{-0.03}$	$107.8^{+15.9}_{-17.8}$	323.0	279
z1-sample	Mg I	$2851.6^{+0.1}_{-0.2}$	$7.87^{+2.13}_{-4.22}$	0.20[a]	$72.5^{+29.4}_{-12.2}$	$2.8^{+9.2}_{-2.5}$	$0.06^{+0.14}_{-0.04}$	$78.4^{+33.8}_{-78.4}$	330.5	279
z1-sample	Mg I	$2851.4^{+0.1}_{-0.2}$	$6.90^{+3.10}_{-4.89}$	$0.16^{+0.04}_{-0.02}$	$102.1^{+22.7}_{-16.2}$	$4.1^{+7.9}_{-3.9}$	$0.04^{+0.14}_{-0.02}$	$150.0^{+31.3}_{-106.8}$	306.0	279
z1-sample	Mg II	$2794.4^{+0.1}_{-0.1}$	10.00[a]	$0.41^{+0.01}_{-0.01}$	$118.7^{+4.1}_{-4.2}$	-[c]	-[c]	-[c]	685.4	280
z1-sample	Mg II	$2794.8^{+0.1}_{-0.1}$	10.00[a]	$0.51^{+0.02}_{-0.02}$	$123.8^{+4.8}_{-5.5}$	$1.9^{+10.1}_{-0.6}$	$0.09^{+0.12}_{-0.09}$	$36.8^{+27.7}_{-36.8}$	438.5	280
z1-sample	Mg II	$2794.2^{+0.1}_{-0.1}$	10.00[a]	$0.37^{+0.01}_{-0.01}$	$160.2^{+7.7}_{-6.8}$	-[c]	-[c]	-[c]	475.7	280
z2-sample	C II	$1332.5^{+0.2}_{-0.2}$	70.00[a]	$0.30^{+0.03}_{-0.02}$	130.0[a]	70.0[a]	$0.59^{+0.07}_{-0.05}$	$107.3^{+15.2}_{-15.0}$	50.7	46
z2-sample	C IV	$1545.7^{+0.1}_{-0.1}$	70.00[a]	$0.47^{+0.02}_{-0.02}$	130.0[a]	$1.1^{+15.2}_{-0.5}$	1.00[a]	$27.7^{+41.4}_{-16.4}$	667.1	61
z6-sample	Si II	$1258.9^{+0.3}_{-0.4}$	10.00[a]	$0.97^{+0.03}_{-0.21}$	$156.5^{+85.4}_{-41.3}$	-	-	-	110.4	130
z6-sample	C II	$1333.7^{+0.7}_{-0.3}$	10.00[a]	$0.72^{+0.28}_{-0.13}$	$261.6^{+38.1}_{-159.1}$	-	-	-	298.4	193
z6-sample	Si IV	$1392.5^{+0.7}_{-0.2}$	10.00[a]	1.00[a]	$166.8^{+180.2}_{-59.6}$	-	-	-	375.5	361
z6-sample	Si II +C II [d]	–	10.00[a]	$0.84^{+0.16}_{-0.16}$	$202.3^{+46.7}_{-50.9}$	-	-	-	299.6	330

[a] A parameter reaches an edge of the range of the parameter.

[b] Optically thick case.

[c] A parameter is not determined because no systemic component is selected as the best-fit result.

[d] This raw lists parameters for Si II

A.2 Stacking Effects on the Outflow Velocity Measurements

The outflow central and maximum velocities are measured by fitting a profile to the absorption lines in the composite spectra (Chapter 5). We evaluate whether the outflow velocities measured from the composite spectra represents the typical outflow velocities of individual spectra.

We create 100 mock spectra including the C II absorption line that consists of the outflow and systemic components expressed in Equations (5.8) and (5.9). The free parameters of the two components are randomly taken from the ranges listed in Table A.2. For simplicity, $v_{\rm out}$ is used instead of $\lambda_{0,\rm out}$ with Equation (5.14). The spectral resolution is $R \sim 2000$, which is the same as the $z0$-sample. The continuum S/N of individual mock spectra is set to be 2. We produce the composite spectrum with the method described in Section 5.1.

Figure A.1 shows an individual spectrum and composite spectrum. The mean $v_{\rm out}$ and $v_{\rm max}$ values of individual spectra are 270 and 582 km s^{-1}, respectively. We measure $v_{\rm out}$ and $v_{\rm max}$ of the composite spectrum by fits described in Section 5.3 and evaluate the errors from the 1000 montecarlo resampling. The measured values are $v_{\rm out} = 248^{+24}_{-30}$ and $v_{\rm max} = 607^{+40}_{-35}$ km s^{-1}, which is consistent with the mean values of individual spectra.

Table A.2 Parameter range to create mock spectra

parameter	units	min	max
$v_{\rm out}$	km s^{-1}	150	400
$\tau_{0,\rm out}$		0.5	20
$C_{\rm f,out}$		0.4	0.6
$b_{\rm D,out}$	km s^{-1}	100	200
$\tau_{0,\rm sys}$		0.5	20
$C_{\rm f,sys}$		0.4	0.6
$b_{\rm D,sys}$	km s^{-1}	100	200

We also evaluate effects of a redshift uncertainty on the outflow velocities with the same setup. An adapted uncertainty is 60 km s^{-1}, which comes from the $z2$-sample and is the largest uncertainty in the $z0$, $z1$, $z2$, and $z6$-samples. We confirm that the

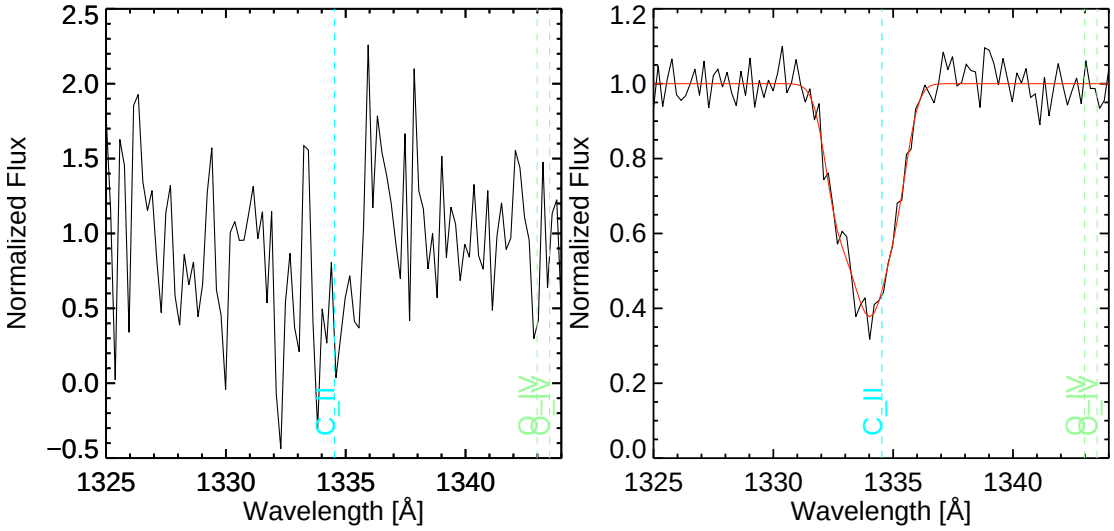

Figure A.1 Mock individual spectrum (Left) and composite spectrum (Right). The red solid line indicates the best-fit curve to the composite spectrum. The cyan vertical dashed line shows the rest wavelength.

redshift uncertainty does not change the $v_{\rm out}$ values while it tends to overestimate the $v_{\rm max}$ value to be $\simeq +40$ km s^{-1}. This systematics of the $v_{\rm max}$ values do not change the conclusion in this thesis.

REFERENCES

Abazajian, K., Adelman-McCarthy, J. K., Agüeros, M. A., et al. 2004, AJ, 128, 502, doi: 10.1086/421365

Abazajian, K. N., Adelman-McCarthy, J. K., Agüeros, M. A., et al. 2009, ApJS, 182, 543, doi: 10.1088/0067-0049/182/2/543

Adelberger, K. L., Steidel, C. C., Shapley, A. E., et al. 2004, ApJ, 607, 226, doi: 10.1086/383221

Ajiki, M., Taniguchi, Y., Murayama, T., et al. 2002, ApJ, 576, L25, doi: 10.1086/343026

Alexandroff, R. M., Heckman, T. M., Borthakur, S., Overzier, R., & Leitherer, C. 2015, ApJ, 810, 104, doi: 10.1088/0004-637X/810/2/104

Barai, P., Monaco, P., Murante, G., Ragagnin, A., & Viel, M. 2015, MNRAS, 447, 266, doi: 10.1093/mnras/stu2340

Behroozi, P. S., Wechsler, R. H., & Conroy, C. 2013, ApJ, 770, 57, doi: 10.1088/0004-637X/770/1/57

Bell, E. F., McIntosh, D. H., Katz, N., & Weinberg, M. D. 2003, ApJS, 149, 289, doi: 10.1086/378847

Blanton, M. R., & Roweis, S. 2007, AJ, 133, 734, doi: 10.1086/510127

Bordoloi, R., Lilly, S. J., Hardmeier, E., et al. 2014, ApJ, 794, 130, doi: 10.1088/0004-637X/794/2/130

Bouché, N., Hohensee, W., Vargas, R., et al. 2012, MNRAS, 426, 801, doi: 10.1111/j.1365-2966.2012.21114.x

Breitschwerdt, D., McKenzie, J. F., & Voelk, H. J. 1991, A&A, 245, 79

Brinchmann, J., Charlot, S., White, S. D. M., et al. 2004, MNRAS, 351, 1151, doi: 10.1111/j.1365-2966.2004.07881.x

Bruzual, G., & Charlot, S. 2003, MNRAS, 344, 1000, doi: 10.1046/j.1365-8711.2003.06897.x

Calzetti, D., Armus, L., Bohlin, R. C., et al. 2000, ApJ, 533, 682, doi: 10.1086/308692

Capak, P. L., Carilli, C., Jones, G., et al. 2015, Nature, 522, 455, doi: 10.1038/nature14500

Castor, J. I., Abbott, D. C., & Klein, R. I. 1975, ApJ, 195, 157, doi: 10.1086/153315

Ceverino, D., Arribas, S., Colina, L., et al. 2016, MNRAS, 460, 2731, doi: 10.1093/mnras/stw1195

Chabrier, G. 2003, PASP, 115, 763, doi: 10.1086/376392

Chen, Y.-M., Tremonti, C. A., Heckman, T. M., et al. 2010, AJ, 140, 445, doi: 10.1088/0004-6256/140/2/445

Chevalier, R. A., & Clegg, A. W. 1985, Nature, 317, 44, doi: 10.1038/317044a0

Chisholm, J., Orlitová, I., Schaerer, D., et al. 2017a, A&A, 605, A67, doi: 10.1051/0004-6361/201730610

Chisholm, J., Tremonti, C. A., Leitherer, C., & Chen, Y. 2016a, MNRAS, 463, 541, doi: 10.1093/mnras/stw1951

—. 2017b, MNRAS, 469, 4831, doi: 10.1093/mnras/stx1164

Chisholm, J., Tremonti, C. A., Leitherer, C., Chen, Y., & Wofford, A. 2016b, MNRAS, 457, 3133, doi: 10.1093/mnras/stw178

Chisholm, J., Tremonti, C. A., Leitherer, C., et al. 2015, ApJ, 811, 149, doi: 10.1088/0004-637X/811/2/149

Chisholm, J., Gazagnes, S., Schaerer, D., et al. 2018, A&A, 616, A30, doi: 10.1051/0004-6361/201832758

Christensen, C. R., Davé, R., Governato, F., et al. 2016, ApJ, 824, 57, doi: 10.3847/0004-637X/824/1/57

Cicone, C., Maiolino, R., & Marconi, A. 2016, A&A, 588, A41, doi: 10.1051/0004-6361/201424514

Ciddor, P. E. 1996, Appl. Opt., 35, 1566, doi: 10.1364/AO.35.001566

Coil, A. L., Newman, J. A., Kaiser, N., et al. 2004, ApJ, 617, 765, doi: 10.1086/425676

Coil, A. L., Weiner, B. J., Holz, D. E., et al. 2011, ApJ, 743, 46, doi: 10.1088/0004-637X/743/1/46

Concas, A., Popesso, P., Brusa, M., et al. 2017, A&A, 606, A36, doi: 10.1051/0004-6361/201629519

Concas, A., Popesso, P., Brusa, M., Mainieri, V., & Thomas, D. 2019, A&A, 622, A188, doi: 10.1051/0004-6361/201732152

Cooper, M. C., Newman, J. A., Davis, M., Finkbeiner, D. P., & Gerke, B. F. 2012, ASCL. http://ascl.net/1203.003

Davies, R. L., Förster Schreiber, N. M., Übler, H., et al. 2019, ApJ, 873, 122, doi: 10.3847/1538-4357/ab06f1

Davis, M., Faber, S. M., Newman, J., et al. 2003, in Proc. SPIE, Vol. 4834, Discoveries and Research Prospects from 6- to 10-Meter-Class Telescopes II, ed. P. Guhathakurta, 161–172

Davis, M., Guhathakurta, P., Konidaris, N. P., et al. 2007, ApJ, 660, L1, doi: 10.1086/517931

Dayal, P., & Ferrara, A. 2018, Phys. Rep., 780, 1, doi: 10.1016/j.physrep.2018.10.002

de Vaucouleurs, G. 1948, Annales d'Astrophysique, 11, 247

Decarli, R., Walter, F., Venemans, B. P., et al. 2017, Nature, 545, 457, doi: 10.1038/nature22358

Dekel, A., & Birnboim, Y. 2006, MNRAS, 368, 2, doi: 10.1111/j.1365-2966.2006.10145.x

Du, X., Shapley, A. E., Martin, C. L., & Coil, A. L. 2016, ApJ, 829, 64, doi: 10.3847/0004-637X/829/2/64

Du, X., Shapley, A. E., Reddy, N. A., et al. 2018, ApJ, 860, 75, doi: 10.3847/1538-4357/aabfcf

Erb, D. K., Quider, A. M., Henry, A. L., & Martin, C. L. 2012, ApJ, 759, 26, doi: 10.1088/0004-637X/759/1/26

Erb, D. K., Steidel, C. C., Shapley, A. E., et al. 2006a, ApJ, 647, 128, doi: 10.1086/505341

—. 2006b, ApJ, 646, 107, doi: 10.1086/504891

Erb, D. K., Steidel, C. C., Trainor, R. F., et al. 2014, ApJ, 795, 33, doi: 10.1088/0004-637X/795/1/33

Faber, S. M., Phillips, A. C., Kibrick, R. I., et al. 2003, in Proc. SPIE, Vol. 4841, Instrument Design and Performance for Optical/Infrared Ground-based Telescopes, ed. M. Iye & A. F. M. Moorwood, 1657–1669

Ferland, G. J., Korista, K. T., Verner, D. A., et al. 1998, PASP, 110, 761, doi: 10.1086/316190

Ferland, G. J., Porter, R. L., van Hoof, P. A. M., et al. 2013, RMxAA, 49, 137. https://arxiv.org/abs/1302.4485

Finley, H., Bouché, N., Contini, T., et al. 2017, A&A, 605, A118, doi: 10.1051/0004-6361/201730428

Förster Schreiber, N. M., Übler, H., Davies, R. L., et al. 2019, ApJ, 875, 21, doi: 10.3847/1538-4357/ab0ca2

Freeman, K. C. 2017, ARA&A, 55, 1, doi: 10.1146/annurev-astro-091916-055249

Fujimoto, S., Ouchi, M., Ferrara, A., et al. 2019, arXiv e-prints. https://arxiv.org/abs/1902.06760

Fukugita, M., Ichikawa, T., Gunn, J. E., et al. 1996, AJ, 111, 1748, doi: 10.1086/117915

Gallerani, S., Pallottini, A., Feruglio, C., et al. 2018, MNRAS, 473, 1909, doi: 10.1093/mnras/stx2458

Genzel, R., Tacconi, L. J., Lutz, D., et al. 2015, ApJ, 800, 20, doi: 10.1088/0004-637X/800/1/20

Griffiths, R. E., Ptak, A., Feigelson, E. D., et al. 2000, Science, 290, 1325, doi: 10.1126/science.290.5495.1325

Grimes, J. P., Heckman, T., Aloisi, A., et al. 2009, ApJS, 181, 272, doi: 10.1088/0067-0049/181/1/272

Gunn, J. E., Carr, M., Rockosi, C., et al. 1998, AJ, 116, 3040, doi: 10.1086/300645

Gunn, J. E., Siegmund, W. A., Mannery, E. J., et al. 2006, AJ, 131, 2332, doi: 10.1086/500975

Harikane, Y., Ouchi, M., Ono, Y., et al. 2016, ApJ, 821, 123, doi: 10.3847/0004-637X/821/2/123

—. 2018, PASJ, 70, S11, doi: 10.1093/pasj/psx097

Hashimoto, T., Verhamme, A., Ouchi, M., et al. 2015, ApJ, 812, 157, doi: 10.1088/0004-637X/812/2/157

Hashimoto, T., Inoue, A. K., Mawatari, K., et al. 2019, PASJ, 71, 71, doi: 10.1093/pasj/psz049

Hayward, C. C., & Hopkins, P. F. 2015, ArXiv e-prints. https://arxiv.org/abs/1510.05650

Heckman, T. M. 2002, in Astronomical Society of the Pacific Conference Series, Vol. 254, Extragalactic Gas at Low Redshift, ed. J. S. Mulchaey & J. T. Stocke, 292

Heckman, T. M., Alexandroff, R. M., Borthakur, S., Overzier, R., & Leitherer, C. 2015, ApJ, 809, 147, doi: 10.1088/0004-637X/809/2/147

Heckman, T. M., Armus, L., & Miley, G. K. 1990, ApJS, 74, 833, doi: 10.1086/191522

Heckman, T. M., & Borthakur, S. 2016, ApJ, 822, 9, doi: 10.3847/0004-637X/822/1/9

Heckman, T. M., Lehnert, M. D., Strickland, D. K., & Armus, L. 2000, ApJS, 129, 493, doi: 10.1086/313421

Heckman, T. M., Borthakur, S., Overzier, R., et al. 2011, ApJ, 730, 5, doi: 10.1088/0004-637X/730/1/5

Heger, A., Fryer, C. L., Woosley, S. E., Langer, N., & Hartmann, D. H. 2003, ApJ, 591, 288, doi: 10.1086/375341

Ilbert, O., McCracken, H. J., Le Fèvre, O., et al. 2013, A&A, 556, A55, doi: 10.1051/0004-6361/201321100

Inoue, A. K., Tamura, Y., Matsuo, H., et al. 2016, Science, 352, 1559, doi: 10.1126/science.aaf0714

Ipavich, F. M. 1975, ApJ, 196, 107, doi: 10.1086/153397

Ishigaki, M., Kawamata, R., Ouchi, M., et al. 2018, ApJ, 854, 73, doi: 10.3847/1538-4357/aaa544

Ishikawa, S., Kashikawa, N., Toshikawa, J., et al. 2017, ApJ, 841, 8, doi: 10.3847/1538-4357/aa6d64

Jones, T., Stark, D. P., & Ellis, R. S. 2012, ApJ, 751, 51, doi: 10.1088/0004-637X/751/1/51

Jones, T. A., Ellis, R. S., Schenker, M. A., & Stark, D. P. 2013, ApJ, 779, 52, doi: 10.1088/0004-637X/779/1/52

Kacprzak, G. G., Martin, C. L., Bouché, N., et al. 2014, ApJ, 792, L12, doi: 10.1088/2041-8205/792/1/L12

Karman, W., Caputi, K. I., Caminha, G. B., et al. 2017, A&A, 599, A28, doi: 10.1051/0004-6361/201629055

Kauffmann, G., Heckman, T. M., White, S. D. M., et al. 2003a, MNRAS, 341, 33, doi: 10.1046/j.1365-8711.2003.06291.x

Kauffmann, G., Heckman, T. M., Tremonti, C., et al. 2003b, MNRAS, 346, 1055, doi: 10.1111/j.1365-2966.2003.07154.x

Kimm, T., Haehnelt, M., Blaizot, J., et al. 2018, ArXiv e-prints. https://arxiv.org/abs/1801.04952

Kormendy, J., & Ho, L. C. 2013, ARA&A, 51, 511, doi: 10.1146/annurev-astro-082708-101811

Kornei, K. A., Shapley, A. E., Martin, C. L., et al. 2012, ApJ, 758, 135, doi: 10.1088/0004-637X/758/2/135

Kroupa, P. 2001, MNRAS, 322, 231, doi: 10.1046/j.1365-8711.2001.04022.x

Larson, R. B. 1974, MNRAS, 169, 229, doi: 10.1093/mnras/169.2.229

Law, D. R., Steidel, C. C., Shapley, A. E., et al. 2012, ApJ, 759, 29, doi: 10.1088/0004-637X/759/1/29

Leethochawalit, N., Jones, T. A., Ellis, R. S., Stark, D. P., & Zitrin, A. 2016, ApJ, 831, 152, doi: 10.3847/0004-637X/831/2/152

Lehnert, M. D., & Heckman, T. M. 1996a, ApJ, 462, 651, doi: 10.1086/177180

—. 1996b, ApJ, 472, 546, doi: 10.1086/178086

Leitherer, C., Ortiz Otálvaro, P. A., Bresolin, F., et al. 2010, ApJS, 189, 309, doi: 10.1088/0067-0049/189/2/309

Leitherer, C., Schaerer, D., Goldader, J. D., et al. 1999, ApJS, 123, 3, doi: 10.1086/313233

Lin, L., Koo, D. C., Weiner, B. J., et al. 2007, ApJ, 660, L51, doi: 10.1086/517919

Madau, P., & Dickinson, M. 2014, ARA&A, 52, 415, doi: 10.1146/annurev-astro-081811-125615

Maraston, C., Nieves Colmenárez, L., Bender, R., & Thomas, D. 2009, A&A, 493, 425, doi: 10.1051/0004-6361:20066907

Maraston, C., & Strömbäck, G. 2011, MNRAS, 418, 2785, doi: 10.1111/j.1365-2966.2011.19738.x

Markwardt, C. B. 2009, in Astronomical Society of the Pacific Conference Series, Vol. 411, Astronomical Data Analysis Software and Systems XVIII, ed. D. A. Bohlender, D. Durand, & P. Dowler, 251

Marrone, D. P., Spilker, J. S., Hayward, C. C., et al. 2018, Nature, 553, 51, doi: 10.1038/nature24629

Martin, C. L. 1998, ApJ, 506, 222, doi: 10.1086/306219

—. 2005, ApJ, 621, 227, doi: 10.1086/427277

—. 2006, ApJ, 647, 222, doi: 10.1086/504886

Martin, C. L., & Bouché, N. 2009, ApJ, 703, 1394, doi: 10.1088/0004-637X/703/2/1394

Martin, C. L., Shapley, A. E., Coil, A. L., et al. 2012, ApJ, 760, 127, doi: 10.1088/0004-637X/760/2/127

McLean, I. S., Becklin, E. E., Bendiksen, O., et al. 1998, in Proc. SPIE, Vol. 3354, Infrared Astronomical Instrumentation, ed. A. M. Fowler, 566–578

Mitchell, P. D., Blaizot, J., Devriendt, J., et al. 2018, MNRAS, 474, 4279, doi: 10.1093/mnras/stx3017

Mitra, S., Davé, R., & Finlator, K. 2015, MNRAS, 452, 1184, doi: 10.1093/mnras/stv1387

Mo, H. J., & White, S. D. M. 2002, MNRAS, 336, 112, doi: 10.1046/j.1365-8711.2002.05723.x

Morton, D. C. 1991, ApJS, 77, 119, doi: 10.1086/191601

—. 2003, ApJS, 149, 205, doi: 10.1086/377639

Mostek, N., Coil, A. L., Moustakas, J., Salim, S., & Weiner, B. J. 2012, ApJ, 746, 124, doi: 10.1088/0004-637X/746/2/124

Muratov, A. L., Kereš, D., Faucher-Giguère, C.-A., et al. 2015, MNRAS, 454, 2691, doi: 10.1093/mnras/stv2126

Murray, N., Martin, C. L., Quataert, E., & Thompson, T. A. 2007, ApJ, 660, 211, doi: 10.1086/512660

Murray, N., Quataert, E., & Thompson, T. A. 2005, ApJ, 618, 569, doi: 10.1086/426067

Muzahid, S., Kacprzak, G. G., Churchill, C. W., et al. 2015, ApJ, 811, 132, doi: 10.1088/0004-637X/811/2/132

Nakajima, K., & Ouchi, M. 2014, MNRAS, 442, 900, doi: 10.1093/mnras/stu902

Nelson, D., Pillepich, A., Springel, V., et al. 2019, MNRAS, 2010, doi: 10.1093/mnras/stz2306

Newman, J. A., Cooper, M. C., Davis, M., et al. 2013, ApJS, 208, 5, doi: 10.1088/0067-0049/208/1/5

Oke, J. B., Cohen, J. G., Carr, M., et al. 1995, PASP, 107, 375, doi: 10.1086/133562

Oppenheimer, B. D., & Davé, R. 2006, MNRAS, 373, 1265, doi: 10.1111/j.1365-2966.2006.10989.x

Oppenheimer, B. D., Davé, R., Kereš, D., et al. 2010, MNRAS, 406, 2325, doi: 10.1111/j.1365-2966.2010.16872.x

Padilla, N. D., & Strauss, M. A. 2008, MNRAS, 388, 1321, doi: 10.1111/j.1365-2966.2008.13480.x

Pavesi, R., Riechers, D. A., Capak, P. L., et al. 2016, ApJ, 832, 151, doi: 10.3847/0004-637X/832/2/151

Prochaska, J. X., Kasen, D., & Rubin, K. 2011, ApJ, 734, 24, doi: 10.1088/0004-637X/734/1/24

Read, J. I., & Trentham, N. 2005, Philosophical Transactions of the Royal Society of London Series A, 363, doi: 10.1098/rsta.2005.1648

Reddy, N. A., Steidel, C. C., Pettini, M., et al. 2008, ApJS, 175, 48, doi: 10.1086/521105

Roberts-Borsani, G. W., & Saintonge, A. 2019, MNRAS, 482, 4111, doi: 10.1093/mnras/sty2824

Robertson, B. E., Ellis, R. S., Furlanetto, S. R., & Dunlop, J. S. 2015, ApJ, 802, L19, doi: 10.1088/2041-8205/802/2/L19

Rockosi, C., Stover, R., Kibrick, R., et al. 2010, in Proc. SPIE, Vol. 7735, Ground-based and Airborne Instrumentation for Astronomy III, 77350R

Rubin, K. H. R., Prochaska, J. X., Koo, D. C., et al. 2014, ApJ, 794, 156, doi: 10.1088/0004-637X/794/2/156

Rubin, K. H. R., Weiner, B. J., Koo, D. C., et al. 2010, ApJ, 719, 1503, doi: 10.1088/0004-637X/719/2/1503

Rupke, D. 2018, Galaxies, 6, 138, doi: 10.3390/galaxies6040138

Rupke, D. S., Veilleux, S., & Sanders, D. B. 2002, ApJ, 570, 588, doi: 10.1086/339789

—. 2005a, ApJS, 160, 87, doi: 10.1086/432886

—. 2005b, ApJS, 160, 115, doi: 10.1086/432889

Salim, S., Rich, R. M., Charlot, S., et al. 2007, ApJS, 173, 267, doi: 10.1086/519218

Salpeter, E. E. 1955, ApJ, 121, 161, doi: 10.1086/145971

Sánchez-Blázquez, P., Peletier, R. F., Jiménez-Vicente, J., et al. 2006, MNRAS, 371, 703, doi: 10.1111/j.1365-2966.2006.10699.x

Sato, T., Martin, C. L., Noeske, K. G., Koo, D. C., & Lotz, J. M. 2009, ApJ, 696, 214, doi: 10.1088/0004-637X/696/1/214

Savage, B. D., & Sembach, K. R. 1996, ARA&A, 34, 279, doi: 10.1146/annurev.astro.34.1.279

Scannapieco, E., & Brüggen, M. 2015, ApJ, 805, 158, doi: 10.1088/0004-637X/805/2/158

Schaye, J., Crain, R. A., Bower, R. G., et al. 2015, MNRAS, 446, 521, doi: 10.1093/mnras/stu2058

Schroetter, I., Bouché, N., Péroux, C., et al. 2015, ApJ, 804, 83, doi: 10.1088/0004-637X/804/2/83

Schroetter, I., Bouché, N., Wendt, M., et al. 2016, ApJ, 833, 39, doi: 10.3847/1538-4357/833/1/39

Schroetter, I., Bouché, N. F., Zabl, J., et al. 2019, MNRAS, 490, 4368, doi: 10.1093/mnras/stz2822

Schwartz, C. M., & Martin, C. L. 2004, ApJ, 610, 201, doi: 10.1086/421546

Schwartz, C. M., Martin, C. L., Chandar, R., et al. 2006, ApJ, 646, 858, doi: 10.1086/504961

Scoville, N., Aussel, H., Brusa, M., et al. 2007, ApJS, 172, 1, doi: 10.1086/516585

Shapley, A. E., Steidel, C. C., Pettini, M., & Adelberger, K. L. 2003, ApJ, 588, 65, doi: 10.1086/373922

Sharma, M., Theuns, T., Frenk, C., et al. 2017, MNRAS, 468, 2176, doi: 10.1093/mnras/stx578

Shibuya, T., Ouchi, M., & Harikane, Y. 2015, ApJS, 219, 15, doi: 10.1088/0067-0049/219/2/15

Shibuya, T., Ouchi, M., Nakajima, K., et al. 2014, ApJ, 788, 74, doi: 10.1088/0004-637X/788/1/74

Somerville, R. S., & Davé, R. 2015, ARA&A, 53, 51, doi: 10.1146/annurev-astro-082812-140951

Speagle, J. S., Steinhardt, C. L., Capak, P. L., & Silverman, J. D. 2014, ApJS, 214, 15, doi: 10.1088/0067-0049/214/2/15

Spitzer, L. 1978, Physical processes in the interstellar medium (New York Wiley-Interscience), doi: 10.1002/9783527617722

Springel, V., & Hernquist, L. 2003, MNRAS, 339, 289, doi: 10.1046/j.1365-8711.2003.06206.x

Springel, V., White, S. D. M., Jenkins, A., et al. 2005, Nature, 435, 629, doi: 10.1038/nature03597

Steidel, C. C., Adelberger, K. L., Shapley, A. E., et al. 2003, ApJ, 592, 728, doi: 10.1086/375772

Steidel, C. C., Erb, D. K., Shapley, A. E., et al. 2010, ApJ, 717, 289, doi: 10.1088/0004-637X/717/1/289

Steidel, C. C., Shapley, A. E., Pettini, M., et al. 2004, ApJ, 604, 534, doi: 10.1086/381960

Steidel, C. C., Strom, A. L., Pettini, M., et al. 2016, ApJ, 826, 159, doi: 10.3847/0004-637X/826/2/159

Steidel, C. C., Rudie, G. C., Strom, A. L., et al. 2014, ApJ, 795, 165, doi: 10.1088/0004-637X/795/2/165

Steinhardt, C. L., Speagle, J. S., Capak, P., et al. 2014, ApJ, 791, L25, doi: 10.1088/2041-8205/791/2/L25

Strauss, M. A., Weinberg, D. H., Lupton, R. H., et al. 2002, AJ, 124, 1810, doi: 10.1086/342343

Strickland, D. K., & Heckman, T. M. 2009, ApJ, 697, 2030, doi: 10.1088/0004-637X/697/2/2030

Swinbank, M., Harrison, C., Tiley, A., et al. 2019, arXiv e-prints. https://arxiv.org/abs/1906.05311

Tacchella, S., Bose, S., Conroy, C., Eisenstein, D. J., & Johnson, B. D. 2018, ApJ, 868, 92, doi: 10.3847/1538-4357/aae8e0

Tanner, R., Cecil, G., & Heitsch, F. 2016, ApJ, 821, 7, doi: 10.3847/0004-637X/821/1/7

Trainor, R. F., Steidel, C. C., Strom, A. L., & Rudie, G. C. 2015, ApJ, 809, 89, doi: 10.1088/0004-637X/809/1/89

Tremonti, C. A., Moustakas, J., & Diamond-Stanic, A. M. 2007, ApJ, 663, L77, doi: 10.1086/520083

Tremonti, C. A., Heckman, T. M., Kauffmann, G., et al. 2004, ApJ, 613, 898, doi: 10.1086/423264

Tumlinson, J., Peeples, M. S., & Werk, J. K. 2017, ARA&A, 55, 389, doi: 10.1146/annurev-astro-091916-055240

Vázquez, G. A., Leitherer, C., Heckman, T. M., et al. 2004, ApJ, 600, 162, doi: 10.1086/379805

Veilleux, S., Cecil, G., & Bland-Hawthorn, J. 2005, ARA&A, 43, 769, doi: 10.1146/annurev.astro.43.072103.150610

Wadepuhl, M., & Springel, V. 2011, MNRAS, 410, 1975, doi: 10.1111/j.1365-2966.2010.17576.x

Walter, F., Riechers, D., Novak, M., et al. 2018, ApJ, 869, L22, doi: 10.3847/2041-8213/aaf4fa

Weiner, B. J., Coil, A. L., Prochaska, J. X., et al. 2009, ApJ, 692, 187, doi: 10.1088/0004-637X/692/1/187

Weller, J., Ostriker, J. P., Bode, P., & Shaw, L. 2005, MNRAS, 364, 823, doi: 10.1111/j.1365-2966.2005.09602.x

Willmer, C. N. A., Faber, S. M., Koo, D. C., et al. 2006, ApJ, 647, 853, doi: 10.1086/505455

York, D. G., Adelman, J., Anderson, Jr., J. E., et al. 2000, AJ, 120, 1579, doi: 10.1086/301513

Zahid, H. J., Geller, M. J., Kewley, L. J., et al. 2013, ApJ, 771, L19, doi: 10.1088/2041-8205/771/2/L19

Zhang, D. 2018, Galaxies, 6, 114, doi: 10.3390/galaxies6040114

Zhu, G. B., Comparat, J., Kneib, J.-P., et al. 2015, ApJ, 815, 48, doi: 10.1088/0004-637X/815/1/48